NORTHWESTERN UNIVERSITY

Localization of Oscillons and Periodically Forced Waves

A DISSERTATION

SUBMITTED TO THE GRADUATE SCHOOL
IN PARTIAL FULFILLMENT OF THE REQUIREMENTS

for the degree of
DOCTOR OF PHILOSOPHY
Field of Applied Mathematics

By
Catherine Crawford

EVANSTON, ILLINOIS
December 2000

ABSTRACT

Localization of Oscillons and Periodically Forced Waves

Catherine Crawford

Motivated by the observation of localized structures in various experimental systems, the mechanisms responsible for localization are investigated within the framework of model equations. First an extension of a Swift-Hohenberg model that exhibits a subcritical transition to square patterns is considered. This model is used to describe localized circular excitations ('oscillons') observed in vertically vibrated granular layers [1]. For sufficiently strong damping of the basic state, stable oscillon structures are found. The localization mechanism is quite general and is due to non-adiabatic effects. Bound structures of oscillons of equal and opposite polarity are found with bound states of like polarity being less robust. Much of the phenomena are consistent with the experimental observations and suggest that oscillons are not specific to patterns in granular media or to parametrically driven systems.

In systems that exhibit a bistability between nonlinear traveling waves and the basic state, pairs of fronts connecting these two states can bind to form localized wave pulses whose stability depends on the interaction between the fronts. The localization of waves within the framework of coupled Ginzburg-Landau equations describing the traveling-wave amplitudes is investigated. We find that the introduction of resonant temporal forcing results in a *new, tunable* mechanism for stabilizing such wave pulses. In contrast to other localization mechanisms the temporal forcing can achieve localization by a repulsive as well as by an attractive interaction between the fronts. The combined effect of temporal modulation and other mechanisms is also investigated. The results are expected to be relevant for binary-mixture convection and for electroconvection in nematic liquid crystals.

For my grandmother, Gwen.

Acknowledgments

As I conclude my time at Northwestern, I would like to thank the many people whose help and support have contributed to the successful completion of this work. I am grateful to my advisor Hermann Riecke for his support, guidance, and patience. I am also thankful to the professors of the Applied Mathematics Department for their additional instruction. In particular, Mary Silber has provided helpful suggestions for this work over the past few years. Thanks to Judy and Edla for taking care of the details and enduring my all-too-frequent calls to the mechanic.

I wish to thank numerous friends for their support over the past few years. I could not have done it without my fellow first-years Volodia, Dimitri, Colleen, and especially Cyndi and Brian. Thanks for keeping my sanity and thanks for keeping me here. Thank you to the occupants of the office next door where I enjoyed taking breaks from work, most recently playing backgammon with Rich. I would like to thank the Cundick Clan (Voss and Palmer) for welcoming me into their family. I am thankful to my good friends Linda and Rebekah for their support and friendship. I am especially grateful for Fil. Thanks for believing in me when I was uncertain.

Most importantly, I want to thank my family. I am thankful for all my nieces and nephews who add noise and fun to my visits home. To my siblings and their spouses, Leslie and Marshall, Van and Janet, Chase, and Cache, I admire and love you all. Thank you for your love and support. My parents have been wonderful. I am thankful that they brought me home every year for Christmas and Redfish Lake where I took advantage of the opportunity to escape the responsibilities and stress of school for a time. They have filled our home and my life with faith, love, happiness and a lot of laughter. I am grateful to them for giving me a sense of who I am and what I can become.

Contents

List of Figures

Chapter 1

Introduction

Many systems driven far from equilibrium undergo instabilities leading to the formation of patterns. Rayleigh-Bénard convection in which a thin fluid layer is heated from below is a classic example. Here a periodic roll structure emerges in the convecting fluid. Experimental and theoretical investigations of patterns are aimed at understanding the mechanisms involved in the formation and selection of patterns as well as their stability and temporal evolution. Equations describing the underlying dynamics of such systems, such as the Navier-Stokes equations for fluids, are typically complicated. Hence, one attempts to describe the instabilities and associated patterns on a macroscopic scale with simpler model equations. Current understanding of spatio-temporal patterns is well advanced and the reader is referred to [2] for a more comprehensive review of pattern formation. In the continuing study of pattern formation, much current work focuses on more complex structures such as the localized states considered in this thesis.

Observations of localized structures confined to a small spatial region of the system have led to additional questions; particularly why such states do not expand to fill the entire system. Hence, one is interested in understanding the mechanisms responsible for their existence and stability. Once again, these localized structures are often studied within simpler model equations, not only due to the complexity of underlying microscopic equations (if even known), but also to provide a universality for describing similar states in diverse systems. The implications of localized structures in any given system may vary from being highly disruptive and unwanted to being of great import such as solitons with applications in nonlinear optics. Hence, a thorough understanding of localized structures is needed in order to successfully suppress or exploit such states.

This thesis addresses localized structures and their localization mechanisms as motivated by experimental observations. First, localized excitations called oscillons are studied within a modified Swift-Hohenberg equation where localization is attributed to nonadiabatic locking. Although this localization mechanism has been shown previously to lock one-dimensional structures [3, 4], we propose that it extends to locking in two spatial dimensions. Additionally, the generality of the model and the mechanism suggest that oscillon-type structures may be observed in other systems exhibiting a subcritical transition to square patterns. Oscillon-type structures and their interactions are investigated numerically using the Swift-Hohenberg model. Second, a new localization mechanism is discovered for traveling-wave pulses within coupled Ginzburg-Landau equations. Periodically forcing the system excites the oppositely traveling wave providing an additional mode that can lead to localized traveling waves. Hence this new mechanism can be externally controlled, or tuned, by the strength of the periodic forcing.

The next section introduces a basic theoretical framework for understanding localized states. The following section provides an overview of localized structures observed in a variety of physical systems and theoretical background for known localization mechanisms. More detailed descriptions are given of the experimental systems motivating this work; namely oscillons in vertically vibrated granular layers, pulses in binary-mixture convection, and worms in nematic liquid crystals. The final section of the introduction outlines the scope of this thesis.

1.1 General Framework

As with spatially extended patterns, theoretical understanding of localized states are usually investigated within the framework of simpler model equations. Such equations are often asymptotically derived from the underlying equations near the onset of instability. As a starting point for localized structures, consider single front solutions within a simple reaction-diffusion equation

$$\partial_t A = \partial_x^2 A - \frac{\partial V}{\partial A} \tag{1.1}$$

for the amplitude A of a pattern. Front solutions to (1.1) correspond to a heteroclinic orbit in phase space connecting two different solutions of $-\partial V/\partial A = 0$ (i.e. extrema of $-V$). In a frame moving with the velocity of such a front, the ansatz $A = A(x - vt) = A(\eta)$ inserted in to (1.1) yields the following equation

$$\partial_\eta^2 A + v\partial_\eta A - \frac{\partial V}{\partial A} = 0. \tag{1.2}$$

This equation describes the motion of a particle in the inverted potential $-V$ with frictional damping given by the velocity v. Figure 1.1a shows a general double-well potential where the maxima correspond to the stable equilibria $A^{\pm}$ and the minimum to an unstable equilibrium A^0. Hence, for a given potential V, a

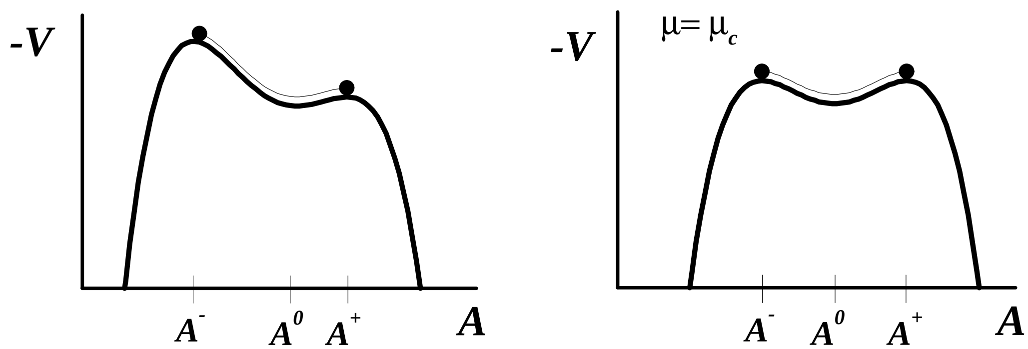

Figure 1.1: Double-well potentials for (a) $\mu \neq \mu_c$ and (b) $\mu = \mu_c$ where values of the maxima are equal.

unique front solution is obtained for the specific value of the friction coefficient that describes a particle starting from rest at the absolute maximum of $-V$, say A^-, then rolls down and back up to rest at the other maximum. In other words, the velocity of the front is uniquely determined by this value of v. Other values of v do not admit front solutions connecting the two stable equilibria as the particle would either not reach or overshoot the other maximum for larger friction and smaller friction, respectively.

For large friction v, a particle beginning at A^- will roll down without overshoot to the minimum representing the unstable equilibrium at A^0. For smaller v, but not small enough for the particle to reach A^+, the particle will overshoot the minimum before returning to rest at A^0. Depending on the size of the friction v, this overshoot may lead to decaying oscillations as it approaches A^0. The leading edge of this front connecting the stable and unstable equilibria is then oscillatory. In contrast with the unique front connecting the two stable points A^- and A^+, there exists a one-parameter family of fronts connecting A^- and A^0.

Let the deformations to the potential be described by a control parameter μ. Then define μ_c to be the value of the control parameter where the potential at A^- is equal to the potential at A^+ and the front connecting the two states is stationary. If $\mu < \mu_c$, then the absolute maximum is at A^- and the front is no longer stationary as the A^- state invades the A^+ state. For nearly stationary fronts ($v \ll 1$), μ is near μ_c and this unique velocity can be determined perturbatively to depend linearly on the control parameter

$$v = \frac{k_1}{2}(\mu - \mu_c). \tag{1.3}$$

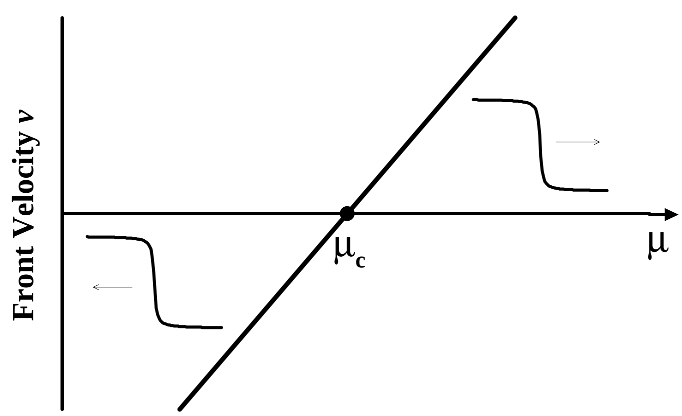

Figure 1.2: Single front velocity. The front is stationary for a single value of the control parameter μ_c.

Localized structures can be formed by combining two of these front solutions. For concreteness, consider now the real Ginzburg-Landau equation for a subcritical bifurcation

$$\partial_t A = d\partial_x^2 A + \mu A + cA^3 - pA^5, \tag{1.4}$$

where the coefficients c, d, and $p > 0$. If we restrict ourselves to solutions $A \geq 0$, then in the previous potential picture, A^- corresponds to the basic zero state and A^+ corresponds to the stable, uniform nonzero steady state. Bound pairs of fronts connecting these two states describe localized solutions. Recall each individual front is moving slowly. If the two fronts are widely separated then the presence of the other front only weakly deforms the front shape and its velocity. This weak interaction leads to the slow evolution of the distance L separating the two fronts [5]

$$\frac{dL}{dt} = k_1(\mu - \mu_c) - k_4 e^{-L/\xi} \tag{1.5}$$

where k_1 and k_4 are positive coefficients which depend on the parameters c, d, and p from equation (1.4). The interaction term is a result of the overlap in the nonlinear amplitude of the two fronts. Figure 1.3 is a sketch of dL/dt as a function of pulse length L based on equation (1.5). There is only one fixed point where $dL/dt = 0$ when $\mu > \mu_c$. Since $k_4 > 0$, an increase in length weakens the attractive interaction between the fronts and they are pushed further apart, whereas a decrease in length results in the fronts coming even closer together. Hence, this fixed point is an unstable pulse. This unstable situation suggests that other contributions must be relevant to stabilize localized structures.

1.2 Localized Structures in Pattern Forming Systems

Examples of localized structures include the coexisting domains of long and short wavelengths observed in Taylor-Couette flow between co-rotating concentric cylinders [6], in Rayleigh-Bénard convection in narrow slots [7], and in parametrically excited waves in ferrofluids [8]. Motivated by the convective rolls and Taylor

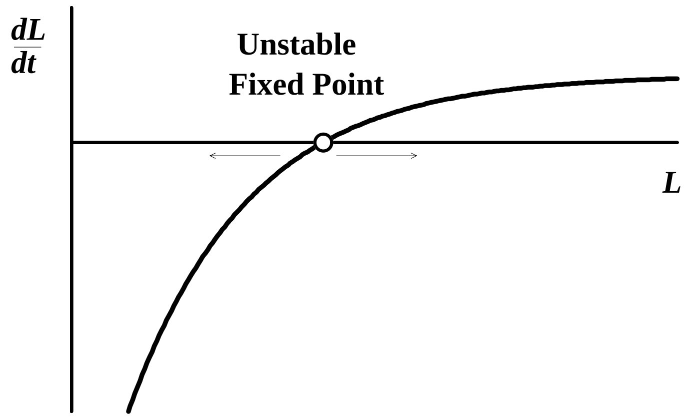

Figure 1.3: dL/dt vs. pulse length L showing the unstable fixed point when $\mu - \mu_c > 0$.

vortices, a localization mechanism within the framework of phase dynamics is introduced in [9] that is further investigated in [10–13]. The system is described by a phase equation for the slow dynamics of the local phase of the underlying pattern. When the diffusion coefficient becomes negative, the pattern becomes Eckhaus unstable. Typically this leads to a phase slip and the relaxation back to a periodic pattern with a wave number within the Eckhaus-stable band. However, the situation may be such that for negative diffusion coefficient, the stable band of wave numbers splits. Domain structures then form from patterns with wave numbers in each of the two separate bands. The structures are stable for boundary conditions which conserve the phase. Phase conservation means that the total number of cells, e.g. convective rolls, remains constant when there are no amplitude variations. Similar domain structures were predicted in [14] for a system with a nonmonotonic dispersion relation leading to a similar split in the Eckhaus stable band of wave numbers. Subsequently, corresponding states were confirmed experimentally in ferrofluids [8].

Localized regions of high and low current states called current filaments have been observed in both semiconductors [15] and gas discharge systems [16]. Their localization has been described by extending the reaction-diffusion equation (1.4) to include a global constraint term representing an inhibitory mechanism related to the external system [17,18]. As the domain length L of a nonzero amplitude

A expands, the global inhibition suppresses A which slows the expansion leading to a stabilizing effect.

Instabilities which break the reflection symmetry of patterns, i.e. parity-breaking bifurcations, can lead to localized waves which propagate through the stationary pattern. These drift waves have been observed in a variety of systems such as directional solidification [19], the printer instability [20], viscous fingering [21], cellular flames [22], and Taylor vortex flow between counter-rotating cylinders [23]. By decomposing the spatial pattern into symmetric and asymmetric components, the parity-breaking dynamics have been investigated via equations that couple the amplitude of the symmetry-breaking mode with the phase of the underlying pattern [24–29]. The amplitude itself depends directly on the wavenumber of the pattern. Even when the bifurcation is supercritical, localized structures corresponding to homoclinic orbits in space can be obtained for nonzero velocity; hence the observed drifting of the localized waves. Localization is possible because of the amplitude dependence on the gradient of the phase which enhances the local growth rate within the localized region.

Since Russell's sighting of a soliton traveling on the surface of a water channel nearly two centuries ago, these localized structures in conservative systems have emerged on the forefront of scientific investigation [30], including technological application in fiber optics [31]. One of the most interesting features of solitons is their ability to emerge unscathed from collisions with another soliton. Solitons arise as solutions to the nonlinear Schrödinger equation

$$2iA_t + A_{xx} + 2|A|^2A^* = 0 \tag{1.6}$$

where the nonlinearity tends to focus the pulse and acts to balance the linear forces trying to disperse the pulse. Even in non-conservative systems, several other observed localized structures have been described in terms of perturbed solitons. They include surface water waves in horizontally vibrated troughs [32], envelope solitons in elastic media [33], and the binary-mixture pulses discussed below in section 1.2.2.

1.2.1 Oscillons in Vertically Vibrated Granular Layers

The work in chapter 2 was motivated by experiments done on vertically vibrated thin layers of granular material. Figure 1.4 shows a sketch of the experimental setup. The container holding the granular material, typically bronze spheres, is displaced vertically with a periodic driving, $z = A \sin \omega t$. The granular layer stays on the plate when the non-dimensional acceleration amplitude $\Gamma \equiv A\omega^2/g < 1$, ($g$ is the acceleration due to gravity). But for $\Gamma > 1$ the layer may lift off from the plate when the downward acceleration of the plate is greater than g. In this regime the experiments have revealed a wealth of interesting phenomena [1, 34–38]. Depending on the driving frequency and amplitude different types of standing-wave

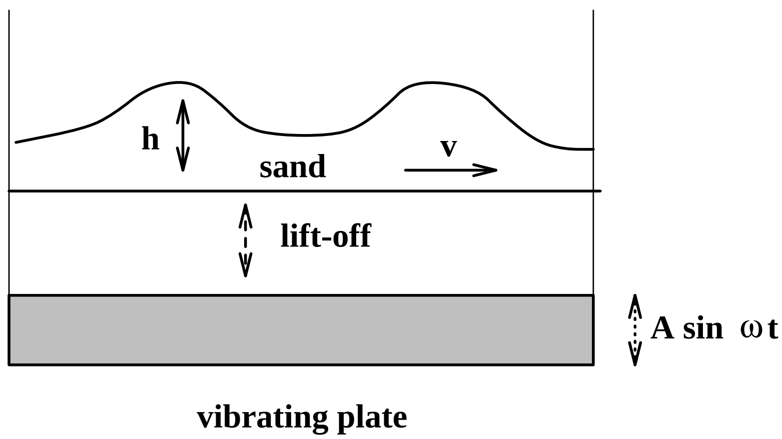

Figure 1.4: Schematic of experimental setup of vertically vibrated granular layers.

patterns are observed. They can be ordered, e.g. stripe patterns and square patterns as they are also observed in parametrically excited surface waves on liquids, or disordered. Particularly exciting is the observation of two-dimensional localized structures which were termed ‘oscillons’ [1]. Figure 1.5 shows experimental pictures of oscillons looking down on the granular layer [39]. Due to the subharmonic response of the excitation, they resemble during one cycle of the driving a circular peak and during the next cycle a circular crater. Since the driving is invariant under shifts by one period, peaks and craters can exist simultaneously in any given cycle (Figure 1.5a). The excitations are found to form bound structures. Thus in the experiments, stable pairs, tetramers, and chains of alternating polarity are observed (Figures 1.5b-d,e). In fact, even the square pattern can be thought of as being built up from these individual units rather than extended waves.

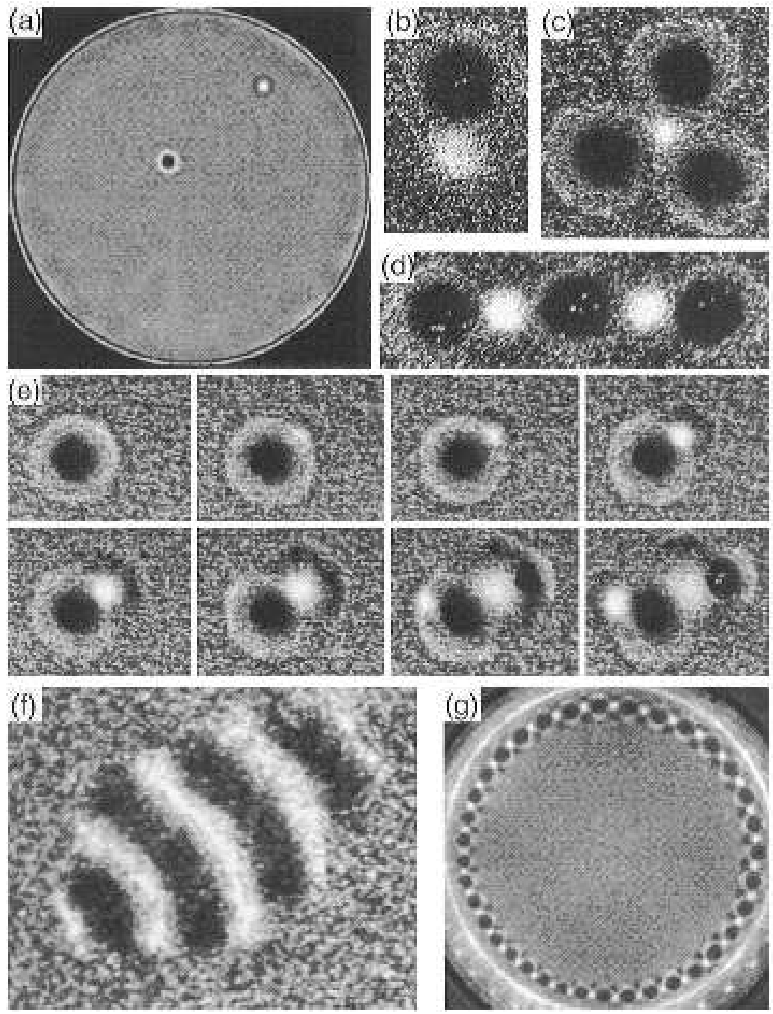

Figure 1.5: Experimentally observed oscillons: (a) Two isolated oscillons in different phases. (b)-(e),(g) Bound states of oscillons of opposite polarity. (e-f) Transitions observed when oscillons lose stability. [39] Pictures courtesy of Paul Umbanhowar.

Stimulated by these experiments oscillon-type patterns have been studied theoretically from a number of different angles [40–43]. In [40] oscillons are found within a Ginzburg-Landau approach; assuming small amplitudes and weak damping of the waves a Ginzburg-Landau equation for the wave amplitude is coupled to a mode describing the local height of the granular layer. In [41] the waves are described using a stroboscopic map in which the waves arise in a period-doubling bifurcation. A more detailed modeling of the dynamics of the granular layer is pursued in [42–45]. In [43] the granular layer is modeled as a sheet that locally follows the dynamics of an inelastic ball whereas in [42] the core ingredients are the free flight of the granular particles and diffusion. While in [40–44] oscillon-type structures have been found numerically, the mechanism that is responsible for the localization of the waves has not been clearly identified. Chapter 2 of this thesis identifies non-adiabatic locking of fronts as a localization mechanism responsible for oscillon-type structures.

1.2.2 Pulses in Binary-Mixture Convection

Localized traveling wave trains have been observed in convection of binary-fluid mixtures. As with pure-fluid Rayleigh-Bénard convection, a thin layer of fluid is heated from below. The physical system is essentially described by the following four parameters [46]: the Rayleigh number R which is proportional to the applied vertical temperature difference, the Prandtl number P which measures the ratio of the kinematic viscosity to the thermal diffusivity, the Lewis number $\mathcal{L}$ which measures the ratio of mass diffusion to thermal diffusion, and the separation ratio ψ which characterizes the alcohol concentration of the fluid mixture. For Lewis number $\mathcal{L} \ll 1$ and negative separation ratio $\psi < -\mathcal{L}^2$, the uniform conductive state loses stability to oscillations as the Rayleigh number is increased above a critical value R_c. The competition between heat and mass diffusion occurring on two very different time scales leads to the oscillatory instability in the form of traveling waves. The transition to nonlinear traveling waves is strongly hysteretic resulting in a bistability between the conductive state and traveling-wave convective state. It is in this region of bistability that spatially confined states of traveling-wave convection are observed. Figure 1.6 shows two typical traveling-wave pulses viewed from above in an annular experimental geometry.

These pulses are one of the most studied and well understood localized

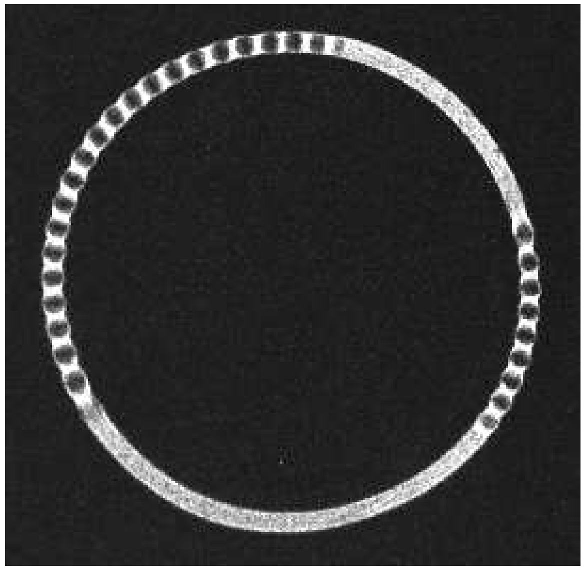

Figure 1.6: Experimental picture of localized traveling-wave pulses in binary-mixture convection [46]. Picture courtesy of Paul Kolodner.

structures. Initial attempts to describe the localization of similar states found in rectangular geometries focused on confinement effects due to reflection of the traveling waves at the end walls [46]. However, subsequent observation of the same states in annular geometries where end wall effects are absent, led to further investigation of their localization mechanism. Within the framework of a complex Ginzburg-Landau equation describing a subcritical bifurcation (1.7), dispersion can lead to localized states

$$\partial_t A = d\partial_x^2 A + \mu A + c|A|^2 A - p|A|^4 A, \tag{1.7}$$

where the amplitude A and the coefficients are complex. In the highly dispersive regime where the imaginary parts of the coefficients are large, the pulses have been described as perturbed solitons of the nonlinear Schrödinger equation (in NLS, $p = 0$ and d, μ, and c are purely imaginary). In regimes of weak dispersion, the pulses are described as bound fronts connecting the bistable states as described in section 1.1. In this case the inclusion of weak dispersion (i.e. small imaginary terms) additionally affects the interaction between fronts, modifying the evolution equation (1.5) for the pulse length L to be [47, 5]

$$\frac{dL}{dt} = k_1(\mu - \hat{\mu}_c) - k_4 e^{-2L/\xi} + \frac{k_5}{L}, \tag{1.8}$$

where $\hat{\mu}_c$ and k_5 contain the contributions from the dispersive terms. In order for a front to connect the nonzero traveling-wave state to the zero basic state, a unique wavenumber must be selected at the position of the fronts, i.e. $k = \pm k_\infty$ at the left- and right-fronts, respectively. Hence, for interacting fronts to form a bound pair, these opposite wavenumbers must be matched via a gradient in the wavenumber across the length of the pulse. The change in the local wavenumber is given by $\delta k(x) \sim 2k_\infty/L$ which gives rise to the k_5/L term in equation (1.8). For $k_5 > 0$ this term provides a repulsive interaction and there is the possibility of two pulses corresponding to two fixed points of (1.8)[1]. When $\mu < \hat{\mu}_c$ this repulsion can balance the inward "pressure" and the second, longer pulse exists and is stable. Figure 1.7 is a sketch of dL/dt versus pulse length L.

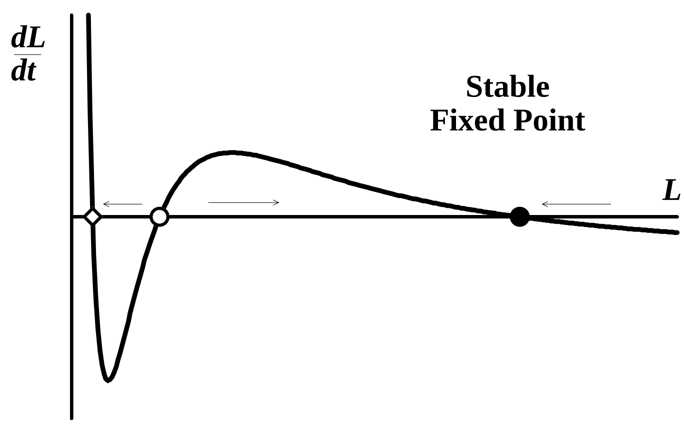

Figure 1.7: dL/dt vs. pulse length L. The solid circle indicates the stable fixed point due to dispersion. The unstable fixed point is indicated by the open circle. Then fixed point indicated by the open diamond represents the unphysical solution where the analysis is invalid for small L.

Although the inclusion dispersion resulted analytically in stable localized states, several features of the pulses observed both experimentally and in numerical

[1]Equation (1.8) actually has a third shorter fixed point. But in the derivation of equation (1.8) L is assumed to be large. Hence this fixed point falls outside of the range of validity and represents an unphysical solution.

simulations of the full Navier-Stokes equations could not be explained within the standard complex Ginzburg-Landau equation (1.7). The drift velocity of a localized solution of the complex Ginzburg-Landau equation is approximately equal to the group velocity[2]. However, observed pulses drifted with a velocity an order of magnitude smaller than the group velocity. Also at the same parameter values, pulses of different lengths were observed whose ordering with respect to length and stability was not consistent with the complex Ginzburg-Landau equations.

The standard CGL equation breaks down for small Lewis number $\mathcal{L}$ and it was shown in [48, 49] that slowly evolving concentration modes must be retained. Extended complex Ginzburg-Landau (ECGL) equations which couple the convective amplitude A and the concentration mode C were derived from the Navier-Stokes equations:

$$\partial_t A = -s\partial_x A + d\partial_x^2 A + (\mu + fC)A + c|A|^2 A - p|A|^4 A \tag{1.9}$$

$$\partial_t C = \delta\partial_x^2 C - \alpha C + h\partial_x |A|^2. \tag{1.10}$$

The actual derivation results in more coupling terms [48] and equations (1.9-1.10) represent a minimal model describing the system. Localized structures of bound fronts were also obtained within this set of coupled equations even in the absence of dispersion. Similar to the localization for a parity-breaking bifurcation, the coupling to the concentration mode enhances the local growth rate within the confined state. With the extended complex Ginzburg-Landau equations, the drift velocity of the pulses was greatly reduced for small Lewis number $\mathcal{L}$ (proportional to the linear damping α of the concentration mode). By analyzing the front interaction, it was shown that their stability required the pulses to travel opposite to the group velocity as seen in experiments. Furthermore, in [50, 51] they showed that the observed multiplicity of pulses and their stable/unstable ordering could be accounted for within the ECGL equations when effects from both the concentration mode and dispersion are present. It is noted that this set of ECGL equations also yields pulse

[2] Equation (1.7) is given in a frame moving with the group velocity. In a stationary frame the equation would read: $\partial_t A = -s\partial_x A + d\partial_x^2 A + \mu A + c|A|^2 A - p|A|^4$.

solutions when the bifurcation to extended waves is supercritical. Such a solution corresponds to a homoclinic solution in space, rather than a heteroclinic solution describing fronts.

1.2.3 Worms in Electroconvection in Nematic Liquid Crystals

More recently, two-dimensional localized waves have been observed in electroconvection of nematic liquid crystals (NLC) [52–55]. The orientation order of NLC leads to a preferred molecular alignment whose direction is indicated by the director $\hat{n}$. An experimental cell with uniform director alignment is obtained for NLC confined between two glass plates. For an AC voltage V applied across the plates exceeding a threshold V_c, the uniform conducting state loses stability to a traveling-wave convective state. Waves traveling at an oblique angle relative to the director $\hat{n}$, are labeled in the four directions as left- and right-traveling zig and zag waves. Experimental and analytical calculations indicate that the Hopf-bifurcation to extended waves is *supercritical*. However, stable, localized waves have been observed below onset of convection at V_c.

Figure 1.8 shows an experimental cell with several of these localized waves which were called "worms" due to their appearance [52]. The worms consist of only two waves, the zig and the zag waves both traveling either to the right or to the left. In the direction of the director $\hat{n}$, corresponding to the x-direction in Figure 1.8, the worms have long, variable lengths with a sharp amplitude maximum (head) at one end decreasing gradually over the length of the worm. In the perpendicular y-direction, the worms are short with a fixed width approximately one wavelength of the underlying pattern. Worms typically do not travel in the y-direction, but travel towards the head in the x-direction. The overall drift of the worm envelope is slow and in the direction opposite the underlying traveling waves.

Worm-structures were found in a complex Swift-Hohenberg model [56] in which localization is attributed to non-adiabatic effects. However, this model re-

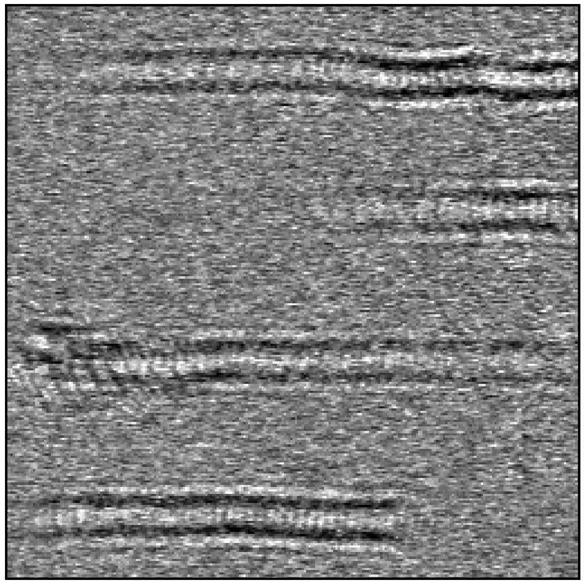

Figure 1.8: Experimental picture of localized worms in electroconvection of nematic liquid crystals [52]. Picture courtesy of Guenter Ahlers.

quired a subcritical bifurcation to extended waves resulting in a bistability between the basic state and the convective state. Hence, this description is unsuccessful in describing the appearance of worms below the onset of convection.

Results from the weak electrolyte model for electroconvection suggest that a slow charge-carrier mode may become dynamically relevant in the worm regime [57]. Motivated by the similarity to the slowly decaying concentration mode in binary-mixture convection and the result that it could lead to localized states when the primary bifurcation was supercritical, similar extended complex Ginzburg-Landau equations were suggested to describe the worms in electroconvection [58]

$$\begin{aligned}\partial_t A + \underline{\mathbf{u}}_A \cdot \nabla A &= \mu A + d_x \partial_x^2 A + d_y \partial_y^2 A + 2a\partial_{xy}^2 A \\ &\quad + fCA - c|A|^2 A - g|B|^2 A \qquad (1.11)\end{aligned}$$

$$\begin{aligned}\partial_t B + \underline{\mathbf{u}}_B \cdot \nabla B &= \mu B + d_x \partial_x^2 B + d_y \partial_y^2 B - 2a\partial_{xy}^2 B \\ &\quad + fCB - c|B|^2 B - g|A|^2 B \qquad (1.12)\end{aligned}$$

$$\partial_t C = \delta \Delta C - \alpha C + \underline{\mathbf{h}}_A \cdot \nabla |A|^2 + \underline{\mathbf{h}}_B \cdot \nabla |B|^2. \qquad (1.13)$$

A and B give the amplitudes of the zig and zag waves which advect the slow field C. The bifurcation to extended waves is supercritical at $\mu = 0$, but localized worm states were found already below onset. By considering two one-dimensional reductions of equations (1.11)-(1.13), it was found in [58] that the localization mechanisms are different in each direction. In the y-direction, the worm is comprised of a standing-wave pulse solution which itself exists below the threshold to extended waves. It represents a spatially homoclinic solution. In the x-direction, the worm can be constructed as bound fronts representing a heteroclinic solution connecting the basic state with this standing-wave pulse. This model seems to capture the essence of the worms observed, but further investigation is required to determine the relevance and identity of an additional mode.

1.3 Scope of Thesis

The investigations of localized structures presented in this thesis were motivated by the experiments described in sections 1.2.1-1.2.3. The thesis has essentially two parts comprising chapters 2 and 3. In chapter 2, oscillon-type structures are investigated within a modified Swift-Hohenberg model where the localization mechanism is quite general and can be attributed to non-adiabatic effects. The interaction between oscillons are studied and connections to the experiments are made. This work on oscillons is published in [59]. The second part of this thesis investigates the localization of traveling waves, when the system is subjected to an external resonant forcing. It is shown that this forcing itself leads to a new, tunable mechanism for localization. Further study of the effect of temporal forcing on structures localized via other mechanisms is also presented. Since the topics addressed in each chapter are quite separate, conclusions will be presented within the chapters. A brief summary and discussion concludes the thesis.

Chapter 2

Oscillons

In this chapter two main points are emphasized. First, it is demonstrated that oscillon-type patterns are neither specific to parametrically excited waves nor to granular media. By studying a suitable extension of the Swift-Hohenberg equation it is shown that stable oscillons may be expected quite generally in systems that undergo a sufficiently hysteretic transition to square patterns. The mechanism of localization is provided by non-adiabatic effects [3, 4, 60, 61]. In another study of a somewhat simpler Swift-Hohenberg equation [62] similar results were found. Presented here is a detailed investigation of the range of existence of oscillons and their bound states. Second, the general results are compared with the experimental observations and include comments on what may be expected in additional experiments . This will help determine whether in this specific experimental system additional mechanisms related to granular media are important, such as a coupling to an additional field [40].

The modified Swift-Hohenberg model is introduced and its relevance to vibrated granular layers is discussed in Section 2.1. The localization mechanism and existence range of oscillons are discussed in Section 2.2. The interaction of oscillons is studied in Section 2.3 followed by the conclusion in Section 2.4.

2.1 The Model

To study the connection between subcritical square patterns and oscillons a simple Swift-Hohenberg-type model is studied. Central for the richness of states observed in connection with oscillons is the fact that there are two types of oscillons with equal and opposite polarity. The two types are related by a reflection symmetry that arises from the discrete time-translation symmetry of the system. Within the framework of a Swift-Hohenberg equation this leads to the requirement that the equations be equivariant under the reflection $\psi \to -\psi$, where ψ is the amplitude. We therefore consider the following two-dimensional equation for the amplitude ψ that characterizes the pattern,

$$\begin{aligned} \partial_t \psi &= R\psi - (\nabla^2 + 1)^2 \psi + b\psi^3 - c\psi^5 \\ &\quad + e\nabla \cdot [(\nabla \psi)^3] - \beta_1 \psi (\nabla \psi)^2 - \beta_2 \psi^2 \nabla^2 \psi. \end{aligned} \tag{2.1}$$

As in the usual Swift-Hohenberg equation the basic state $\psi = 0$ becomes first unstable to a spatially periodic structure with wave number $q = 1$ at $R = 0$, where R is the control parameter. The choice of nonlinear terms is guided by the following considerations. Due to the reflection symmetry $\psi \to -\psi$ only odd powers of ψ are possible. In order to obtain a subcritical bifurcation the usual Swift-Hohenberg equation has to be extended to fifth order. If only the nonlinearities ψ^3 and ψ^5 are present no stable square patterns arise. The term proportional to e is chosen because it is known to favor square patterns [63, 2] and the terms proportional to the β_i's allow additional tuning possibilities.

Models of type (2.1) have been used to describe a wide range of patterns from Rayleigh-Bénard convection to wide-area lasers [2, 64]. The connection with the experiments on vibrated granular layers can be understood in the following way. In a weakly nonlinear framework one attempts to describe the standing waves by an expansion based on the mode that destabilizes the basic state with undeformed surface, $h = 0$. The surface deformation of a spatially periodic standing wave arising in a subharmonic instability can then be written as

$$h(\mathbf{r}, t) = A\, H_\omega(t)\, e^{i\omega t/2} e^{i\mathbf{q}\cdot\mathbf{r}} + c.c. + h.o.t., \tag{2.2}$$

where $H_\omega(t)$ has the same period as the driving, $2\pi/\omega$, and A is the small amplitude of the wave. In a Ginzburg-Landau approach the amplitude A would be allowed to vary slowly in space and time. In order to capture the non-adiabatic effects, which couple the slow and fast space dependence, no slow space dependence can be introduced. The order parameter ψ is therefore allowed to vary on a fast spatial scale, which incorporates the term $e^{i\mathbf{q}\cdot\mathbf{r}}$. The fast time dependence, however, is locked to the driving and can be kept outside the order parameter. From (2.2) it is apparent that the symmetry $t \to t + 2\pi/\omega$ induces the symmetry $\psi(\mathbf{r},t) \to -\psi(\mathbf{r},t)$ of the Swift-Hohenberg equation. Note that subharmonic instabilities are characterized by a single real Floquet multiplier, $\mu = -1$. Therefore, near onset the order parameter ψ, describing the excited waves, is real. An explicit derivation of a one-dimensional version of (2.1) from a periodically forced nonlinear Schrödinger equation has been performed in the context of phase-sensitive amplifiers of optical solitons [65] [1]. In that analysis damping is strong and the (strong) driving occurs periodically in a shock-like manner. This situation is very similar to that encountered in the granular system.

To obtain an overview of the periodic solutions of (2.1) we perform a weakly nonlinear analysis. The ansatz $\psi = Ae^{ix} + Be^{iy} + c.c. + h.o.t.$ yields the following amplitude equation

$$\begin{aligned} \partial_t A &= RA - \beta \mid A \mid^2 A - \gamma \mid B \mid^2 A \\ &\quad - \delta \mid A \mid^4 A - 2\rho \mid A \mid^2 \mid B \mid^2 A - \rho \mid B \mid^4 A, \qquad (2.3) \\ \partial_t B &= RB - \beta \mid B \mid^2 B - \gamma \mid A \mid^2 B \\ &\quad - \delta \mid B \mid^4 B - 2\rho \mid B \mid^2 \mid A \mid^2 B - \rho \mid A \mid^4 B, \qquad (2.4) \end{aligned}$$

where $\beta = -3b + 3e + \beta_1 - 3\beta_2, \gamma = -6b + 2e + 2\beta_1 - 6\beta_2, \delta = (-3b\beta_1 - 9e\beta_1 + 5\beta_1^2 - 11\beta_1\beta_2 + 480cd)/48d$, and $\rho = (-3b\beta_1 - e\beta_1 + 3\beta_1^2 - 7\beta_1\beta_2 + 120cd)/4d$. Thus the bifurcation to stripes and squares is subcritical for $\beta < 0$ and $\beta + \gamma < 0$, respectively. In determining the stability of steady-state solutions, equations (2.3-2.4) for real amplitudes A and B (i.e. $A \to Ae^{i\phi}$, A real) can be considered since they decouple from the equation for the phase. A steady square solution is defined

[1] In [65] $e = 0$ and $(\partial_x^2 + 1)^2\psi$ is replaced by $(\partial_x^2 - 1)^2\psi$.

by the amplitude

$$A^2 = B^2 = \frac{-(\beta+\gamma) \pm \sqrt{(\beta+\gamma)^2 + 4R(\delta+3\rho)}}{2(\delta+3\rho)} \tag{2.5}$$

which come into existence in a saddle-node bifurcation at $R_{sn} = -(\beta+\gamma)^2/4(\delta+3\rho)$. Similarly for stripes, the amplitudes are

$$A^2 = \frac{-\beta \pm \sqrt{\beta^2 + 4R\delta}}{2\delta}, \qquad B^2 = 0 \tag{2.6}$$

and the saddle-node point is $R_{sn} = -\beta^2/4\delta$. Linearizing the amplitude equations (2.3-2.4) about the steady pattern solutions leads to a pair of eigenvalues in each case. For squares, the eigenvalues are

$$\sigma_1 = -2(\beta+\gamma)A^2 - 4(\delta+3\rho)A^4 \tag{2.7}$$

$$\sigma_2 = -2(\beta-\gamma)A^2 - 4(\delta-\rho)A^4 \tag{2.8}$$

where A^2 for squares is given by the expression (2.5). The eigenvalues for stripe patterns are

$$\sigma_1 = -2\beta A^2 - 4\delta A^4 \tag{2.9}$$

$$\sigma_2 = (\beta-\gamma)A^2 + (\delta-\rho)A^4 \tag{2.10}$$

for A^2 given in (2.6). In both cases σ_1 is the eigenvalue associated with the saddle-node bifurcation and σ_2 is associated with the transition to the other mode (stripes or squares). The lower branch of solutions is unstable and only the solutions corresponding to the to upper '+' branch may be stable. Their relative stability can then be computed for a given set of parameter values. Motivated by the experiments, we focus on the regime in which the bifurcation to square patterns is subcritical. Unless otherwise noted, the bifurcation to stripes is also subcritical and squares are typically made more subcritical by taking $\gamma < 0$. Note that for $\beta-\gamma > 0$, if $\delta-\rho > 0$ then squares are stable. Then for large amplitude if $\delta-\rho < 0$ squares are unstable to stripes.

2.2 Oscillons

To investigate localized, oscillon-type solutions equation (2.1) is studied numerically using a pseudo-spectral code. A single oscillon can be seen in Figure 2.1. Figure 2.2 shows the region found numerically for the existence of localized states for several values of e for the case $\beta_1 = \beta_2$. Below the solid triangles, oscillons do not exist, whereas above the solid circles and squares the oscillons lose stability to extended stripes or squares, respectively. Also shown are the saddle-node bifurcations for squares and stripes.

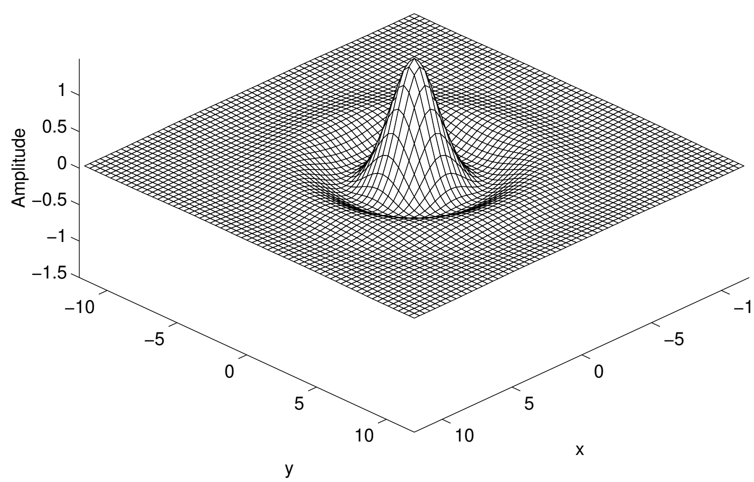

Figure 2.1: Single oscillon for the parameters $R = -0.5, b = c = 1.0, e = 0.75, \beta_1 = \beta_2 = 2.0$.

The mechanism involved in localizing these structures is now discussed. Consider an oscillon as an extremely small domain of a patterned state connected by fronts to the basic, unpatterned state. As discussed in the introduction, within the framework of a Ginzburg-Landau equation, fronts are stationary only for a single parameter value. In this setting, the interaction of fronts is attractive and such a localized state is unstable (cf. section 1.1, Figures 1.2-1.3 and [47, 5]). In [3]

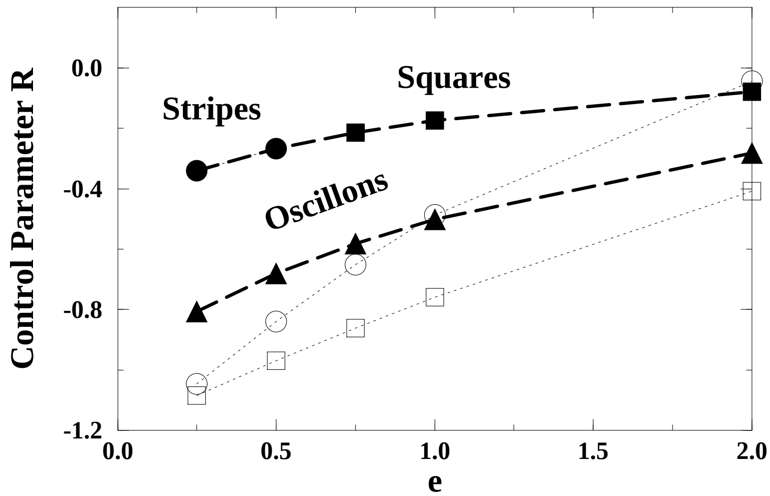

Figure 2.2: Numerically obtained saddle-node bifurcations for squares (open squares), stripes (open circles), and oscillons (solid triangle) along with the parameter values at which oscillons lose stability to extended squares (solid squares) or stripes (solid circles). The parameters are $b = c = 1.0, \beta_1 = \beta_2 = 2.0$.

the pinning of interfacial fronts by the interaction with the underlying small-scale periodic pattern has been pointed out. The pinning effect is examined in a more quantitative analysis in [4]. Their results are summarized below. Since the fast and slow spatial scales are not treated independently, the solvability condition describing the velocity of the front (1.3) is modified to be of the form

$$\frac{dX_0}{dt} = \frac{k_1}{2}(R - R_c) + \kappa(R)\cos(QX_0) \tag{2.11}$$

where X_0 is the position of the front and the cosine reflects the periodicity of the underlying pattern with wavenumber Q. The front can now be locked ($dX_0/dt = 0$) for a range of the control parameter, i.e. when $|R - R_c| \leq 2\kappa(R)/k_1$ which scales as $\kappa(R) \propto e^{-\alpha/\sqrt{R}}$. This same pinning was used to explain the existence of localized pulses in a one-dimensional quintic Swift-Hohenberg equation [61]. The same mechanism is expected to operate in two spatial dimensions. Hence, we also expect the range of existence of the oscillons to scale in a similar manner.

To confirm that the pinning is responsible for the localization, the dependence of the existence range of oscillons as a function of the coefficient c is investigated. Increasing the prefactor c of the quintic term causes both squares and stripes to become less subcritical. Figure 2.3a shows a phase diagram for the range of existence of the localized structures along with the numerical and analytical saddle-node curves for squares. Since squares become less subcritical, an increase in c necessitates an increase in R for finding oscillons. The oscillons have oscillatory tails that decay exponentially outward. As R is increased, the spatial decay of these tails becomes more gradual. Hence, the front locking becomes weaker and the localized solution loses stability to a periodic pattern. To demonstrate the scaling of the locking range, the range in the control parameter R where a single oscillon exists as a function of the inverse square root of the midpoint of this range is plotted. The log-linear plot in Figure 2.3b shows that the range does scale proportional to $e^{-\alpha/\sqrt{R}}$. This illustrates that the oscillons arise if the fronts are steep, i.e. if the basic state is strongly stable.

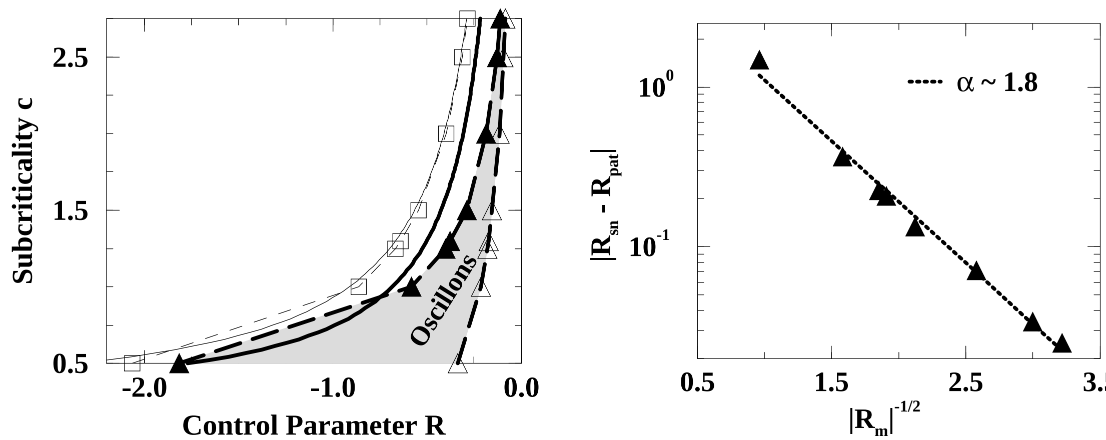

Figure 2.3: (a) Oscillons exist between the solid triangles and the open triangles. The numerical saddle-node bifurcation for squares (open squares) along with the analytical saddle-node curve (thin solid line) are shown. The thick solid line shows the analytical curve where $\Delta E = 0$ (cf. 2.12)). (b) The existence range of a single oscillon is plotted as a function of the inverse square root of the midpoint of the range. The dashed line is a fit to $\kappa e^{-\alpha/\sqrt{R_m}}$. The parameters are $b = 1.0, e = 0.75, \beta_1 = \beta_2 = 2.0$.

For $\beta_1 = \beta_2 \equiv 2f$ equation (2.1) possesses a Lyapunov Functional $\mathcal{L}$,

$$\mathcal{L} \;=\; \int dx\{-\frac{1}{2}R\psi^2 + \frac{1}{2}[(\nabla^2+1)\psi]^2 - \frac{1}{4}b\psi^4 + \frac{1}{6}c\psi^6$$

$$-\frac{1}{4}e(\nabla\psi)^4 + \frac{1}{4}f\psi^2\nabla^2(\psi^2)\} \equiv \int dx E(x) \tag{2.12}$$

with $\psi_t = -\delta\mathcal{L}/\delta\psi$. In this case the 'energy' difference ΔE between different states of the system governs the motion of a single front. For the stable zero state E is 0, while for squares it is $-RA^2/2 + (\beta+\gamma)A^4/4 + (\delta+3\rho)A^6/6$ within the weakly nonlinear theory (2.3-2.4). The values of R at which both states have the same energy ($\Delta E = 0$) and at which a single front would be stationary is shown as the thick curve in Figure 2.3a. The existence range of oscillons lies to the right of this curve, corresponding to parameters for which the square pattern has a lower energy. We attribute this difference to the attractive interaction between the fronts making up the oscillon.

The existence range of oscillons in the one-dimensional Swift-Hohenberg model was also investigated by varying the parameters c and R for the same parameters as used in the two-dimensional case of Figure 2.3. Figure 2.4a shows the bifurcation diagram for one-dimensional oscillons along with the saddle-node curves for the periodic pattern. Again the oscillon range of existence scales as $e^{-\alpha/\sqrt{R}}$. In contrast to the two-dimensional oscillons, $\alpha \sim 6.7$ is significantly larger for the one-dimensional oscillons. Hence, one-dimensional oscillons exist over a much smaller range in the control parameter R as is easily seen by comparing Figures 2.3a and 2.4a.

When the 2-dimensional oscillon loses stability to an extended pattern state, stripes or squares emerge depending on other parameters. Figure 2.5 shows intermediate stages for a single oscillon in the center evolving to stripes and squares, respectively. As can be seen in the transition to stripes, the oscillon tends to elongate in one direction and generate small stripes in the other direction, eventually filling the entire space with stripes. Note that the square pattern, although being unstable to stripes, still exists in this regime (cf. Figure 2.2). The transition to squares is generally characterized by more oscillons appearing on the perimeter of the initial oscillon. These features seen in the numerical simulations are similar to the transitions observed in the experimental granular system.

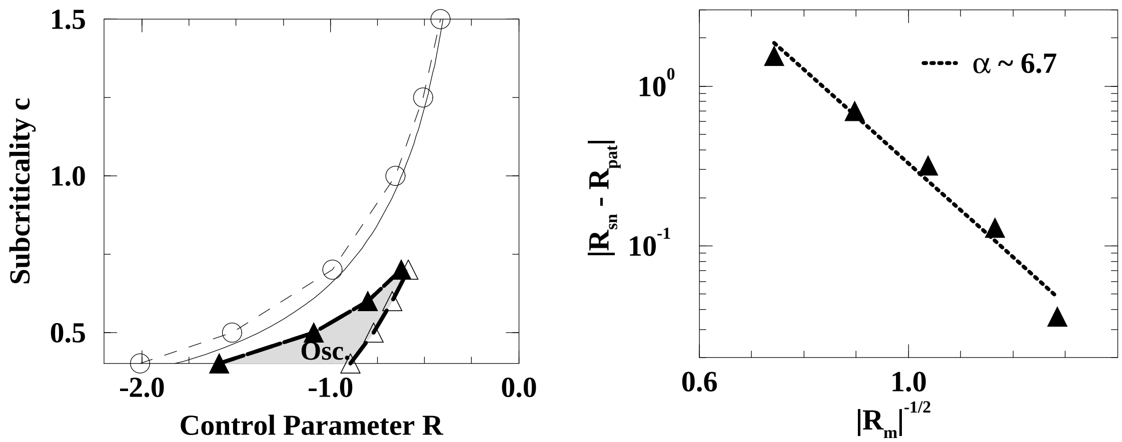

Figure 2.4: (a) One-dimensional oscillons exist between the solid triangles and the open triangles. The numerical saddle-node bifurcation for one-dimensional stripes (open circles) along with the analytical saddle-node curve (thin solid line) are shown. (b) The existence range of a single one-dimensional oscillon is plotted as a function of the inverse square root of the midpoint of the range. The dashed line is a fit to $\kappa e^{-\alpha/\sqrt{R_m}}$. The parameters are the same as Figure 2.3.

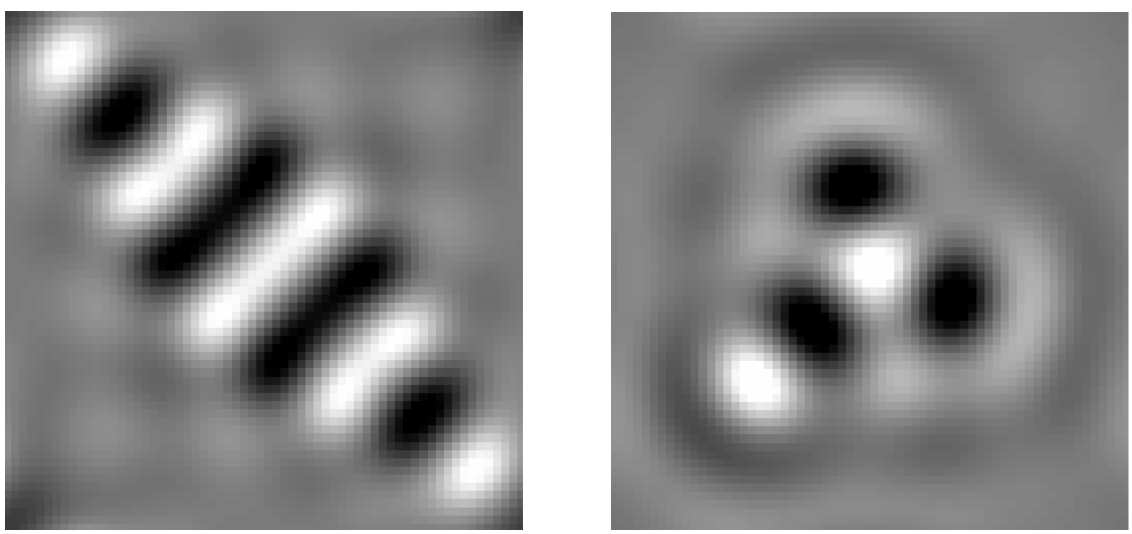

Figure 2.5: The transition to stripes (a) and squares (b) starting from a single oscillon in the center. The parameters are $b = c = 1.0, \beta_1 = \beta_2 = 2.0$ and for (a) $R = -0.264, e = 0.5$ and (b) $R = -0.205, e = 0.75$.

Other, more complicated extended patterns were also sometimes found when the control parameter R was incremented by larger amounts. Figure 2.6

shows snapshots at four different times leading to the steady solution observed at time ~ 545. The emerging pattern seems to arise from competing wavelengths of the underlying pattern and the system size.

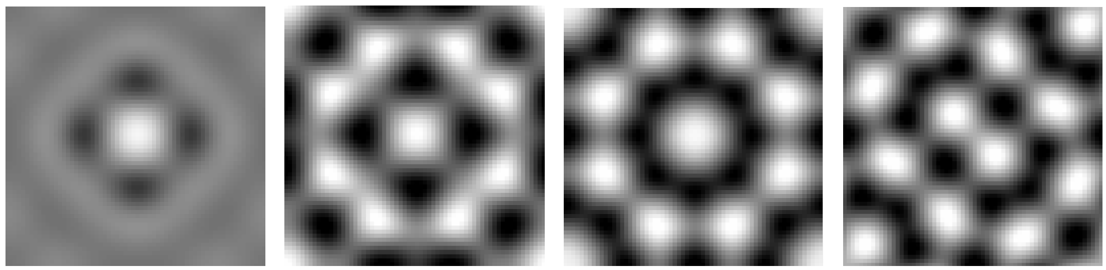

Figure 2.6: The transition to a more complicated pattern from a single oscillon when the control parameter is changed from $R = -0.35$ to $R = -0.10$. The snapshots from left to right are at time $28, 49, 93$, and 545. The parameters are $b = c = 1.0, e = 2.0, \beta_1 = 0.0, \text{and} \beta_2 = 2.0$.

To investigate whether the general locking mechanism is sufficient to explain the experiments or whether aspects have to be taken into account that are specific to the granular system, these findings are compared with the experimental results in more detail. The experimental phase diagram in Figure 2.7 [1] shows that oscillons exist only below the patterns for a mid-range of frequencies. Increasing the driving amplitude Γ, patterns appear at the solid diamonds. For decreasing Γ, extended patterns disappear at the solid circles to become either the flat layer or oscillons which exist all the way to the solid squares. Within the minimal framework presented here, oscillons are expected to exist where squares are strongly subcritical, i.e. where the square pattern coexists with a strongly stable basic state. However, in the low frequency range where squares exhibit large hysteresis, oscillons are not seen experimentally. The following explanation is proposed. In the experiments, the driving amplitude is increased into the pattern regime which results in a pattern with wavenumber close to the critical wavenumber. Then the amplitude is decreased and oscillons emerge depending on where the pattern with this wave number goes unstable. Figures. 2.8a,b show the neutral stability curve for the basic state $\psi \equiv 0$ and the numerically determined range over which square patterns (restricted to a

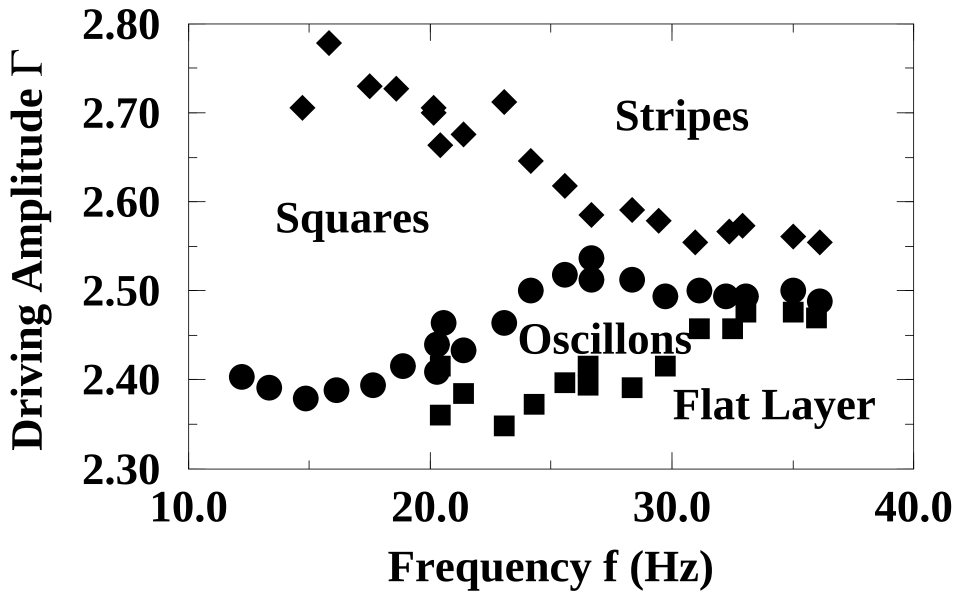

Figure 2.7: The experimental phase diagram [1]. For increasing Γ, patterns appear at the solid diamonds. As Γ is decreased the extended patterns exist until the solid circles beyond which oscillons exist in the mid-frequency range until the solid squares.

system size of one wavelength) are stable, along with the range in R where oscillons exist for two sets of parameter values. Decreasing R below the values marked by solid squares, the amplitude of the square pattern goes to zero in a saddle-node bifurcation. The open squares indicate the values of R where the square pattern seems to undergo an instability involving the wavelength of the pattern. As the control parameter R is decreased, squares remain in existence until the solid saddle-node points, although they may lose stability earlier. Note that we do not associate a wavenumber q with the oscillon and the shaded region refers only to the R-values where oscillons exist. In Figure 2.8a the oscillon range extends below the saddle-node for squares in particular for wavenumbers close to $q_c = 1$, so that oscillons are expected as R is decreased below the existence of squares. This is indicated by the arrow. In contrast, Figure 2.8b shows a situation in which the oscillon range is above these points near $q_c = 1$, and one does not expect to obtain oscillons by decreasing R further below the saddle-node.

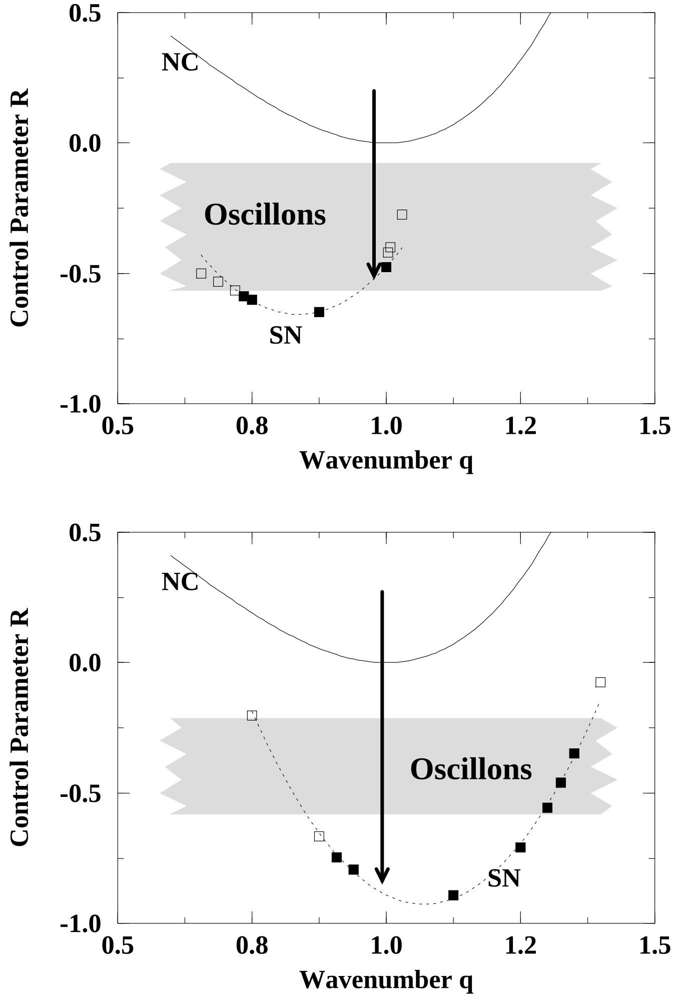

Figure 2.8: The neutral stability curve for the basic state and the numerical saddle-nodes for squares (solid squares) are shown as a functions of the wavenumber q. Open squares denote cases where the single square loses stability. The shaded region indicates the range in R where oscillons exist. For the parameters $b = c = 1.0, e = 4.0, \beta_1 = 0.0, \beta_2 = 2.3$ (a), the oscillons exist for values of the control parameter below the saddle-node for squares. For the parameters $b = c = 1.0, e = 0.75, \beta_1 = \beta_2 = 2.0$ (b), the oscillons no longer exist before the saddle-node for squares is reached by decreasing R.

Figure 2.9 shows the bifurcation diagram obtained from numerical simulations of (2.1) for the same parameters as in Figure 2.8a. Note that stripes are supercritical in this case. Here we see that a single oscillon exists for a range of R-values below the saddle-node for the square pattern with wavenumber $q = 1$.

Starting with an extended square pattern with wavenumber q = 1, adding a small

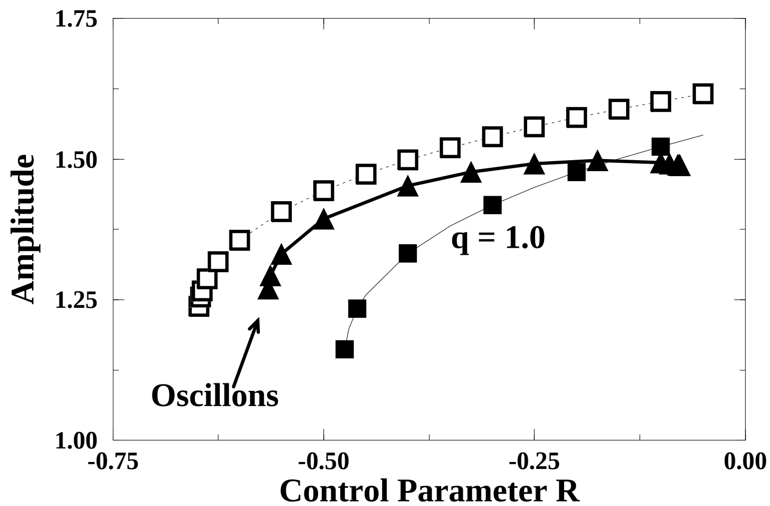

Figure 2.9: Bifurcation curves obtained for a single oscillon (solid triangles) and squares with $q = 1.0$ (solid squares) and $q = 0.875$ (open squares). Parameters are $b = c = 1.0, e = 4.0, \beta_1 = 0.0, \beta_2 = 2.3$ (cf. Figure 2.8a).

uniform random perturbation, and then decreasing the control parameter below the saddle-node, we find that the pattern breaks down and some oscillons persist. Random perturbations to the square pattern result in a competition between a change in the wavelength and decay of the pattern to the zero state, leading to patches of both in the system. The resulting pattern is better described as a collection of oscillons. The top row of Figure 2.10 shows a case in which several oscillons survive, while the bottom row of Figure 2.10 shows a case in which only one oscillon remains. These results are consistent with the observation of oscillons existing in the parameter regime below where the periodic patterns exist in the granular experiments.

In light of the experiments for lower frequencies, the oscillons may still exist, but their range of existence may be 'embedded' in the range of existence for squares as suggested by Figure 2.8b.[2] In that case the oscillons would not be accessible by changing the amplitude of forcing. We suggest that oscillons may be

[2]It is also conceivable that despite the increase of the hysteresis, the flat state becomes less stable with decreasing frequency thus decreasing the oscillon range.

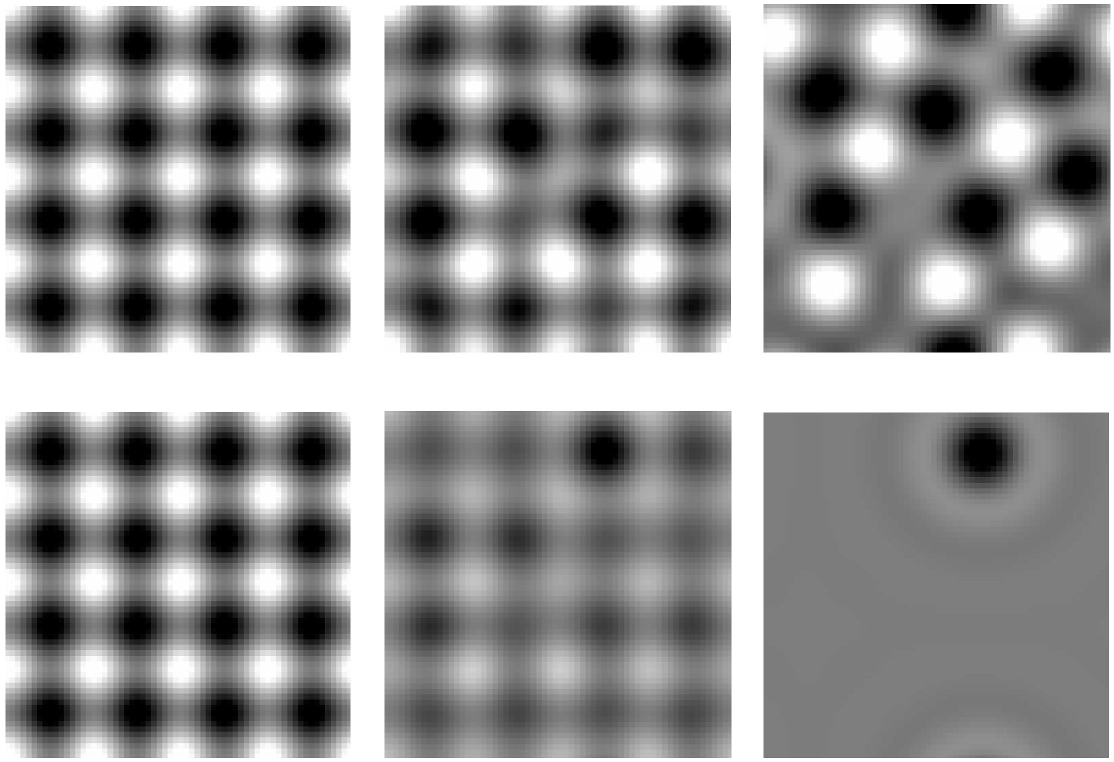

Figure 2.10: Time evolution of an initially perturbed square pattern ($q = 1$) with $R = -0.45$. Top row: R is decreased to -0.48 and parts of the pattern decay, but several oscillons persist ($t = 0, 15, 1000$). Bottom row: R is decreased to -0.504 resulting in a rapid decay of the pattern and only one surviving oscillon ($t = 0, 10, 2000$). All other parameters as in Fig 2.8a.

accessible in this regime by starting with an oscillon in the mid-frequency range and then decreasing the frequency.

As mentioned in the introduction, coupling to an additional field can lead to robust localized structures which may even exist below the bifurcation to extended patterns. Hence, the existence of oscillons below threshold can also be explained in the model proposed in [40] where the oscillation amplitude is coupled to the local average mass density.

2.3 Interaction of Oscillons

Since the oscillons have oscillatory tails that decay exponentially outward, one expects them to interact and form bound states. Figure 2.11 shows several of these bound states found in the numerical simulations which are similar to states observed in the experimental system. These include dipoles, tetramers, and chains of alternating polarity. In the overdamped exponential case (i.e. $(\partial_x^2 - 1)^2\psi$) [65],

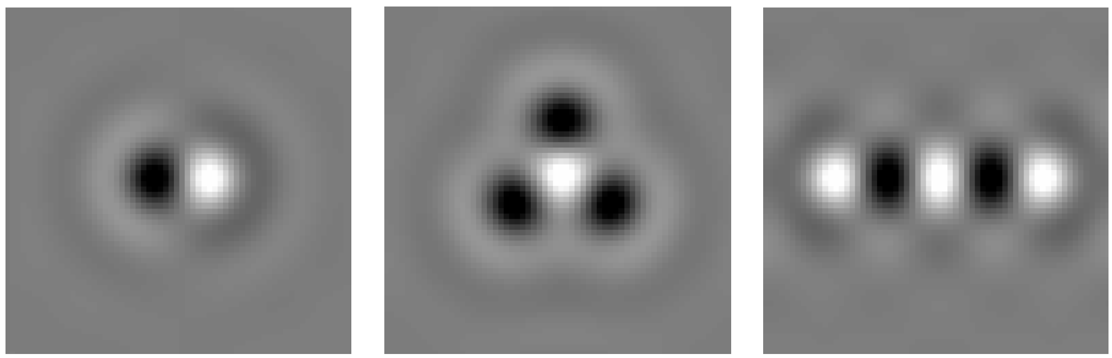

Figure 2.11: Bound states of opposite polarity: (a) dipole, (b) tetramer, and (c) chain of 5 alternating oscillons for the parameters as in Figure 2.1.

the existence and stability of multiple pulses in one dimension has been studied in [66].

In addition to seeing oscillons of opposite polarity binding, we also find bound states of like polarity, which have not been seen in the granular experiments. The separation distance between like pairs is greater than for opposite pairs. As can be seen in the cross-section of a like pair in Figure 2.12b, the spatial oscillations between the pair lock the two oscillons together, but do not create a third negative oscillon between them as can be seen by comparison with the $+-+$ chain (dashed line). However, increasing the parameter R causes the oscillations to decay slower in space. Eventually a value of R is reached where the minimum exceeds a threshold beyond which the amplitude grows to form an oscillon of opposite polarity and becomes a $+-+$ chain.

Figure 2.13 shows the existence range of $++$ structures for two values of c

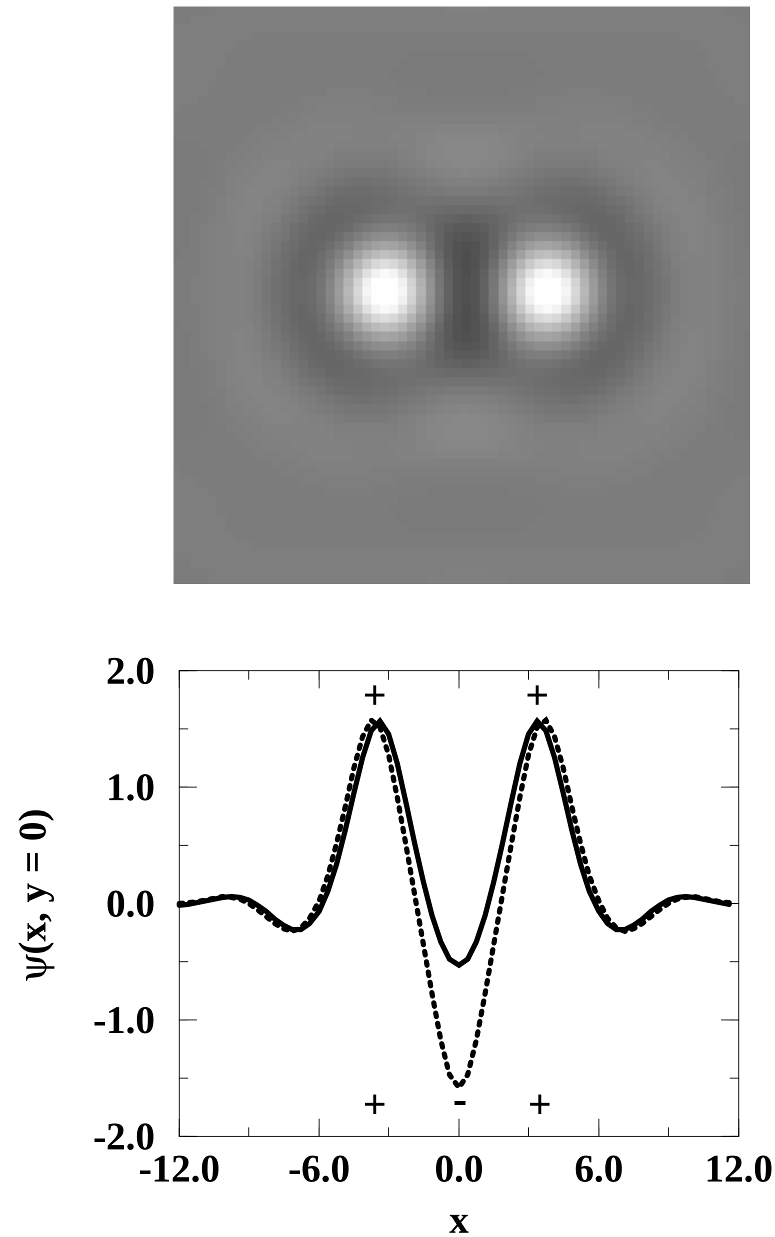

Figure 2.12: (a) Two bound oscillons of like polarity and (b) their cross-section (solid line) along with the cross-section for a chain of alternating polarity (dashed line). For the pair $R = -0.470$ while for the chain $R = -0.469$. All other parameters as in Figure 2.1.

(dark region). The border between the dark and grey regions marks the transition to a $+-+$ structure. To the right of the grey region the $+-+$ chain evolves to a periodic pattern. This result shows that the ratio of the like-pair range to the single-oscillon range is greatly reduced by slightly increasing c which decreases the subcriticality. Increasing c further makes it difficult to find a stable ++ structure. We expect that a bound pair of like polarity may be similarly difficult to find in experiments because they exist only over a small range. Conversely their range of existence may be larger in regions of stronger stability of the basic state.

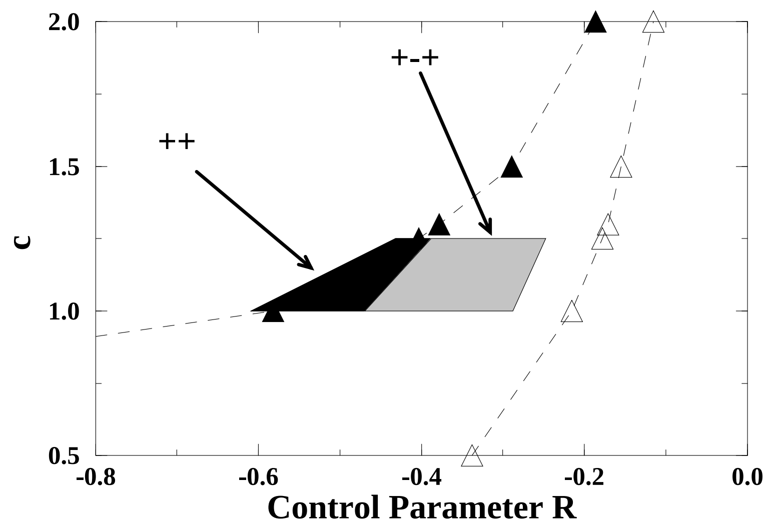

Figure 2.13: Existence range for a pair of like oscillons is shown in black. The left side of the grey region marks the transition to a chain of three oscillons of alternating polarity (cf. Figure 2.12b). The $+-+$ chain persists up to the right end of the grey area. Parameters are as in Figure 2.3.

Since the peak-to-peak distance for two like pulses is greater than that for two pulses of opposing amplitude, we expect the binding between the ++ state to be much weaker than the binding of the $-+$ state. In order to study the 'strength' of the binding, bounded noise was added to the solution at each time step and the peak-to-peak distance was measured. The results for several noise strengths are shown in Figure 2.14. Figure 2.14a shows that the opposing pair remains bound for all three noise levels. In contrast, Figure 2.14b shows that the like pair is more susceptible to the same values of noise. In fact, for the mid-level noise, the like pair creates a third negative oscillon in the center and for the highest-level noise, the pair quickly loses stability and by time 200 has become two perpendicular chains of alternating polarity. The effect of noise in the experimental system combined with the small existence range for oscillons of like polarity may contribute to them not being observed in the experiments.

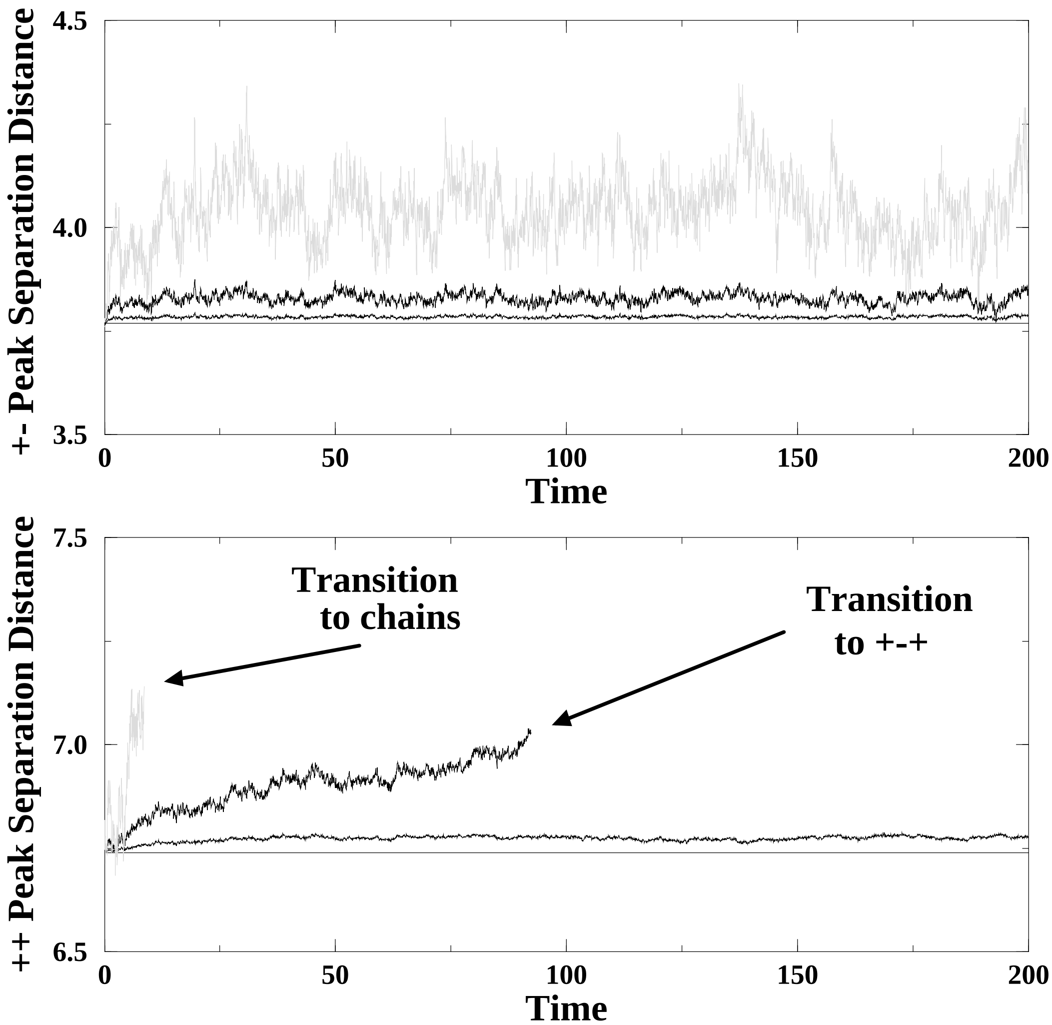

Figure 2.14: (a) The peak-to-peak distance for a pair of oscillons of opposite polarity is plotted for the unperturbed pair (straight line) and for three added noise levels, 0.075 (bottom), 0.15 (middle), 0.3 (top, grey). (b) The same is plotted for a like pair. The parameters are as in Figure 2.1.

The interaction of like pairs can also result in forming triad structures of two like oscillons bound to a third opposite oscillon in a triangular pattern as shown in Figure 2.15. The triad breaks the spatial reflection symmetry and in this non-potential case the triad travels in the direction of the two leading oscillons.

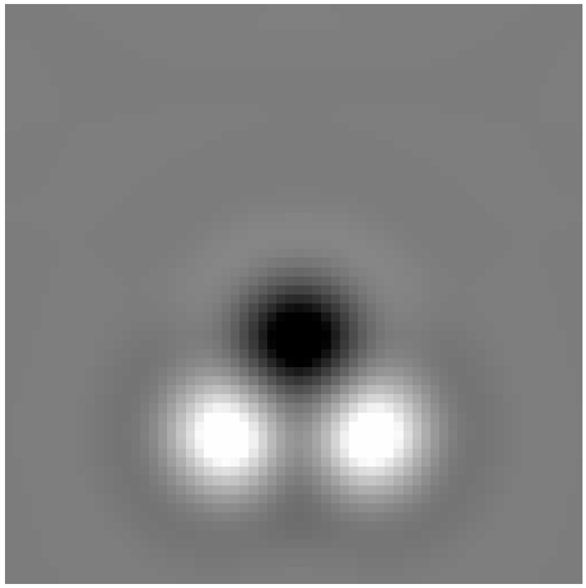

Figure 2.15: Triad propagating downward for $R = -1.5, b = c = 1.0, e = \beta_2 = 4.0, \beta_1 = 0.0$.

2.4 Conclusions

The results of investigating a Swift-Hohenberg model for the existence of two-dimensional localized oscillons has been presented. Since the subharmonic response results in the reflection symmetry $\psi \to -\psi$, one obtains equal oscillons of opposite polarity. Oscillon-type structures are a general feature to be expected in systems where the transition to squares is subcritical and the basic state is sufficiently stable so as to allow localization caused by the interaction of the large-scale envelope with the small-scale underlying periodic pattern. Hence the observance of oscillons should not be restricted to granular materials. For example, one would also expect them to be accessible in Faraday experiments of shear-thinning fluids for which the viscosity decreases with the flow, which should make the transition subcritical [67, 68]. Subsequently, oscillons were found experimentally in vertically vibrated colloidal suspensions which exhibit a subcritical transition to square patterns [69]. Their existence range was found to scale as $e^{-\alpha/\sqrt{R}}$, consistent with the nonadiabatic locking mechanism. Furthermore, they observed oscillons of like polarity interacting to form bound states. The impact of noise is weaker in the colloidal suspensions that in granular material. It is therefore reasonable to assume that the noise in colloidal suspensions is insufficient to unbind the like-pairs as may be occurring in the granular system.

Further comparison with the granular experiments will show whether this general mechanism is sufficient to capture the observed oscillon or whether additional physical mechanisms like a coupling to an additional slow mode are relevant [40, 58]. Experimental tests to determine the validity of this minimal framework involve the range of existence of oscillons and of like-pairs in the low-frequency range. Oscillons may be observable experimentally in the low-frequency regime by changing the experimental protocol. Bound states of like-polarity are shown numerically to be not as robust as those of opposite polarity. The existence of bound states of like-polarity may be larger in regions of greater subcriticality, e.g. lower frequencies, and their observance more likely.

Chapter 3

Periodically Forced Waves

For traveling waves it is well known that the external application of a resonant temporal forcing excites the counterpropagating wave [70–72]. As mentioned in the introduction, coupling the amplitude to an additional mode such as the phase for the parity-breaking bifurcation and the slowly decaying concentration field for binary-mixture convection can lead to localized structures. A natural question is therefore whether the periodic forcing and the resulting counterpropagating wave can play a similar role and lead to the localization of the traveling wave into a pulse. Since the temporal forcing is easily controlled externally this localization mechanism would be *tunable*.

This chapter investigates the effect of time-periodic forcing on spatially localized waves. First the effect of forcing on the interaction of fronts in the absence of other localization mechanisms is considered and it is shown that forcing alone can lead to localized structures. This new localization mechanism can stabilize pulses with either a repulsive or an attractive interaction. While the interaction strength between fronts is usually determined by the system parameters, forcing allows the strength to be controlled externally. To focus on the interaction of the fronts due to the temporal forcing, the front equations are derived in Section 3.1 in the absence of dispersion so that all of the coefficients of the Ginzburg-Landau equations are real. Section 3.2 is a discussion of the resulting front equations and comparison with numerical calculations. Section 3.3 extends the analysis and discussion to include holes and multiple pulses. The combined effect of temporal forcing and other localization mechanisms is investigated in Sections 3.4 and 3.5 and the conclusion is presented in Section 3.6.

3.1 Derivation of the Front Equations

Motivated by the pulses observed in binary mixture convection (c.f. Section 1.2.2), a subcritical bifurcation to traveling waves is considered. The velocity is expanded in terms of the amplitudes A and B, of the left and right traveling waves

$$v = A(x,t)e^{i(q_c\tilde{x}-\frac{\omega_e}{2}\tilde{t})} + B(x,t)e^{-i(q_c\tilde{x}+\frac{\omega_e}{2}\tilde{t})} + c.c. + h.o.t. \tag{3.1}$$

where $\tilde{t}$ and $\tilde{x}$ are the fast time and space coordinates. The amplitudes A and B are allowed to vary on a slow time scale t and a slow spatial scale x. Using the translation and reflection symmetry of the system, one can determine the form of the amplitude equations for A and B. An external resonant forcing $\nu e^{i\omega_e\tilde{t}}$ at twice the Hopf frequency, $\omega_e = 2\omega_h$, is introduced. This forcing excites the oppositely traveling waves and breaks the time translation symmetry, resulting to lowest order in a linear coupling between the two wave amplitudes [70–72]. Hence the following set of coupled Ginzburg-Landau equations are studied as a model describing the system.

$$\begin{aligned}
\partial_t A &= -s\partial_x A + \epsilon^2 d_2 \partial_{xx} A + \mu A + c|A|^2 A - p|A|^4 A \\
&\quad -g|B|^2 A - r|A|^2|B|^2 A - u|B|^4 A + \nu B^* && (3.2) \\
\partial_t B &= +s\partial_x B + \epsilon^2 d_2 \partial_{xx} B + \mu B + c|B|^2 B - p|B|^4 B \\
&\quad -g|A|^2 B - r|A|^2|B|^2 B - u|A|^4 B + \nu A^* && (3.3)
\end{aligned}$$

where the coefficient ν and the group velocity s are real. Otherwise all other coefficients may be complex. However, to focus on the interaction of the fronts due to temporal forcing, the front equations are derived for the case in which all of the coefficients are real, i.e. neglecting dispersion and detuning. Nonlinear gradient terms which would also appear in the leading order equations (3.2-3.3) have also been neglected. In order for the bifurcation to be weakly subcritical, the cubic coefficients must be small enough to balance the quintic terms. Equations (3.2-3.3) have been suitably rescaled such that the control parameter μ and the amplitudes A and B are $\mathcal{O}(1)$. If the usual scaling $x = \epsilon\tilde{x}$ is used to obtain the complex Ginzburg-Landau equations in which the growth term μA is balanced by the diffusive term $d\partial_{xx}A$, then for large group velocity, the scaling of $s\partial_x A$ is inconsistent with the rest of the equation, i.e. it is of *lower*-order. However, by considering slower spatial scales $x = \epsilon^2\tilde{x}$, the advective term $s\partial_x A$ is of the same order as μA and the diffusive term then appears in the re-scaled equations (3.2-3.3) as a higher-order correction ($\mathcal{O}(\epsilon^2)$) [73].

As discussed in the introduction, one contribution to the interaction between fronts in the convective amplitude arises from their overlap. For large distances it is small, inducing a weak attractive interaction which destabilizes pulses. However, since here the diffusion is weak ($\mathcal{O}(\epsilon^2)$), resulting in steep fronts in A, the overlap between the fronts is higher order in ϵ and the associated interaction can be ignored. Hence the interaction between fronts is dominated by the presence of the oppositely traveling wave excited by the periodic forcing. The small diffusion coefficient causes internal layers to arise at the positions of the fronts. The two bound fronts are then divided into the five regions sketched in Figure 3.1, where x_L and x_R give the positions of the left and right fronts. Within regions I, III, and V the amplitude of A is constant. Regions II and IV are regions of rapid change where the dynamics of the fronts are determined. The small ϵ scale characterizes the width of the internal layers. However, their width is still large relative to the critical wavelength of the traveling waves.

We consider the forcing to be small, $\nu = \mathcal{O}(\epsilon)$, so that the corresponding amplitude B of the now excited left traveling wave is of the same order in $\epsilon \ll 1$. The amplitudes and the parameters μ and ν are expanded as

$$\begin{aligned} A &= A_0 + \epsilon A_1 + \cdots, \quad & B &= \epsilon B_1 + \cdots, \\ \mu &= \mu_c + \epsilon^2 \mu_2 + \cdots, \quad & \nu &= \epsilon \nu_1 + \cdots. \end{aligned} \tag{3.4}$$

where $\mu_c = -3c^2/16p$ is the value of the control parameter at which a single, non-

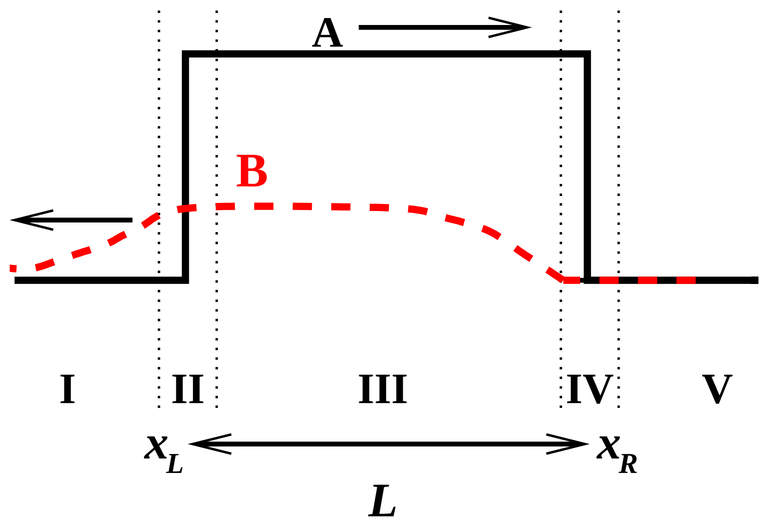

Figure 3.1: Sketch of a pulse traveling to the right. A is the amplitude of the right-traveling wave. Temporal forcing excites the left-traveling wave so that B grows spatially to the left reaching a maximum at the trailing front, behind which it decays exponentially.

interacting front is stationary. For $\mu > \mu_c$, the nonlinear convective state invades the basic state. The positions x_R and x_L of the right and left fronts move on the slow time scale $T = \epsilon^3 t$. Consider a frame of reference moving with the group velocity s and substitute these expansions into equations (3.2-3.3). Then the leading order equations for A and B in the outer regions I, III, and V are

$$0 = \mu_c A_0 + cA_0^3 - pA_0^5, \tag{3.5}$$

$$0 = 2s\partial_x B_1 + \mu_c B_1 + \nu_1 A_0 - gA_0^2 B_1 - uA_0^4 B_1. \tag{3.6}$$

Solving equation (3.5) results in $A_0 = 0$ in regions I and V and $A_0^2 = A_c^2 = 3c/4p$ in region III. The corresponding solution to (3.6) is

$$B_1^j(x) = \frac{\nu_1}{\alpha} A_0^j + K^j e^{\frac{\alpha^j}{2s} x}, \tag{3.7}$$

where j corresponds to the regions I, III, and V and $\alpha^j = -\mu_c + gA_0^{j^2} + uA_0^{j^4}$.

In the inner regions II and IV, the solutions vary on a fast space scale x/ϵ which is captured by introducing the inner coordinates $\eta = (x - x_L)/\epsilon$ and

$\eta = (x_R - x)/\epsilon$, respectively. The spatial derivative then transforms as $\partial_x \to \pm\partial_\eta/\epsilon$. The resulting leading-order equations for A and B are

$$0 = d_2\partial_{\eta\eta}A_0 + \mu_c A_0 + cA_0^3 - pA_0^5, \tag{3.8}$$

$$0 = \pm 2s\partial_\eta B_1. \tag{3.9}$$

From (3.8) one obtains the left and right front solution

$$A_0(\eta) = A_c\sqrt{\frac{1}{2}\left[1 + \tanh\left(\frac{\eta}{\xi}\right)\right]}, \qquad \xi = \frac{4}{c}\sqrt{\frac{pd_2}{3}} \tag{3.10}$$

where A_c^2 and η are defined above. Equation (3.9) implies that B_1 does not depend on the fast space variable η, i.e. $B_1 = B_c^{I,IV}$ constant in regions II and IV. At $\mathcal{O}(\epsilon)$, no inhomogeneity arises in the equation for A_1, which is therefore taken to be identically 0. But at $\mathcal{O}(\epsilon^2)$ the following equation for A_2 is obtained:

$$\mathcal{L}A_2 = \mp\frac{dx_{L,R}}{dT}\partial_\eta A_0 - \mu_2 A_0 + gB_1^2 A_0 + rA_0^3 B_1^2 - \nu_1 B_1, \tag{3.11}$$

where $\mathcal{L} = d_2\partial_{\eta\eta} + \mu_c + 3cA_0^2 - 5pA_0^4$ is the linearized operator. The singular operator $\mathcal{L}$ has a zero-eigenmode $\partial_\eta A_0$, which leads to a solvability condition for equation (3.11). The result of projecting equation (3.11) onto the zero-eigenmode determines the velocity of the fronts in regions II and IV,

$$\pm\frac{dx_{L,R}}{dT} = \left[-2(\mu - \mu_c) + (2g + A_c^2 r)B_c^{II,IV^2} - \frac{4\nu_1 B_c^{II,IV}}{A_c}\right]\xi \tag{3.12}$$

with $B_c^{II,IV}$ yet undetermined.

Since B is generated by A, we consider the case where $B = 0$ ahead of a pulse traveling to the right (i.e. region V where $A \equiv 0$). This implies that $K^V = 0$ from equation (3.7). Now matching the inner and outer solutions for B at the left and right positions (x_L and x_R) of the fronts, one obtains the constant values $B_c^{II} = (\nu_1 A_c/\alpha)\left[1 - \exp(-\alpha L/2s)\right]$ and $B_c^{IV} = 0$. The constants K^I and K^{III} are nonzero and we see from equation (3.7) that B grows spatially to the left in region

III and approaches the limiting value $\nu_1 A_c/\alpha$. Then in region I where the pulse has passed and A again equals 0, B decays exponentially to zero. The individual front velocities are given by substituting the values of $B_c^{II,IV}$ into the expressions given in (3.12)

$$\frac{dx_L}{dT} = \left[-2(\mu-\mu_c) + \frac{\nu^2(2g + A_c^2 r)A_c^2}{\alpha^2} - \frac{4\nu_1^2}{\alpha}\right]\xi, \tag{3.13}$$

$$\frac{dx_R}{dT} = +2(\mu-\mu_c)\xi. \tag{3.14}$$

Combining these results yields the following equations describing the evolution of the pulse length $L = x_R - x_L$ and the velocity of the pulse relative to a frame moving with the group velocity s in terms of a "center of mass" coordinate $M = (x_R + x_L)/2$,

$$\frac{dL}{dT} = k_1(\mu-\mu_c) + k_2\nu^2(1 - e^{-\frac{\alpha}{2s}L}) - k_3\nu^2(1 - e^{-\frac{\alpha}{2s}L})^2, \tag{3.15}$$

$$\frac{dM}{dT} = \frac{1}{2}\left[-k_2\nu^2(1 - e^{-\frac{\alpha}{2s}L}) + k_3\nu^2(1 - e^{-\frac{\alpha}{2s}L})^2\right], \tag{3.16}$$

where $k_1 = 4\xi$, $k_2 = 4\xi/\alpha$, and $k_3 = [(2g + A_c^2 r)A_c^2\xi]/\alpha^2$. While both k_1 and k_2 are always positive, k_3 may be either positive or negative. As will be seen in the next section, the sign of k_3 determines whether stable pulse solutions may exist. The interaction length is given by $2s/\alpha$.

3.2 Discussion of Front Equations

The possible pulse solutions of (3.15-3.16) are more easily discussed in terms of the quantity $\Lambda \equiv [1 - \exp(-\alpha L/2s)]$ which monotonically increases from zero to one as L increases from zero to infinity. Equation (3.15) is then given by

$$\frac{1}{1-\Lambda} \cdot d\Lambda/dT = f(\Lambda) \equiv k_1(\mu-\mu_c) + k_2\nu^2\Lambda - k_3\nu^2\Lambda^2. \tag{3.17}$$

Figure 3.2 shows the parabola opening downward for $k_3 > 0$, depicting $f(\Lambda)$ for the two cases $\mu > \mu_c$ and $\mu < \mu_c$. The maximum occurs at $\Lambda = k_2/2k_3$ independent of forcing strength ν. Fixed points Λ_0 are indicated where $f(\Lambda) = 0$:

$$\Lambda_0 = (1 - e^{-\frac{\alpha}{2s}L_0}) \equiv \frac{k_2 \pm \sqrt{k_2^2 + \frac{4(\mu-\mu_c)k_1k_3}{\nu^2}}}{2k_3} \tag{3.18}$$

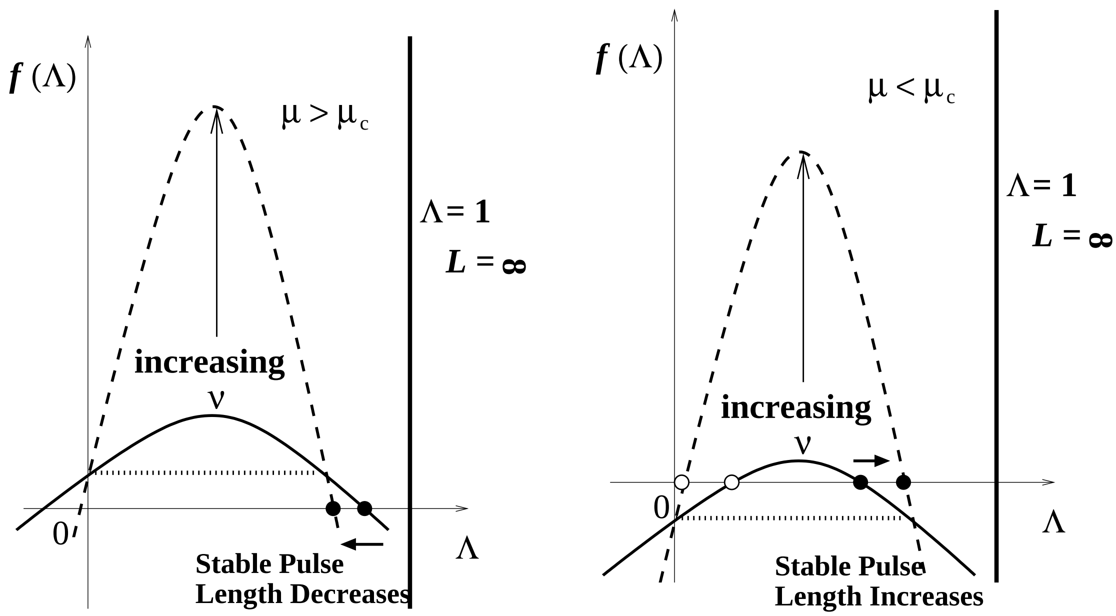

Figure 3.2: Sketch of $f(\Lambda) \equiv k_1(\mu - \mu_c) + k_2\nu^2\Lambda - k_3\nu^2\Lambda^2$ for $k_3 > 0$. Stable (unstable) fixed points are indicated by solid (open) circles. Varying forcing changes the steepness of the parabola and the height of the maximum located at $\Lambda = k_2/2k_3$. Increasing forcing ν decreases the stable pulse length for (a) $\mu > \mu_c$ and increases the stable pulse length for (b) $\mu < \mu_c$.

A linear stability analysis shows that a pulse with $\Lambda = \Lambda_0$ is stable if $f'(\Lambda_0) < 0$. If $k_3 < 0$, the parabola is opening upward with the minimum at $\Lambda = k_2/2k_3 < 0$ so that $f'(\Lambda) > 0$ for all values of $\Lambda > 0$. Hence a stable pulse may exist only if $k_3 > 0$ and in this case corresponds to the upper branch of equation (3.18). If the coefficients are such that the minimum at $k_2/2k_3$ is near one, then the stable pulse length is near infinity. For $k_2/2k_3$ greater than one, only the unstable lower branch of solutions exists. Unless otherwise stated the discussion of the front interaction will focus on the regime $0 < k_2/2k_3 < 1$ where a stable branch exists.

From the expression (3.18) and the parabola in Figure 3.2, one can easily see the effect of forcing on the stable pulse length. When $\mu = \mu_c$, ν no longer appears in this expression and the pulse length remains constant (L_c satisfying $\Lambda_0 = k_2/k_3$) as the forcing varies. As the forcing ν increases, $f(0) = f(k_2/k_3) = k_1(\mu - \mu_c)$ remains fixed while the parabola steepens (see Figure 3.2). Thus for $\mu > \mu_c$ the stable pulse length is larger than L_c, but approaches the equilibrium length L_c as forcing increases (Figure 3.2a). Conversely, for $\mu < \mu_c$ the pulse length increases to L_c with increasing ν (Figure 3.2b). As forcing ν decreases for $\mu > \mu_c$, the pulse length increases and eventually diverges to infinity. In contrast, for $\mu < \mu_c$ decreasing forcing results in the pulse length decreasing until the pulse is destroyed in a saddle-node bifurcation. Figure 3.3 shows both the analytical results for the steady state solutions of equation (3.15) and numerical results obtained by integrating the full amplitude equations (3.2-3.3). The pulse lengths were measured at half-amplitude. The pulse length is plotted as a function of forcing strength for several values of the control parameter μ confirming the expected behavior. The top figure is for group velocity $s = 20.0$ and the bottom figure for $s = 1.7$. Here we see that although the analytical result no longer agrees quantitatively for smaller s, it still describes the qualitative behavior of the pulse length as the control parameters are varied. This dependence on the group velocity will be discussed at the end of this section. Since the analysis leads to the single ordinary differential equation (3.15) describing the evolution of a pulse, the dynamics have been reduced to a one-dimensional manifold for the length of a pulse. A numerical control technique is then employed to obtain the unstable pulse solutions indicated by the long dashed curves in Figure 3.3. Given a specified pulse length, the technique adjusts the control parameter according to the direction of growth of the pulse length over a given time interval until the pulse length is no longer changing. In Figure 3.3, the parameter adjusted to control the length is the forcing strength ν. The same technique is also used for varying the control parameter μ while all other parameters remained fixed (cf. Figures 3.8-3.9).

These different regimes can be understood by looking at the individual interaction terms in equation (3.15) and their origins from equation (3.2). The first term in (3.15) is a measure of how far the control parameter μ is from the critical value μ_c where, in the absence of forcing, an isolated front is stationary. It provides a “pressure” which is directed outward for $\mu > \mu_c$ and which has to be balanced by the interaction terms. The second and third terms describe the interaction between fronts due to forcing. The second term arises from the linear coupling between A

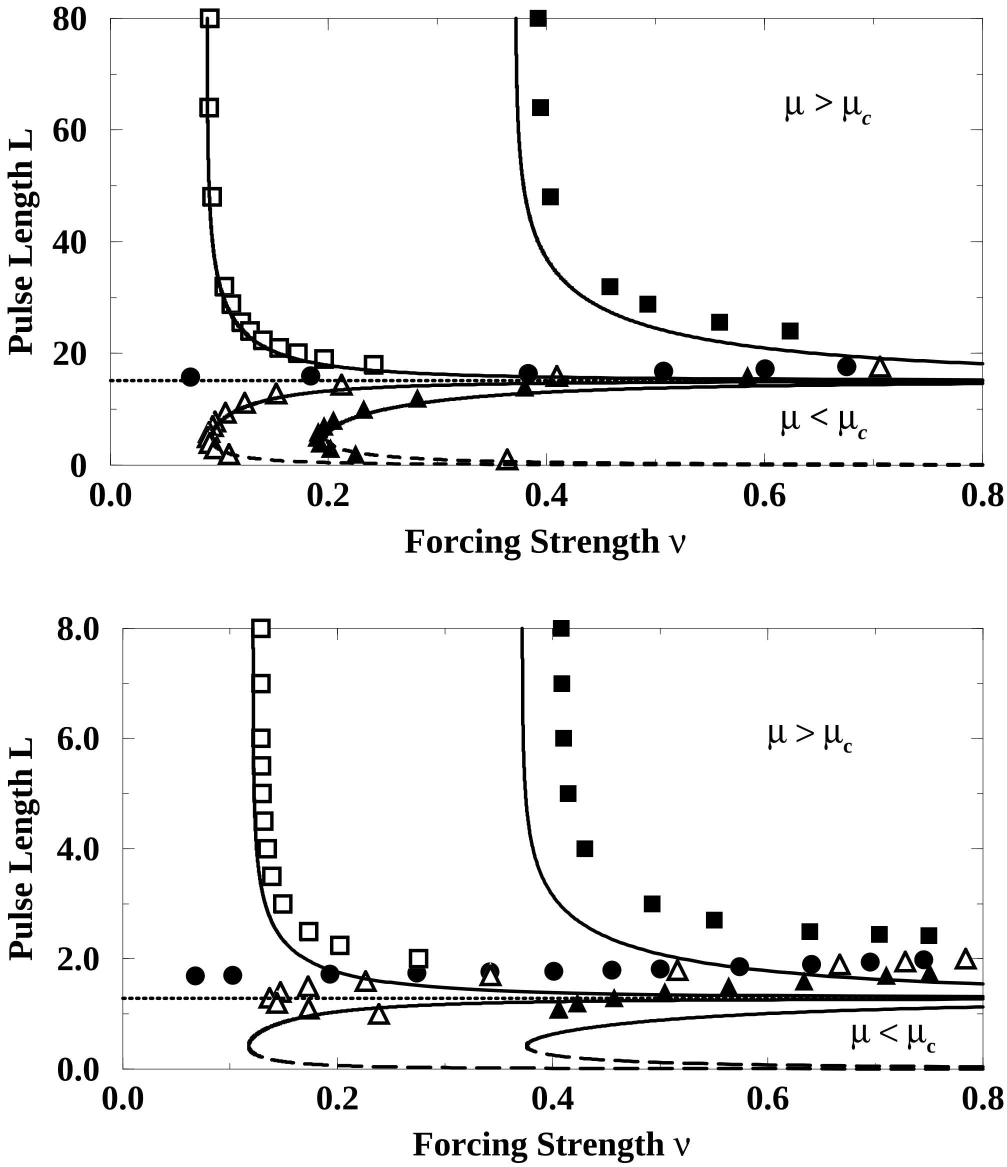

Figure 3.3: Dependence of pulse length L on the forcing strength ν. The symbols indicate the numerical results and the curves are obtained from equation (3.18). The dotted line corresponds to $\mu = \mu_c$. The curves above (below) this line correspond to values of $\mu > \mu_c$ ($\mu < \mu_c$). The dashed curves indicate unstable branches. The group velocity $s = 20$ and 1.7 in the top and bottom figures, respectively. $\mu = -1.238$ (solid squares), -1.2475 (open squares), $-1.248075 = \mu_c$ (circles), -1.2485 (open triangles), and -1.250 (solid triangles). All other parameters are as in Figure 3.4.

and B introduced by the forcing in equation (3.2) through which B excites A and therefore enhances the invasion of the nonlinear state into the linear state. The third term stems from the nonlinear coupling which, when $k_3 > 0$, suppresses A and therefore weakens the invasion.

The effect of forcing on a pulse depends on the distance between the fronts. Since the pulse is traveling to the right, the amplitude B is growing spatially to the left. For short pulses, therefore, B remains small and the linear coupling term dominates the interaction implying a repulsive interaction. Thus, for $\mu < \mu_c$ the inward "pressure" can be balanced by a repulsive interaction as it arises in short pulses. With increasing pulse lengths, B reaches larger values at the trailing front and the nonlinear coupling term gains importance leading, for large lengths, to an attractive interaction that grows with distance. In contrast to many other localization mechanisms, the growing attractive interaction present in long pulses is able to balance the outward "pressure" for $\mu > \mu_c$. In this regime the pulses become shorter with increased forcing. Figure 3.4 shows two pulse solutions obtained by numerically integrating equations (3.2-3.3). The control parameter μ is -1.240 for the longer pulse and -1.250 for the shorter pulse. All other parameters are the same for both pulses. Particularly note that the forcing $\nu = 0.2534$ for both pulses, yet the amplitude B (shown in the inset) has not saturated for the shorter pulse.

From equations (3.15-3.16) we see that when $dL/dT \equiv 0$ for a steady pulse L_0, then $dM/dT = k_1(\mu - \mu_c)/2$. Thus the pulse velocity in the moving frame is given by the invasion speed. By contrast, in dispersively stable pulses the velocity depends on the control parameter only through the nonlinear gradient terms [47,5]. Strikingly, in the asymptotic calculation leading to (3.16) the pulse velocity does not depend on the forcing ν. Figure 3.5a shows that the linear dependence on μ is in good agreement with this analytical result, but that the velocity does also depend on forcing ν. We suggest that the discrepancy may be explained by the contribution of the leading front at x_R to the interaction of the fronts. Since in this analysis $B_c = 0$ in region IV, this implies that forcing has no affect on the velocity of the leading front (equation 3.12). However, non-zero B within this inner region will slightly alter the

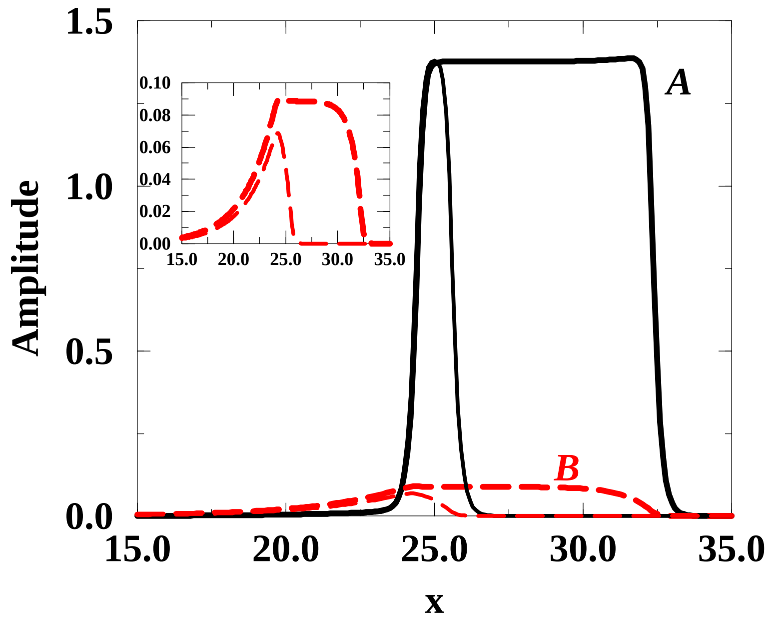

Figure 3.4: Numerically obtained long and short pulse solutions, with $\mu > \mu_c$ and $\mu < \mu_c$, respectively. The inset zooms in on the amplitude B only. The parameters are $\nu = 0.2534, s = 1.7, d = 0.05, c = 2.58, p = 1.0, g = 1.4, r = 4.0$, and $\mu = -1.244$ ($\mu = -1.250$) for the long (short) pulse. For these parameters $\mu_c = -1.248075$.

velocity of the leading front and consequently affect the pulse velocity and length as a function of forcing. For the parameters used in Figure 3.4, note that B varies slowly in region II whereas it varies almost as fast as A in region IV suggesting that the missing contribution is more prevalent at the leading front. Figure 3.5b shows single front velocities for both the leading and trailing front. The curves are the analytical results obtained from equation (3.12) for single fronts ($L \to \infty$) and the symbols indicate numerical results. As expected, the velocity of the trailing front is well described by the analysis, but the velocity of the leading front does depend slightly on forcing. This actual leading front velocity then dictates the velocity of the pulse. For larger group velocity s, the interaction length $2s/\alpha$ increases and the separation of the fast and slow spatial scales at the positions of the fronts becomes more distinct as shown in Figure 3.6. Thus we expect and the numerical results confirm (Figure 3.7) that the agreement with analytical results (3.15-3.16) for pulse

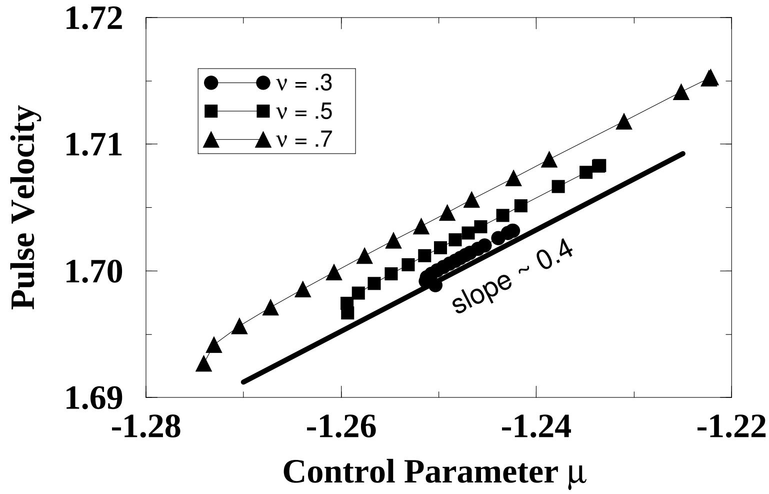

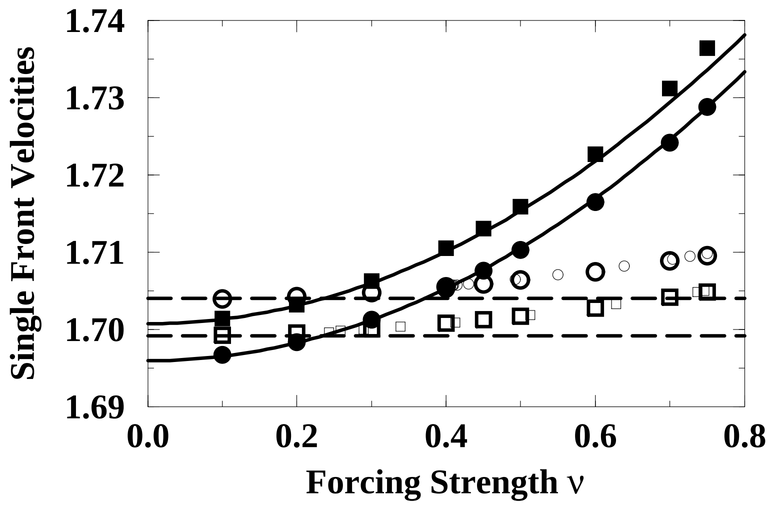

Figure 3.5: (a) Pulse velocity as a function of μ for forcing $\nu = 0.3, 0.5$, and 0.7. The line shown is obtained from the analytical result $v_{pulse} = k_1(\mu - \mu_c)/2 + s$. (b) Velocity dependence on forcing ν. The solid and open symbols indicate the numerically obtained velocities for the trailing and leading fronts, respectively. The curves give the analytical results. Squares are for $\mu = -1.250$ and circles for $\mu = -1.238$. The small symbols show the corresponding numerically obtained pulse velocities. All other parameters are as in Figure 3.4.

length and velocity improves with increasing group velocity s. For small forcing ν the relative error of the velocity is on order of the numerical accuracy. We note that the qualitative behavior of the pulse length is consistent even for smaller group velocity (Figure 3.3b).

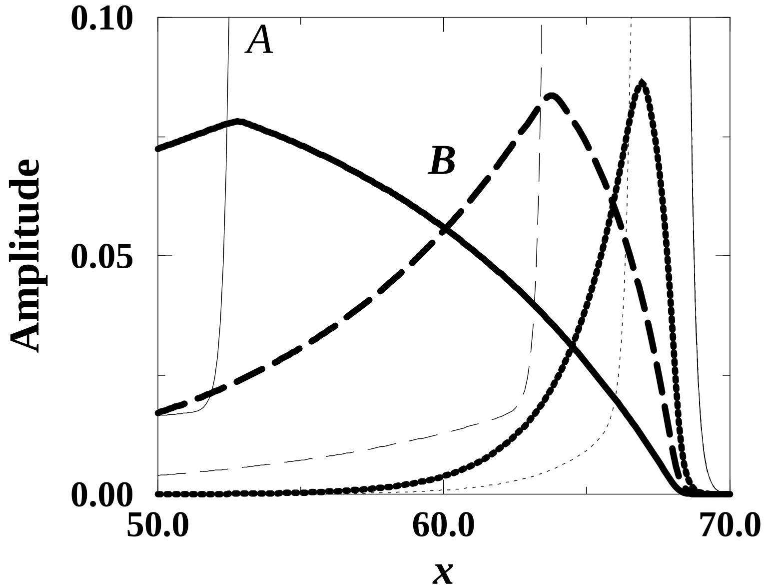

Figure 3.6: Amplitude B of pulse solutions when $s = 1.25, 5.0, 20.0$ indicated by the thick dotted, dashed, and solid lines, respectively. The amplitudes A are indicated by thin lines and the leading front in A is indistinguishable between the different velocities. $\mu = -1.2485, \nu = 0.29$ and all other parameters as in Figure 3.4.

However, since the interaction length $2s/\alpha$ scales with the group velocity, it approaches zero linearly with $s \to 0$. As the pulse length L reaches $\mathcal{O}(\epsilon)$, the overlap in the convective amplitude is no longer negligible. In this regime there exists a short unstable pulse corresponding to the unstable pulse which exists in the uncoupled real Ginzburg-Landau equation (1.5) (see Figure 1.3). It is therefore expected that the pulse stabilized by forcing will merge with this short unstable pulse as the group velocity s is decreased such that the pulse length is of $\mathcal{O}(\epsilon)$.

3.3 Holes and Multiple Pulses

The analysis from Section 3.1 can be applied to other front configurations such as hole states and multiple pulses. A hole consists of a localized region of

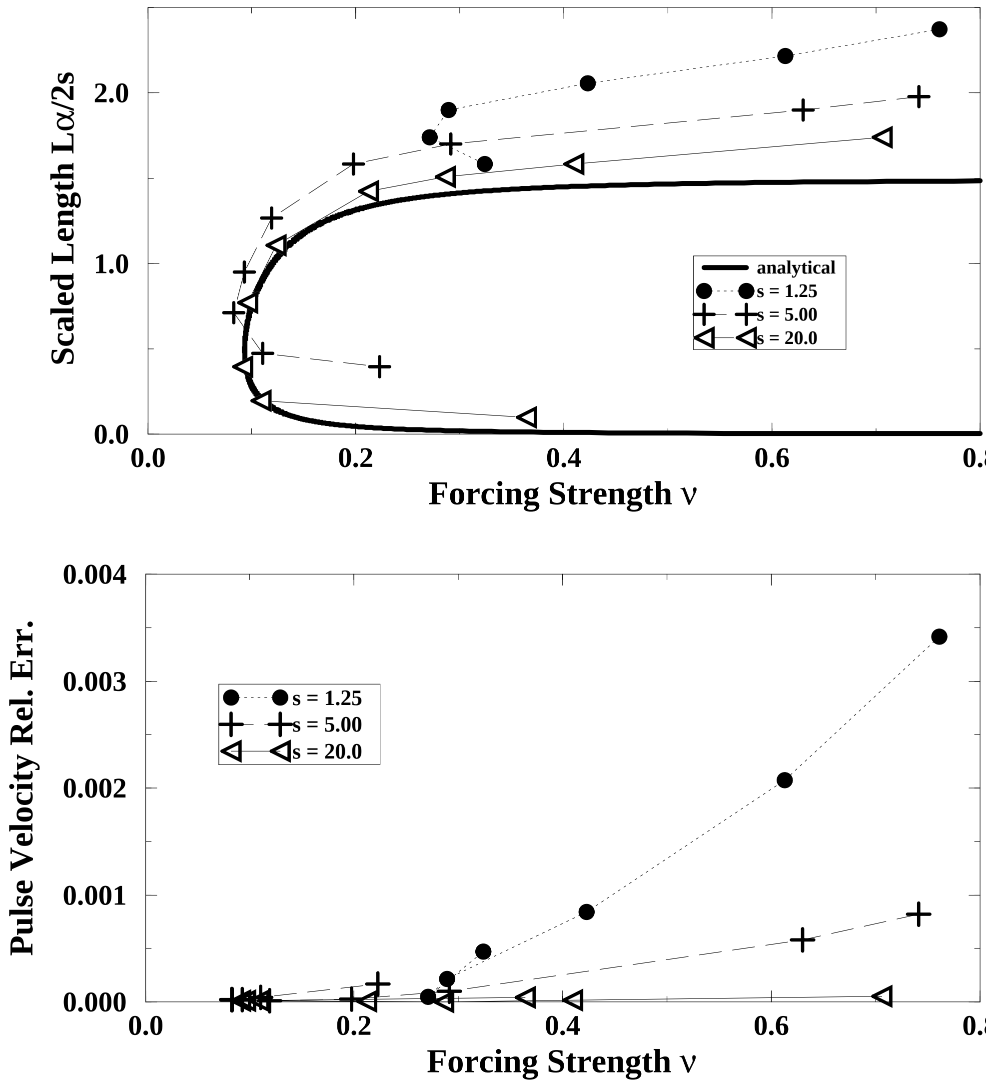

Figure 3.7: (a) Scaled pulse length and (b) relative error of pulse velocity versus forcing ν for $s = 1.25, 5.0, 20.0$. $\mu = -1.2485$ and all other parameters as in Figure 3.4.

zero amplitude in A surrounded by the nonzero traveling wave amplitude. The corresponding evolution equation for a hole of length L_h is given by

$$\frac{dL_h}{dT} = -k_1(\mu - \mu_c) - k_2\nu^2(1 + e^{\frac{\mu_c}{2s}L_h}) + k_3\nu^2(1 + e^{\frac{\mu_c}{s}L_h}), \tag{3.19}$$

where k_1, k_2, and k_3 are defined as before and a stable hole may be possible when $k_3 > 0$. Note that the interaction length for holes is now given by $-2s/\mu_c$ which is longer than the interaction length $2s/\alpha$ for pulses. Solving $dL_h/dT = 0$ again yields two possible solutions $L_h^{\pm}$, with the longer hole unstable and the shorter hole stable. In contrast with the pulses, stable holes thus exist only over a finite range of shorter lengths. The RHS is quadratic in $\Lambda_h = exp(\mu_c L_h/2s)$, describing a parabola opening upward. Although forcing variations now result in not only stretching the parabola, but also shifting it vertically, the variations in hole length again depends on the sign of the first term in (3.19). When $\mu < \mu_c$, increasing forcing causes stable holes to get shorter, while for $\mu > \mu_c$ the stable hole length will increase. Although the tendency of a hole to grow or shrink with increased forcing depends only on the sign of $\mu - \mu_c$, the limiting behavior is different depending on the relative sizes of k_2 and k_3. If $k_3 < k_2$ then holes exist only for $\mu < \mu_c$ and as ν increases, the hole length goes to zero. If $k_3 > k_2/2(\sqrt{2}-1) \approx 1.2k_2$, holes exist only for $\mu > \mu_c$ and as ν increases the stable hole length grows and eventually disappears in a saddle-node bifurcation with the unstable hole. Finally, for the intermediate values of k_3, holes exist for values of μ both above and below μ_c. In this case, as $\nu \to \infty$, the hole length approaches the limiting length determined when $\mu = \mu_c$.

Figure 3.8 shows a stable numerical hole solution and the control parameter μ as a function of the hole length for different values of the forcing. Stable and unstable solutions are indicated by solid and open symbols, respectively. Again, the unstable holes are obtained by means of a numerical control technique. First, we note that according to this analysis, the minimum of these curves should all be at the same value of L_h, but the numerical results show the minimum shifted to the right as ν increases. The analysis in Section 3.1 requires that A vanish in the hole region, but the presence of B in this region actually generates small nonzero A, which in turn generates B. Hence, the actual value of B at the trailing front is greater than predicted. This suppresses A there and the trailing front slows down leading to longer pulses and a shift of the minimum of the curves to the right as forcing ν increases. If the parameters are such that the control parameter μ can be taken smaller, the basic state is more strongly damped. Hence, within the hole region A is smaller and the shift of the curves is less pronounced as seen in Figure 3.9.

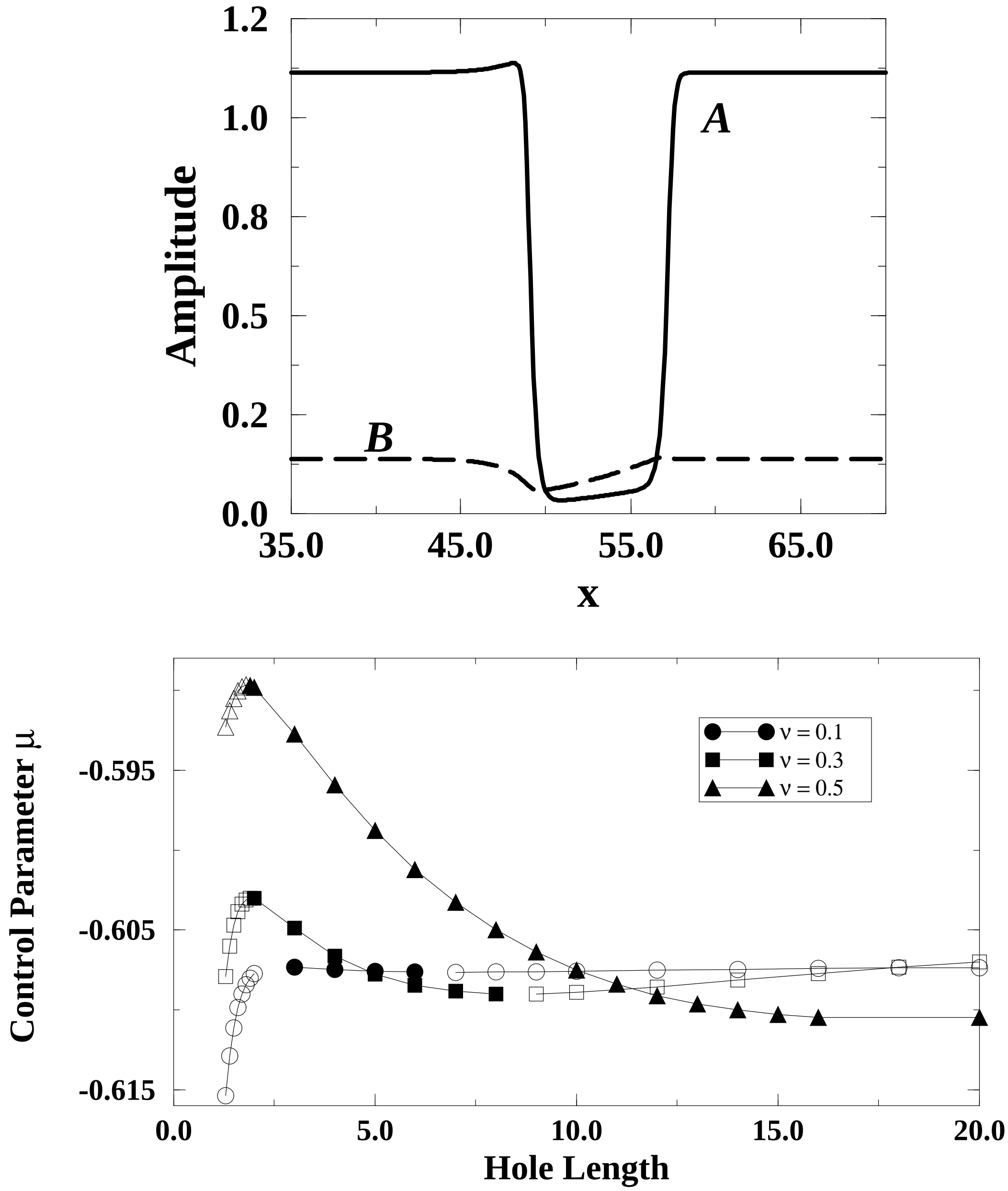

Figure 3.8: (a) Numerical hole solution for $c = 1.8, \mu = -0.609$, and $\nu = 0.3$. (b) Control parameter μ as a function of hole length for various values of ν. For $c = 1.8$, k_3 is in the regime where holes exist for both $\mu > \mu_c$ and $\mu < \mu_c$. Solid (open) symbols indicate stable (unstable) solutions. All other parameters are as in Figure 3.4 .

Here $c = 2.58$ so that $\mu_c \sim -1.248$ as compared to $c = 1.8$ in Figure 3.8 where $\mu_c \sim -0.608$.

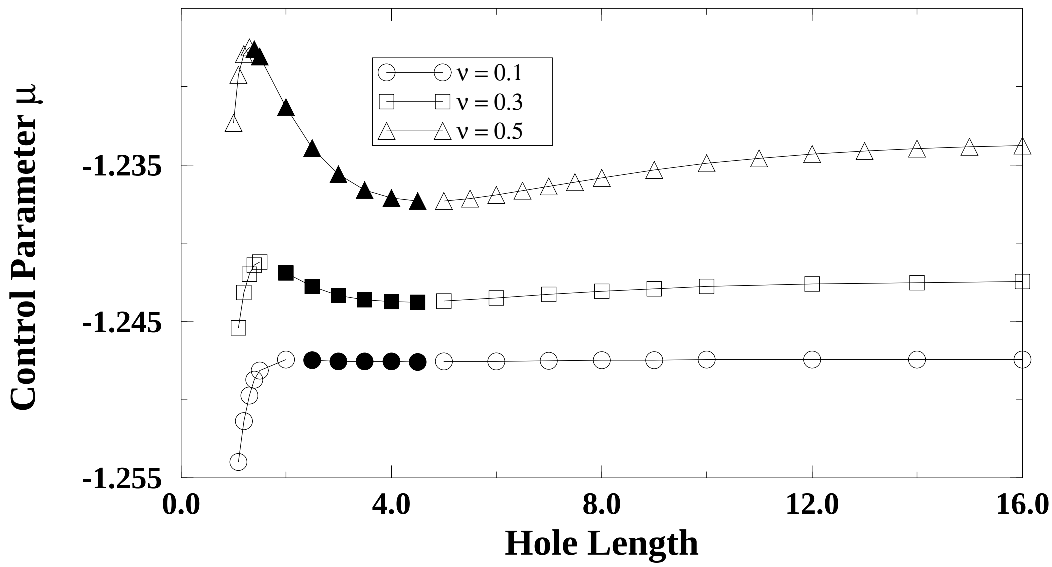

Figure 3.9: Control parameter μ as a function of hole length for various values of ν. For $c = 2.58$, k_3 is in the regime where stable holes exist only for $\mu > \mu_c$. Solid (open) symbols indicate stable (unstable) solutions. All other parameters are as in Figure 3.4 .

For a two pulse configuration, there are now four inner front regions which match to five outer regions resulting in evolution equations of the following form

$$\frac{dL_1}{dT} = k_1(\mu - \mu_c) + k_2\nu^2\Lambda_1 - k_3\nu^2\Lambda_1^2 \tag{3.20}$$

$$\frac{dL_2}{dT} = -k_1(\mu - \mu_c) - k_2\nu^2\Lambda_1(1 + \Lambda_2) + k_3\nu^2\Lambda_1^2(1 + \Lambda_2^2) \tag{3.21}$$

$$\begin{aligned}\frac{dL_3}{dT} &= k_1(\mu - \mu_c) + k_2\nu^2\left\{\Lambda_1\Lambda_2 + [1 + \Lambda_3(\Lambda_1\Lambda_2 - 1)]\right\} \\ &\quad -k_3\nu^2\left\{\Lambda_1^2\Lambda_2^2 + [1 + \Lambda_3(\Lambda_1\Lambda_2 - 1)]^2\right\}\end{aligned} \tag{3.22}$$

where L_1 is the length of the leading pulse, L_2 is the separation distance and L_3 is the length of the trailing pulse. Λ_i are defined in terms of L_i as follows: $\Lambda_1 = 1 - \exp(-\alpha L_1/2s), \Lambda_2 = \exp(\mu_c L_2/2s)$, and $\Lambda_3 = \exp(-\alpha L_3/2s)$. Since equation (3.20) for L_1 is the same as equation (3.15) which describes a single pulse, the leading pulse length is unaffected by the trailing pulse. But the trailing pulse length depends on both the length of the leading pulse and the separation distance and is shorter than the leading pulse. Solving equations (3.20-3.22) for the fixed points $\Lambda_{10}, \Lambda_{20}, \Lambda_{30}$, it is found that $\Lambda_{10} \cdot \Lambda_{20} = k_2/k_3$ and $\Lambda_{30} = k_3 \cdot (1 - \Lambda_{10}/(k_3 - k_2)$. Since L_1 increases with increasing Λ_1, and L_2 and L_3 increase with decreasing Λ_2 and Λ_3, this suggests that all three lengths will either increase or decrease as the control parameters μ and ν are varied. The eigenvalues σ_i obtained from linearizing equations (3.20-3.22) indicate that $\sigma_1 = \sigma_3$ and a two-pulse solution may be stable when k_3 is positive. A stable two-pulse solution is therefore expected to exist and be stable whenever a single pulse exists. However, since the trailing pulse is narrower than the leading pulse, it may become too short and collapse as it merges in a saddle-node bifurcation with the shorter unstable pulse for parameter values where the single pulse is still stable. Numerically, we observe that as the control parameter μ is decreased all three lengths get shorter and the trailing pulse eventually collapses to zero. Figure 3.10 shows a two-pulse solution superimposed over a single pulse solution confirming that the leading pulse length is unaffected by the trailing pulse.

Similarly, a periodic chain of pulses can be considered by constructing the pulse in a box of fixed length L_{box} with periodic boundary conditions. Referring to Figure 3.1, regions I and V are combined into one outer region of length $L_2 = L_{box} - L$ where L is the length of a pulse. The resulting evolution equation for the pulse length is

$$\begin{aligned} \frac{dL}{dT} &= k_1(\mu - \mu_c) + k_2\nu^2 \frac{(1 - e^{-\frac{\alpha}{2s}L})}{(1 - e^{\frac{\mu_c}{2s}L_2} e^{-\frac{\alpha}{2s}L})}(e^{\frac{\mu_c}{2s}L_2} + 1) \\ &\quad - k_3\nu^2 \frac{(1 - e^{-\frac{\alpha}{2s}L})^2}{(1 - e^{\frac{\mu_c}{2s}L_2} e^{-\frac{\alpha}{2s}L})^2}(e^{\frac{\mu_c}{s}L_2} + 1). \end{aligned} \tag{3.23}$$

Very short pulses are, as usual, unstable and quickly collapse. Similarly, pulses that nearly fill the system are also unstable and quickly fill the box. For intermediate lengths, periodic chains exist and are stable when constructed from a single pulse in box.

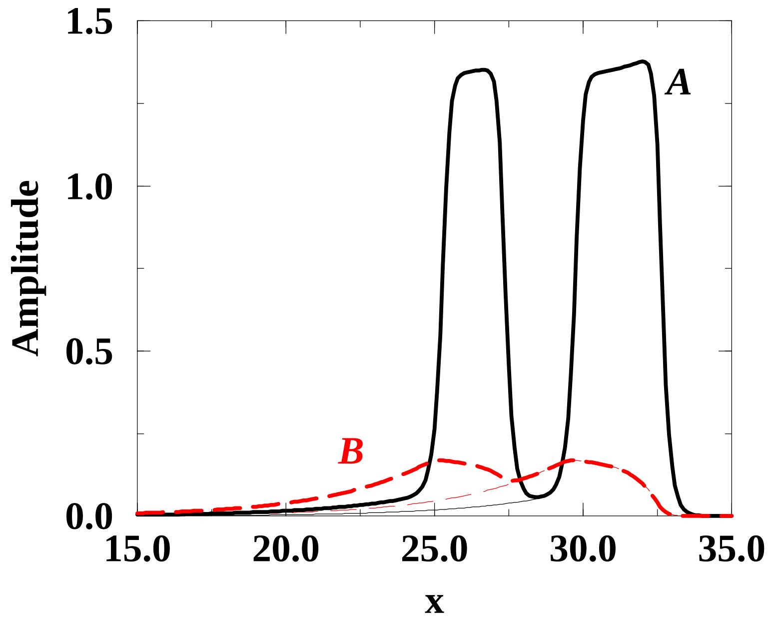

Figure 3.10: Two-pulse solution (thick lines) superimposed over a single-pulse solution (thin lines) for $\mu = -1.238, \nu = 0.5$, and all other parameters as in Figure 3.4.

3.4 Dispersion Effects

Waves generally have both linear and nonlinear dispersion. Hence, the coefficients and the amplitudes in equations (3.2-3.3) are in general complex. In order to understand the contribution of weak dispersion the derivation of equation (1.8) from [47, 5] is presented below for the single complex Ginzburg-Landau equation

$$\partial_t A = d\partial_x^2 A + \mu A + c|A|^2 A - p|A|^4 A. \tag{3.24}$$

If the imaginary parts of the coefficients are small (i.e. weak dispersion), then the front solution and its modified velocity can be calculated perturbatively. For a general traveling wave solution, the complex amplitude can be written as

$$A(x,t) = R(x,t)e^{i\phi(x,t)}, \tag{3.25}$$

where R and ϕ are the real amplitude and phase. Substituting this form into equation (3.24) results in the following equations for the amplitude R and the phase ϕ

$$\partial_t R \;=\; \mu R - d_r(R\phi_x^2 - R_{xx}) + d_i(-R\phi_{xx} - 2R_x\phi_x) + c_r R^3 - p_r R^5, \tag{3.26}$$

$$R\partial_t \phi \quad = \quad -d_i \left(R\phi_x^2 - R_{xx} \right) + d_r \left(R\phi_{xx} + 2R_x \phi_x \right) + c_i R^3 - p_i R^5, \tag{3.27}$$

where the subscripts 'r' and 'i' refer to the real and imaginary parts of the coefficients. The following expansions are introduced

$$R \quad = \quad A_0(\eta) + \epsilon^2 A_2(\eta) + \cdots, \tag{3.28}$$

$$\phi \quad = \quad \epsilon\omega_1 t + \int q(\eta) d\eta, \tag{3.29}$$

$$q(\eta) \quad = \quad \epsilon q_1(\eta) + \cdots \tag{3.30}$$

where $A_0(\eta)$ is the leading-order, real front solution given by equation (3.10), $\eta = x - x_L(T)$ or $x_R(T) - x$ for the left and right front, respectively with μ_c, A_c, and ξ defined as before. The scaling in ϵ in these expansions was chosen so that the analysis is manageable.

At $\mathcal{O}(\epsilon)$, the following equation is obtained from equation (3.27)

$$d_r \frac{d}{d\eta} \left[A_0^2 q_1 \right] = A_0^2 \omega_1 - d_i A_0'' A_0 - c_i A_0^4 + p_i A_0^6. \tag{3.31}$$

The wavenumber q_1 can then be calculated by integrating both sides. For this integral to remain bound as $\eta \to \infty$ requires that the frequency be given by

$$\omega_1 = c_i A_c^2 - p_i A_c^4. \tag{3.32}$$

The solution for $q_1(\eta)$ is then found to be

$$q_1(\eta) = \frac{1}{d_r} \left[U + V A_0^2 \right] \tag{3.33}$$

where

$$U \quad = \quad A_c^2 \xi \left[\frac{c_i}{2} - \frac{p_i A_c^2}{2} - \frac{d_i}{2\xi^2 A_c^2} \right] \tag{3.34}$$

$$V \quad = \quad \xi \left[\frac{3d_i}{4\xi^2 A_c^2} - \frac{p_i A_c^2}{4} \right]. \tag{3.35}$$

As $\eta \to \infty$, the wavenumber q_∞ is given as

$$q_\infty = \frac{A_c^2}{d_r} \xi \left[\frac{c_i}{2} + \frac{d_i}{4\xi^2 A_c^2} - \frac{3p_i A_c^2}{4} \right]. \tag{3.36}$$

Hence, a front connecting the traveling-wave state and the basic state determines the local wavenumber near the left front to be q_∞. Similarly, it will be $-q_\infty$ for a right front.

The $\mathcal{O}(\epsilon^2)$ equation obtained from equation (3.26) is

$$\mathcal{L}A_2 = \mp d_T x_{L,R} A_0' - \mu_2 A_0 + d_r A_0 q_1^2 + d_i A_0 q_1' + 2 d_i A_0' q_1 \tag{3.37}$$

where $\mathcal{L} = d_r \partial_\eta^2 + \mu_c + 3c_r A_0^2 - 5p_r A_0^4$ is the singular, linearized operator. Projecting equation (3.37) onto the zero-eigenmode $\partial_\eta A_0$ determines the velocity of a single, non-interacting front to be

$$\frac{dx_L}{dT} = -\frac{dx_R}{dT} = -2\xi(\mu - \hat{\mu}_c). \tag{3.38}$$

The value $\hat{\mu}_c$ is the value of the control parameter where a single front is stationary which includes a correction due to dispersive terms:

$$\hat{\mu}_c = \mu_c + \frac{1}{d_r}\left[U^2 + A_c^2 UV + \frac{1}{3}A_c^4 V^2\right] + \frac{d_i}{d_r \xi}\left[\frac{2}{3}A_c^2 V + U\right]. \tag{3.39}$$

Once again, a pulse solution is formed as a bound pair of these front solutions. If the distance $L = x_R - x_L$ between fronts is large, their shapes are only weakly distorted by the presence of the other front. Hence, the effect on the velocity and their resultant interaction is weak and can be determined as follows. The solutions are expanded similar to equations (3.30), but now the pulse solution is a composite of the left and right front solutions and their common amplitude. The local wavenumber and frequency determined previously in equations (3.32-3.33) are modified to account for the interaction, i.e.

$$R = A_L(x - x_L) + A_R(x_R - x) - A_c + \epsilon^2 A_2(\eta) + \cdots, \tag{3.40}$$

$$q(\eta) = \epsilon q_1(\eta) + \delta q(\eta) \tag{3.41}$$

$$\omega = \epsilon \omega_1 + \delta\omega. \tag{3.42}$$

To lowest order, $A_L = A_0(x - x_L), A_R = A_0(xR - x)$, and A_c (cf. equations (3.10)) each solve the amplitude equation. Let $x_m = (x_R + x_L)/2$ be the center of the localized pulse and consider the semi-infinite domains $x > x_m$ and $x < x_m$ separately. For $x < x_m$,

$$\begin{aligned} A_R - A_c &= A_c \left\{ \sqrt{\frac{1}{2}\left[1 + \tanh\left(\frac{\eta}{\xi}\right)\right]} - 1 \right\} && (3.43) \\ &= \frac{A_c e^{-(x_R - x)/\xi}}{\sqrt{e^{2(x - x_R)/\xi} + 1}\left(1 + \sqrt{1 + e^{-2(x_r - x)/\xi}}\right)} && (3.44) \\ &\approx -\frac{A_c}{2} e^{-2(x_R - x)/\xi} \ll 1 \text{ as } x_R - x \to \infty. && (3.45) \end{aligned}$$

A similar result is obtained for $A_L - A_c$ on $x > x_m$. The differences $A_{R,L} - A_c$ are taken to be the same order as A_2, i.e. $\sim \epsilon^2$. The correction to equation (3.31) due to dispersion on $(-\infty, x_m]$ leads to the following equation for $\delta q(\eta)$

$$A_0 \delta\omega = d_r A_0 \delta q' + 2 d_r A_0' \delta q, \tag{3.46}$$

which gives the solution

$$\begin{aligned} \delta q &= \frac{\delta\omega}{2 d_r}\left(1 + e^{-\frac{2(x - x_L)}{\xi}}\right) \ln\left(1 + e^{2\frac{x - x_L}{\xi}}\right) && (3.47) \\ &\approx \frac{\delta\omega}{d_r}(x - x_L) \text{ as } x - x_L \to \infty. && (3.48) \end{aligned}$$

A similar result is obtained for the right front on $[x_m, \infty)$ and the asymptotic values at the left and right fronts are given by $q \approx \pm(q_\infty + \delta q)$. Requiring this expression for the local wavenumber inside the pulse to match at the center of the pulse leads to the additional modification of the frequency to be $\delta\omega = -2 d_r q_\infty / L$.

In order to see how the interaction between the two fronts affects the velocity of a single front, these values and expansions are reinserted into the amplitude equation (3.26) for each semi-infinite domain, $x < x_m$ and $x > x_m$. For the left front this leads to a correction to equation (3.37) in which the following three terms appear on the right-hand side:

$$2 d_r A_0 q_1 \delta q - d_i A_0 \delta q' - 2 d_i A_0' \delta q \tag{3.49}$$

Each of these terms contains δq which gives an overall factor of k_∞ / L. Incorporating these terms into the solvability condition yields the following velocity due to dispersion of an interacting front

$$\frac{dx_L}{dT} = -\frac{dx_R}{dT} = -2\xi(\mu - \hat{\mu}_c) - \frac{k_5}{2L}. \tag{3.50}$$

The term proportional to k_5 represents the interaction due to dispersion since k_5 depends on the imaginary terms

$$k_5 = 8q_\infty \xi \left(\xi U \frac{\pi^2}{6} + \xi A_c^2 V - d_i \right), \tag{3.51}$$

where q_∞, U, V, ξ and A_c are all defined above.

The solvability condition arises from translation symmetry. In the case of a stationary, bound, two-front solution, the spatial derivative of this solution is the zero-eigenmode. However, as mentioned above, the cases $x < x_m$ and $x > x_m$ can be considered separately for large separation distance L. Hence, two solvability conditions arise, one in each domain. Technically the projection onto the zero-eigenmode $\partial_x A_{L,R}$ on the intervals $(-\infty, x_m]$ and $[x_m, \infty)$ will lead to boundary terms at x_m. However, these terms will be of higher order and can be neglected.

The final correction to the interacting front velocity can be obtained by considering the additional terms

$$-A_R'' - (\mu_c + 3c_r A_L^2 - 5p_r A_L^4)(A_R - A_c) + d_T x_R A_R' \tag{3.52}$$

appearing on the right-hand side of equation (3.37) for $x < x_m$ and $A_0 \to A_L$. Similar results are obtained for A_R and $x > x_m$. The resulting integrals from the solvability conditions are approximated using the asymptotic expression (3.45) and the leading order terms are retained. This interaction leads to an exponential term $\sim e^{-2L/\xi}$ in the front velocity.

Combining the results into a single equation describing the evolution of a pulse of length L yields the equation presented in the introduction Section 1.2.2 [47, 5]:

$$\frac{dL}{dt} = k_1(\mu - \hat{\mu}_c) - k_4 e^{-2L/\xi} + \frac{k_5}{L}. \tag{3.53}$$

The coefficients k_1 and k_4 are positive and contain only the real part of the original coefficients. The first term is similar to equation (3.15) where $\hat{\mu}_c$ is the new value of the control parameter at which a single, isolated front is stationary. The second term arises as a result of the overlap of the fronts in the convective amplitude. The term involving k_5 contains the imaginary parts of the coefficients, so that this term represents the interaction due to dispersion. When $k_5 > 0$, dispersion provides a repulsive interaction and can lead to the existence of stable pulses. When $\mu < \hat{\mu}_c$ two pulse solutions exist with the longer one being stable.

We are interested in the combined effects of forcing and dispersion, particularly whether periodic forcing can stabilize or destabilize pulses obtained in the purely dispersive regime. The task of deriving front equations including both dispersion and forcing seems formidable. It is suggested and validated by the numerical simulations below that the relevant aspects of both features may be modeled by adding the two contributions. This leads to an equation of the following form for pulses of length L:

$$\frac{dL}{dT} = k_1(\mu - \hat{\mu}_c) + k_2\nu^2(1 - e^{-\frac{\alpha}{2s}L}) - k_3\nu^2(1 - e^{-\frac{\alpha}{2s}L})^2 - k_4 e^{-L/\xi} + \frac{k_5}{L}. \qquad (3.54)$$

If both dispersion and forcing independently result in a stable pulse, their combined contribution merely enhances the stability of the pulse. The case of competing contributions is more interesting. Figure 3.11 is a plot of the control parameter μ as a function of steady-state pulse lengths L from equation (3.54). The dashed curve is for dispersion in the absence of forcing ($\nu = 0$), whereas the solid and dotted curves indicate the addition of forcing. For a given value of the control parameter indicated by the thin horizontal line, the equilibrium solutions can be determined, solid circles indicating stable solutions and open circles indicating the unstable solutions. Plotted are both cases when weak dispersion leads to a stable pulse, $k_5 > 0$ (a), and when it does not, $k_5 < 0$ (b). If forcing does not stabilize a pulse ($k_2/2k_3 > 1$), then increasing forcing pushes the stable branch of solutions downward. There is a competition between the two interactions and four solution branches may exist (Figure 3.11a inset). Eventually, for sufficiently large forcing ν the stable pulse disappears at infinity, leaving only the unstable pulse solution. Similarly, when dispersion does not stabilize the pulse, increasing forcing with $k_2/2k_3 < 1$ can eventually lead to a stable pulse branch (Figure 3.11b).

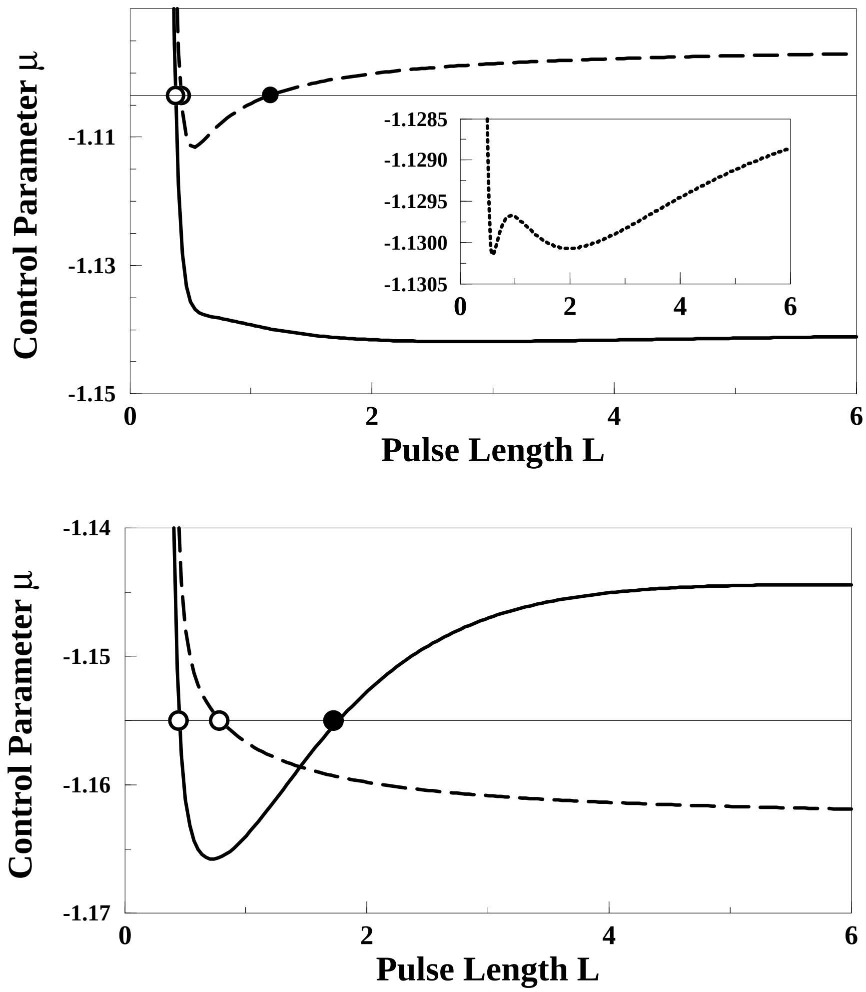

Figure 3.11: Control parameter μ vs. steady-state pulse lengths of equation (3.54) for dispersion only, $\nu = 0$ (dashed curve) and added forcing $\nu = 0.5$ (solid curve). The solid circles indicate stable solutions and the open circles indicate unstable ones for a given value of μ. (a) For $k_5 > 0$ and $k_2/2k_3 > 1$ forcing can eventually destroy a stable pulse, $d = 0.01 + 0.0i, r = 0.0$. The inset shows the four branches possible for an intermediate value of forcing $\nu = 0.425$. (b) For $k_5 < 0$ and $k_2/2k_3 < 1$ increased forcing can lead to stable pulse solutions, $d = 0.01 - 0.01i, r = 4.0$. All other parameters are the same: $s = 1.7, c = 2.45 + 0.2i, p = 1.0, g = 1.4$.

For large L, equation (3.54) is dominated by the $1/L$ dispersive interaction, suggesting that the original dispersive behavior is recovered for large lengths L. For a case like that shown in Figure 3.11a (inset), the competition can lead to two additional pulses, one unstable and one stable, for intermediate values of forcing ν. For larger forcing, only one unstable pulse and one long, stable pulse remain. Note that for fixed μ and increasing ν the stable pulse will still disappear at infinity since the branch is being pushed downward. So this continued existence of both branches occurs at a new, small range in the control parameter. For a case like that depicted in Figure 3.11b, in which the forcing generates a stable pulse, the $1/L$ behavior of the dispersive interaction suggests the existence of a long, third, unstable pulse. However, in the analysis of the dispersive interaction in [47] and confirmed numerically in [51], this power-law behavior continues only up to a maximal length L_{max}, beyond which the dispersive interaction decays rapidly. This maximal length L_{max} decreases with increasing dispersion. If forcing dominates the interaction for lengths up to L_{max}, then this long-length dispersively dominated behavior is no longer expected for either case depicted in Figure 3.11. But it should be present for weaker forcing or shorter interaction length.

Figures 3.12 show numerical results that confirm the expected pulse behavior based on equation (3.54). Plotted are the numerically obtained pulse lengths as a function of the control parameter μ. Figures 3.12a,b show that increased forcing may destroy a dispersively stable pulse. For forcing strength $\nu = 0.2$, the forcing is not sufficient to eliminate the stable pulse and both solution branches are still present. The inset shows an intermediate value of $\nu = 0.4$ where four solution branches exist and Figure 3.12b shows the pulse lengths for stronger forcing $\nu = 0.5$, where only the unstable branch remains. Figures 3.12c,d depict the creation of a stable pulse branch by increasing forcing strength. When $\nu = 0.1$ forcing leads to a stable branch, but for longer lengths the dispersion dominates and a third, unstable pulse exists. However, for $\nu = 0.2$ the forcing succeeds in dominating the interaction beyond L_{max} so that the branch remains stable.

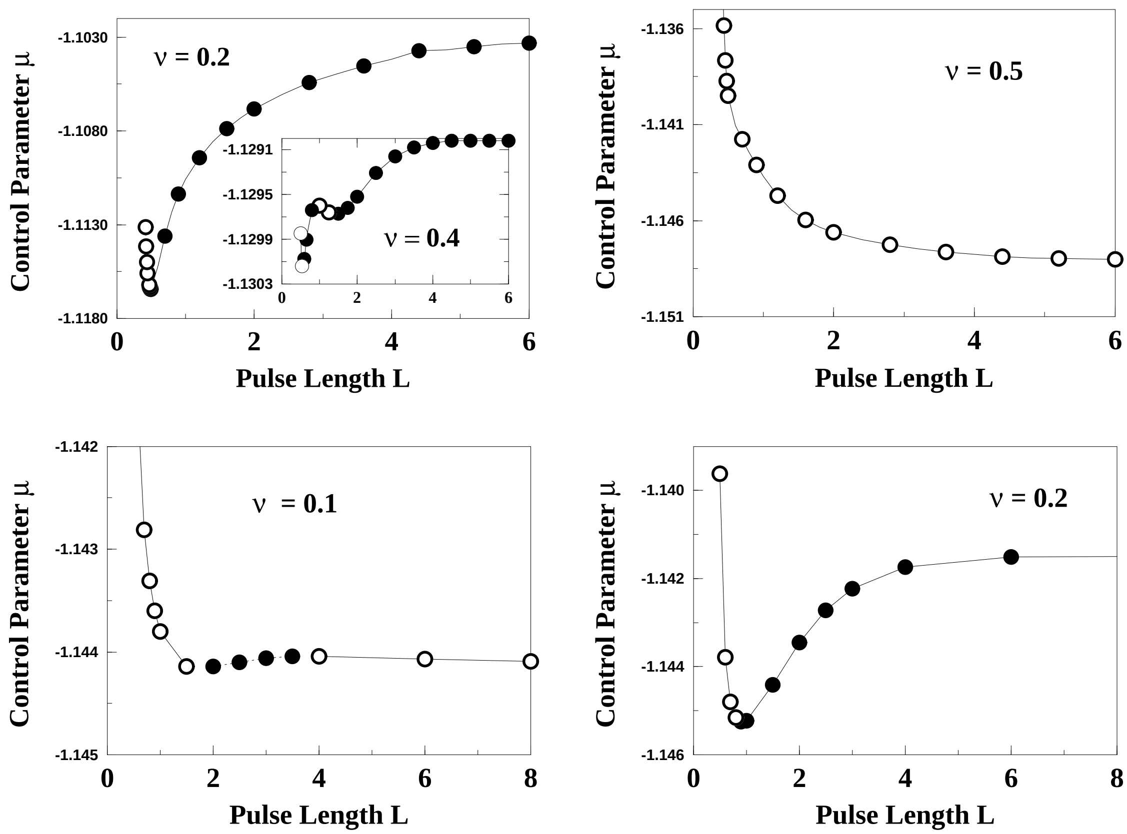

Figure 3.12: (a)-(b) The control parameter μ vs. the pulse length when forcing destroys a dispersively stable pulse ($d = 0.01 + 0.0i$ and $r = 0.0$). Forcing strength $\nu = 0.2$ and $\nu = 0.4$ (inset) in (a), and $\nu = 0.5$ in (b). (c)-(d) Forcing creates a stable branch ($d = 0.01 - 0.005i$ and $r = 4.0$). Forcing strength $\nu = 0.1$ in (c) $\nu = 0.2$ in (d). All other parameters are the same: $s = 1.7, c = 2.45 + 0.2i, p = 1.0, g = 1.4$.

3.5 Advected Mode

As discussed in the introduction, the localization of pulses in binary-mixture convection is also due to a slowly decaying concentration mode that is advected by the convective amplitude. Inclusion of this mode with the periodically forced waves leads to equations

$$\begin{aligned} \partial_t A &= -s\partial_x A + d\partial_{xx} A + (\mu + fC)A + c|A|^2 A - p|A|^4 A \\ &\quad -g|B|^2 A - r|A|^2|B|^2 A - u|B|^4 A + \nu B^*, \end{aligned} \tag{3.55}$$

$$\begin{aligned}
\partial_t B &= +s\partial_x B + d\partial_{xx} B + (\mu + fC)B + c|B|^2 - p|B|^4 B \\
&\quad -g|A|^2 B - r|A|^2|B|^2 B - u|A|^4 B + \nu A^*, \qquad (3.56)\\
\partial_t C &= \delta\partial_x^2 C - \alpha C + h\partial_x(|A|^2 - |B|^2). \qquad (3.57)
\end{aligned}$$

Similar to equations (1.9-1.10) and equations (3.2-3.3), additional coupling and nonlinear gradient terms have been omitted. If waves in only one direction are considered, the pulse length in the absence of forcing is governed by the following equations [50]

$$\begin{aligned}
v_l &= s - \frac{\gamma}{|v_l|} + \mathrm{sgn}(v_l)\rho, \qquad (3.58)\\
v_t &= s - \frac{\gamma}{|v_t|} - \mathrm{sgn}(v_t)\rho + 2\gamma\frac{e^{-\alpha L/v_l}}{|v_l|}, \qquad (3.59)\\
\frac{dL}{dT} &= \gamma\left(\frac{1}{v_t} - \frac{1}{v_l}\right) - 2\frac{\gamma}{v_l}e^{-\alpha L/|v_l|} + 2\rho, \qquad (3.60)
\end{aligned}$$

where v_l and v_t give the velocities of the leading and trailing fronts, respectively, and $dL/dT = \mathrm{sgn}(v_l)(v_l - v_t)$. The coefficient ρ scales with the control parameter μ and γ scales with the coupling h. These equations were also derived in the limit of weak diffusion ($d \ll 1$) so that the overlap in the traveling-wave amplitude has been ignored. It was shown that pulses arising from equations (3.58-3.60) are stable if they travel opposite the group velocity s.

Again, it is of interest to investigate the combined effects of periodic forcing and the concentration mode C on localized structures. When the group velocity is small the interaction length $2s/\alpha$ due to forcing decreases. Hence for the longer pulses localized by the concentration field, forcing no longer contributes significantly to the interaction of fronts directly. However, the velocity of each front is affected by forcing which, in turn affects the interaction via the advected mode C. For the left front, it may be expected from equation (3.13) that the contribution to the velocity is approximately $\nu^2(k_3 - k_2)$. Although equation (3.14) implies the right front is unaffected by forcing, the numerical results and discussion of section 3.2 suggest that the missing contribution to the velocity of the leading front is proportional to ν^2 and becomes more relevant for small group velocity. Since forcing does not contribute directly to the *interaction* of fronts, the pulse existence and stability should be determined by equations similar to equations (3.58-3.60) with a small correction to the velocities due to forcing. In particular, it is still expected that these pulses will be stable if they travel opposite the group velocity.

Starting with a stable pulse in the absence of forcing, we see that the pulses continue to travel backwards as forcing is added. Typically forcing leads to pulses that travel faster and become longer as in Figure 3.13. At this fixed value of μ, the pulse lengths are observed to diverge to infinity before forcing ν is sufficiently large for the amplitude B to grow to the full amplitude of A. Here it seems that the small coupling h which leads to less accumulation of the advected mode C and the associated feedback to the growth rate is not large enough to excite B to full amplitude. As μ decreases forcing may be increased further before the pulse length diverges. In the case shown in Figure 3.14 two regimes were observed. For $r = 0.0$, the pulses again traveled faster and the lengths grew. For the other parameter regime where $r = 4.0$ it was found that the pulse length decreased slightly and the pulses slowed down. In both cases the pulses continued to travel backwards and remained stable until forcing is sufficiently large that the amplitude B grows to full amplitude of A. Here the pulses lose stability to a standing-wave pulse similar to Figure 3.15b. In this case the coupling h and therefore C is larger leading to greater feedback to the local growth rate of both A and B. It is noted that in all cases observed the pulse lengths consistently decrease monotonically as a function of velocity.

In [48], pulses localized by the concentration field in the absence of forcing were observed to slow down and become shorter as the group velocity s was increased. Eventually the short pulses were destroyed in a saddle-node bifurcation which occurred for $s \sim \mathcal{O}(1)$ and before the velocity of the pulse reached zero. Since the pulses are stable when they travel opposite the group velocity, the advection of C must be sufficiently strong for larger group velocity so that the suppression of the local growth rate ahead of the pulse is large enough to cause the pulses to drift backwards. The necessarily strong coupling of A and B with C then enhances the

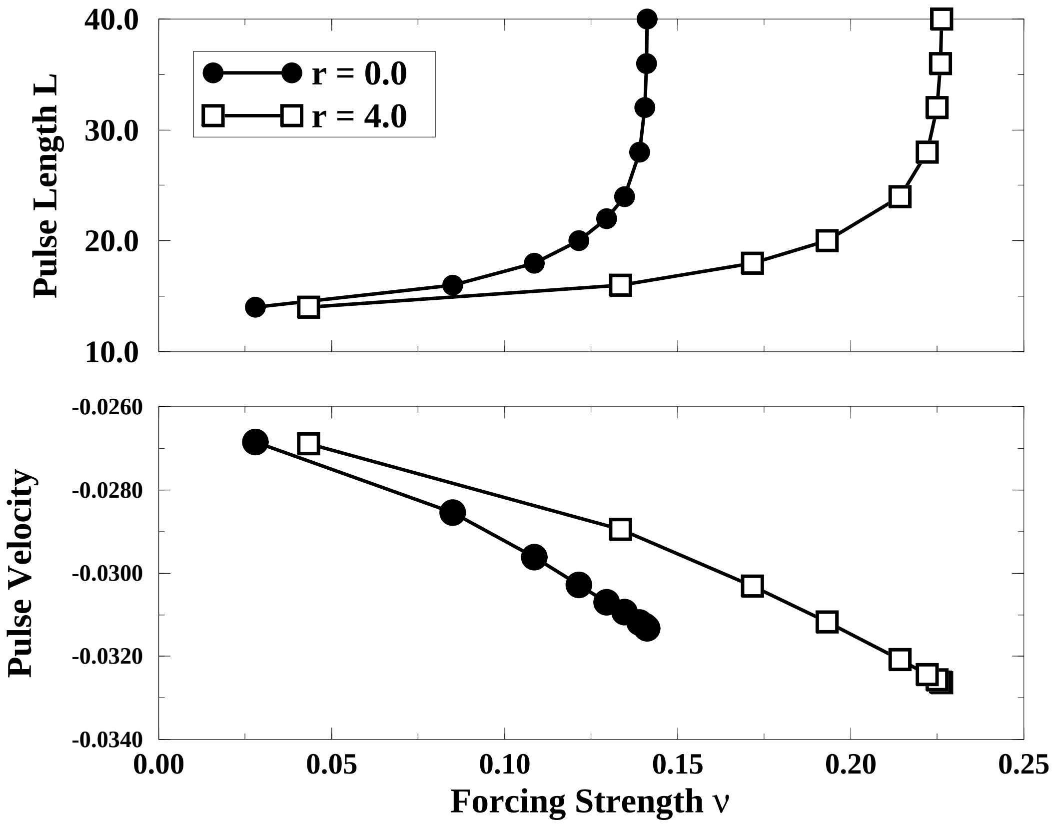

Figure 3.13: (a) Pulse length and (b) velocity as a function of forcing. (c) Pulse length vs. velocity. Parameters are $\mu = -1.0, s = 0.3, d = 0.05, c = 2.58, p = 1.0, g = 1.42, f = 1.0, \delta = 0.10, \alpha = -0.01, h = 0.03$.

local growth rate of both A and B at the right front as seen in Figure 3.15a. As forcing strength increases above a threshold, the amplitude of B grows to full amplitude of A and the solution typically tends to a standing-wave localized solution as shown in Figure 3.15b.

Figure 3.16 is a linear-log plot of this threshold value ν_{max} as a function of the group velocity s. The behavior is similar in both cases where in the absence of the concentration mode C the pulses would be stable ($r = 4.0$) and unstable ($r = 0.0$). For smaller group velocity, B decays more quickly to the left of the pulse. Therefore, forcing can be increased further and the threshold value ν_{max} is larger.

For larger group velocity, B decays more slowly to the left of the pulse

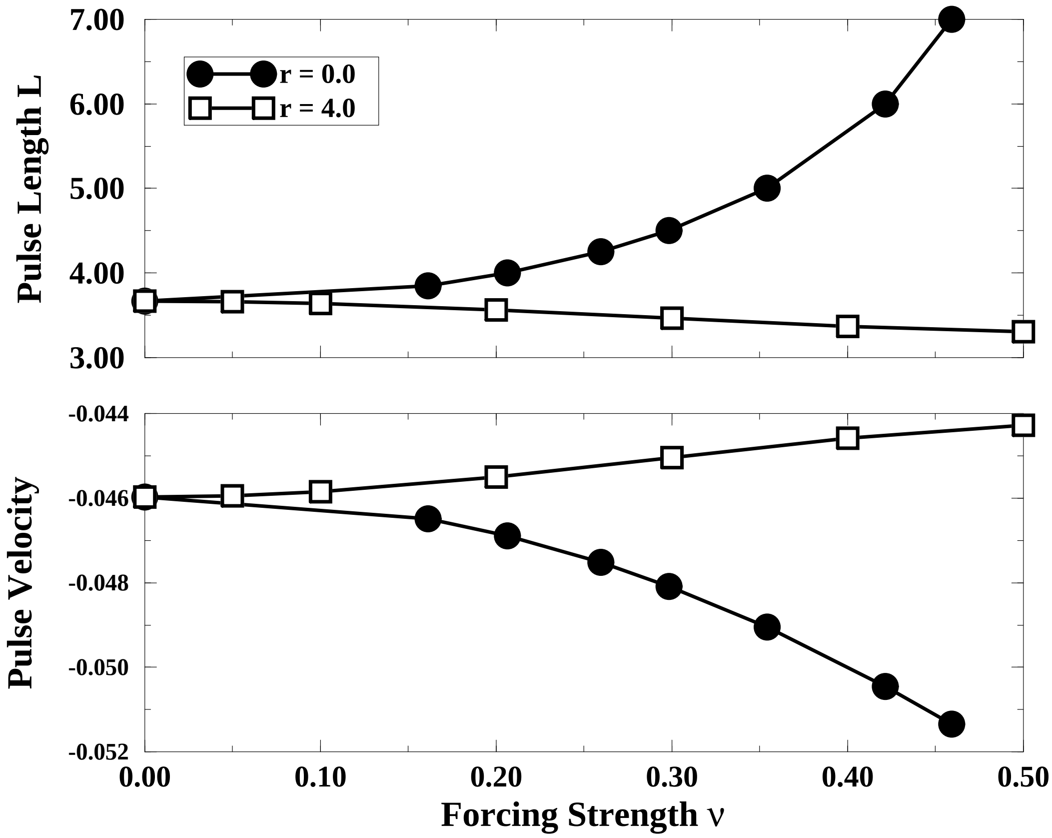

Figure 3.14: (a) Pulse length and (b) velocity as a function of forcing. (c) Pulse length vs. velocity. Parameters are $\mu = -1.0, s = 0.1, d = 0.01, c = 2.45, p = 1.0, g = 1.55, f = 0.1, \delta = 0.01, \alpha = -0.02, h = 0.3$.

where the concentration field further enhances the local growth rate. Hence B grows to full amplitude of A for relatively small values of ν. If the incremental increase of ν above threshold is small enough, the traveling-wave pulse becomes a standing-wave pulse similar to Figure 3.15b. However, if ν is incremented to a larger value, the left front is a fast front as described in [50] and seen in Figure 3.17. Here the build-up of C is not sufficient to slow down this front and the pulse length grows rapidly in this direction. The right edge of the pulse remains relatively motionless. Because of periodic boundary conditions the left front eventually wraps around and feels the right edge of the pulse. Rather than merging to fill the whole system, the strong presence of the concentration field at the right edge causes this fast front

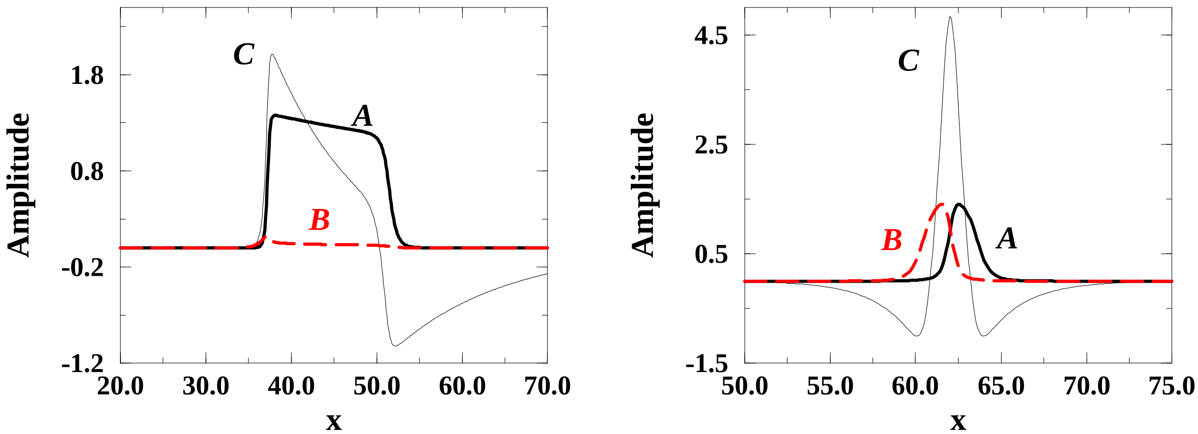

Figure 3.15: (a) Localized traveling-wave solution for forcing strength $\nu = 0.05$. (b) Localized standing-wave solution forcing strength $\nu = 0.10$. In both figures $r = 4.0, s = 0.4$, and all other parameters as in Figure 3.16.

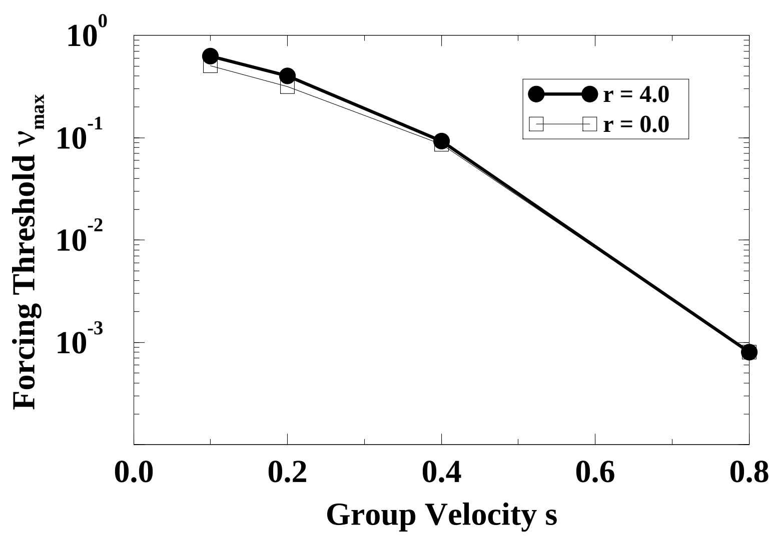

Figure 3.16: Threshold value of forcing strength ν above which the amplitude B grows to equal amplitude as A as a function of group velocity. The results are similar for both $r = 4.0$ (circles) and $r = 0.0$ (squares) where pulses in the absence of the advected mode C are stable and unstable, respectively. The other parameters are $\mu = -0.5427, d = 0.15, c = 2.4, p = 1.65, g = 1.42, f = 1.0, \delta = 0.10, \alpha = -0.02$, and $h = 0.3$.

to change its direction of propagation and it is eventually pushed back to form a standing-wave type localized structure similar to Figure 3.15b. Similarly if another pulse were in the path of the fast-traveling front it would also cause the fast front to change direction and form a standing-wave pulse.

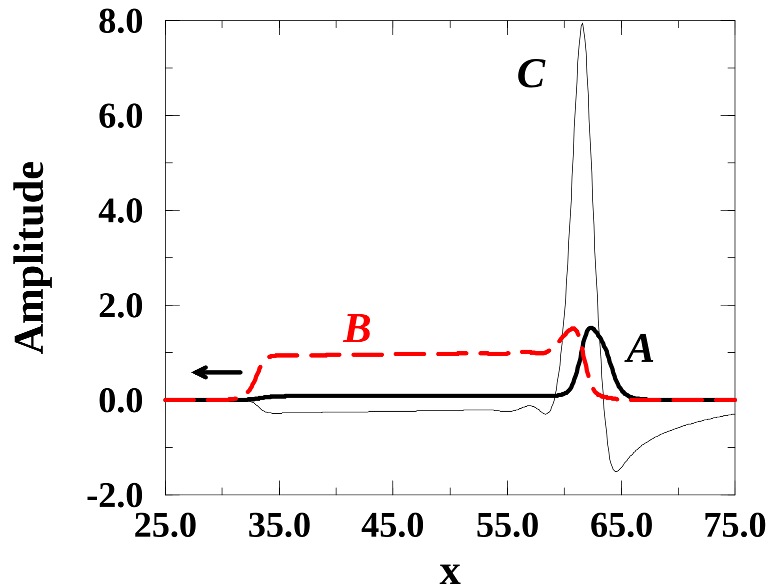

Figure 3.17: Growing pulse when forcing strength is incremented from $\nu = 0.0$ to $\nu = 0.20$ for $s = 1.0$. All other parameters as in Figure 3.16. Due to periodic boundary conditions, the left front eventually feels the presence of the right front and then begins to travel back to the right. The final state is a standing-wave pulse similar to Figure 3.15b.

3.6 Conclusions

In this chapter the effect of external periodic forcing on the interaction of fronts connecting the stable basic and nonlinear traveling wave states in a subcritical bifurcation has been investigated. Localized structures were described analytically as bound pairs of fronts. The temporal forcing excites the oppositely traveling wave and provides an additional mode which is sufficient to localize structures. Since forcing is an externally controlled parameter, pulses of tunable length can be obtained via this new localization mechanism. Forcing stabilizes pulses through either a repulsive or an *attractive* interaction between the fronts depending on the pulse length. This is in contrast to other localization mechanisms in which stable pulses arise only for a repulsive interaction [47,5,50]. Multiple pulses with different, but fixed, lengths and holes are also obtained.

In addition, the combined effect of temporal forcing and other localization mechanisms has been investigated. With the inclusion of weak dispersion, the interaction between fronts can be described by a single equation combining the two interaction terms (3.54). It was found that in this dispersive regime forcing can also lead to the creation of new pulses or the destruction of pulses depending on system parameters. The competition between the two interactions determine the number and stability of pulses observed.

Periodically forcing the extended Ginzburg-Landau equations (3.55-3.57) which couple the traveling wave amplitudes to a slowly decaying mode have been more difficult to analyze. First, it was found that the group velocity must be sufficiently small, otherwise B will grow to full amplitude for extremely small values of forcing strength ν. In this case the forcing creates standing-wave type pulses. For small group velocity s, forcing led to both increased and decreased pulse velocities which in turn caused the pulse length to decrease monotonically with increased pulse velocity. In some cases with weak coupling h, the stable pulse lengths diverged to infinity before forcing was sufficient to excite B to the full amplitude of A.

Chapter 4

Summary and Discussion

In summary of the work presented thus far in this thesis, localized structures have been investigated numerically and analytically within two general frameworks. First, oscillons were investigated within a modified Swift-Hohenberg model which retains both the fast and slow spatial scales. The interaction between these two scales leads to pinning of fronts and the localization of oscillon-type structures in two-dimensions is associated with an underlying square pattern. Localization is sustained as long as the bifurcation is sufficiently subcritical and the basic state is strongly stable. As the control parameter is increased above the stability limit for oscillons, the numerical results show strong similarities to the two types of transitions observed in the experimental system. Bound states of oscillon-structures were also found numerically. Prior to this work, oscillons of like polarity had not been observed experimentally, but were found in the numerical simulations of our model. Further investigation showed that these bound states of like polarity are less robust and very susceptible to noise which may be why they are not seen in the granular experiments. However, our model and the pinning of fronts suggested that such states could be observable under proper conditions. By studying a general model and obtaining oscillon-structures quite generally, it was expected that oscillons and their bound states could be observed in other systems where the transition to squares is sufficiently hysteretic. This prediction was supported by experiments on vertically vibrated colloidal suspensions. The existence range of these experimental oscillons scaled consistent with the nonadiabatic locking mechanism and they also observed bound states of oscillons of like polarity.

Secondly, one-dimensional localized traveling waves were studied within the framework of Ginzburg-Landau equations subject to external periodic forcing. The forcing itself provides a new localization mechanism which can be controlled externally, leading to pulses of tunable size. Periodic forcing can result in both an attractive and a repulsive interaction between the fronts. In contrast to other localization mechanisms which provide only a repulsive interaction between fronts to balance the inward "pressure", the periodic forcing allows balancing with either an inward "pressure" for short pulses or an outward "pressure" for longer pulses. Since forcing strength is an externally controlled parameter, one aim of this research is to gain insight into the response of localized structures to periodic forcing. The results may then be used to help determine the relevance of other localization mechanisms and to possibly control, suppress, or excite localized states. The combined effects of periodic forcing and weak dispersion were also investigated and it was found that forcing can destroy pulses that are stabilized by dispersion or create a new stable branch of solutions depending on the parameter regime. The effect of forcing structures localized by coupling to an advected mode was also investigated numerically. Although it was found that periodic forcing led to both increases and decreases in pulse velocity, the pulse length decreased monotonically with increased pulse velocity. For forcing sufficient to excite the amplitude B to full amplitude of A, the pulses often tended to standing-wave type pulses. In some cases the pulse length diverged before forcing was sufficiently strong to excite the full amplitude B.

The discussion below presents some of the open questions and continuing investigation related to the work involving periodically forced localized waves. First, the possibility of finding localized chaotic states is investigated in Section 4.1. Section 4.2 is a discussion of the relevance of the results of Section 3.5 to the two-dimensional worms observed experimentally in nematic liquid crystals. The effect of periodic forcing on a transverse cross-section as well as a two-dimensional worm state is presented.

4.1 Chaotic States

One question of interest is whether chaotic states may be localized by periodic forcing. Within the supercritical complex Ginzburg-Landau equation ($c < 0, p = 0$ in equation (1.7)), the Newell criterion $-d_i c_i - d_r c_r < 0$ signals the onset of phase chaos where plane-wave solutions are all Benjamin-Feir unstable. In [74] the equivalent criterion for the subcritical complex Ginzburg-Landau equation (1.7) was found to be

$$d_i(-c_i + 2p_i|A_0|^2) + d_r(-c_r + 2p_r|A_0|^2) < 0 \tag{4.1}$$

where A_0 is the amplitude of the spatially homogeneous solution $A_h = A_0 e^{i\omega t}$. It is within this Benjamin-Feir unstable regime that localized solutions were studied. For the parameters investigated, the imaginary terms must be taken relatively large with respect to the real parts of the coefficients and the solutions are dominated by the strongly dispersive behavior. The Benjamin-Feir instability is associated with dispersive forces which try to focus wavetrains into pulses [74]. Hence, it is difficult to find a localized chaotic state in this regime. It was found that for a range in the control parameter, the solutions tended to narrow, highly localized objects which did not exhibit chaotic behavior. As the control parameter μ is increased, these pulses expand to fill the system. This extended state again exhibits the chaotic behavior associated with the Benjamin-Feir instability. In the cases studied, the presence of periodic forcing does not seem to have a noticeable effect on the rate of expansion.

By changing the sign of one of the dispersive terms, the Ginzburg-Landau equation is in the defocusing parameter regime. The dispersive forces are no longer trying to focus wavetrains into localized objects. Additionally the system is no longer Benjamin-Feir unstable and thus far chaotic dynamics have not been observed in this regime.

4.2 Two-Dimensional Localized Worms

In light of the two-dimensional localized traveling waves or 'worms' observed in electroconvection of nematic liquid crystals, the relevance of the results of chapter 3 will be discussed. The introduction of periodic forcing excites both the zig and the zag waves traveling in the opposite direction which modifies the extended complex Ginzburg-Landau equations (1.11-1.13) introduced in Section 1.2.3 to be

$$\begin{aligned}
\partial_t A + \underline{\mathbf{u}}_A \cdot \nabla A &= \mu A + d_x \partial_x^2 A + d_y \partial_y^2 A + 2a\partial_{xy}^2 A + fCA \\
&\quad -(c|A|^2 + g|B|^2 + r|D|^2 + u|E|^2)A + kBD^*E + \nu D^* \qquad (4.2)
\end{aligned}$$

$$\begin{aligned}
\partial_t B + \underline{\mathbf{u}}_B \cdot \nabla B &= \mu B + d_x \partial_x^2 B + d_y \partial_y^2 B - 2a\partial_{xy}^2 B + fCB \\
&\quad -(c|B|^2 + g|A|^2 + r|E|^2 + u|D|^2)A + kAE^*D + \nu E^* \qquad (4.3)
\end{aligned}$$

$$\begin{aligned}
\partial_t D + \underline{\mathbf{u}}_D \cdot \nabla D &= \mu D + d_x \partial_x^2 D + d_y \partial_y^2 D + 2a\partial_{xy}^2 D + fCD \\
&\quad -(c|D|^2 + g|E|^2 + r|A|^2 + u|B|^2)A + kEA^*B + \nu A^* \qquad (4.4)
\end{aligned}$$

$$\begin{aligned}
\partial_t E + \underline{\mathbf{u}}_E \cdot \nabla E &= \mu E + d_x \partial_x^2 E + d_y \partial_y^2 E - 2a\partial_{xy}^2 E + fCE \\
&\quad -(c|E|^2 + g|D|^2 + r|B|^2 + u|A|^2)A + kDB^*A + \nu B^* \qquad (4.5)
\end{aligned}$$

$$\begin{aligned}
\partial_t C &= \delta \Delta C - \alpha C \\
&\quad + \nabla \cdot (\underline{\mathbf{h}}_A |A|^2 + \underline{\mathbf{h}}_B |B|^2 + \underline{\mathbf{h}}_D |D|^2 + \underline{\mathbf{h}}_E |E|^2). \qquad (4.6)
\end{aligned}$$

Recall that extended traveling-wave convection occurs in supercritical bifurcation and worms appear already below onset. Thus, there does not exist a bistability in which to form fronts between *extended* traveling waves and the basic state. However, in a reduction in the y-direction of the extended complex Ginzburg-Landau equations (1.11-1.13) localized standing wave structures, similar to those shown in Figure 3.15, were found to exist below onset of extended waves [58]. Hence, there does exist a bistability between this localized object and the basic state. A cross-section through the x-direction of a worm can be considered as bound fronts connecting these two states as depicted in Figure 4.1. This picture suggests that the results of Section 3.5 may indicate the response to periodic forcing along the length of the worm.

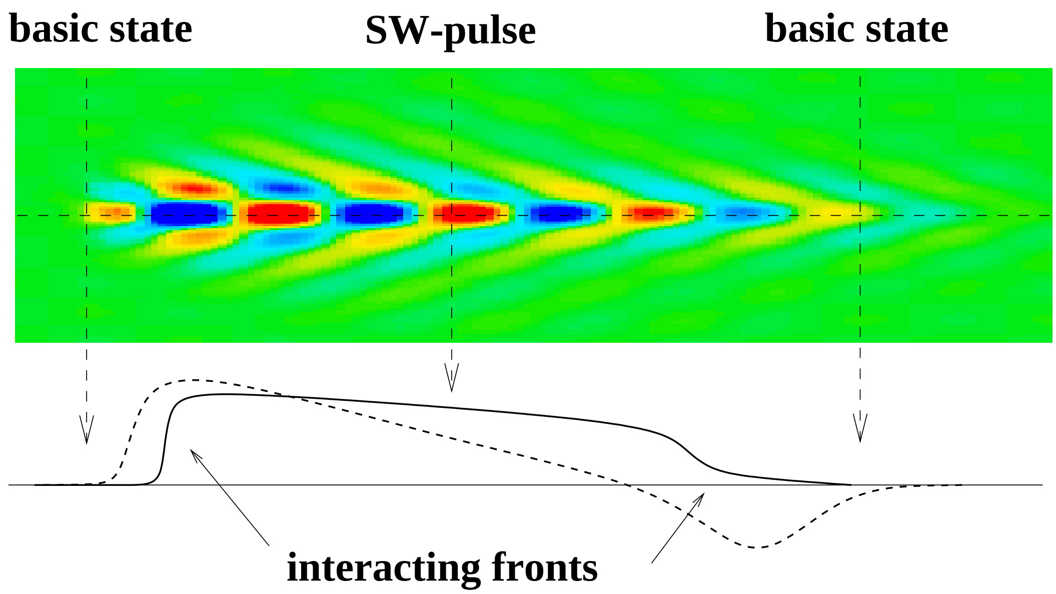

Figure 4.1: Numerically obtained worm solution to equations (1.11-1.13) [58]. The sketch is a cross-section in the x-direction showing the fronts connecting the basic state with the standing wave pulse.

In addition to the results presented in Section 3.5 for traveling-wave pulses, the effect of forcing on the one-dimensional standing-wave pulse was investigated. These standing-wave pulses are robust and do not change significantly for forcing strength small enough that the basic state remains stable. For forcing strength $|\nu| \sim |\mu|$, the basic zero state becomes unstable and the single pulse first loses stability to an array of pulses as shown in Figure 4.2. New pulses arise where the advected mode has decayed and is no longer strong enough to suppress convection [58]. A slight difference in the now nonzero amplitudes A and B leads to an accumulation of C which further enhances the growth rates of A and B to form the new pulses.

Figure 4.3 shows the solutions obtained for various values of the forcing strength. As the forcing increases, the number of pulses increases. Then for forcing strength $\nu = 0.2$, the solution no longer has a distinct pulse structure, but rather

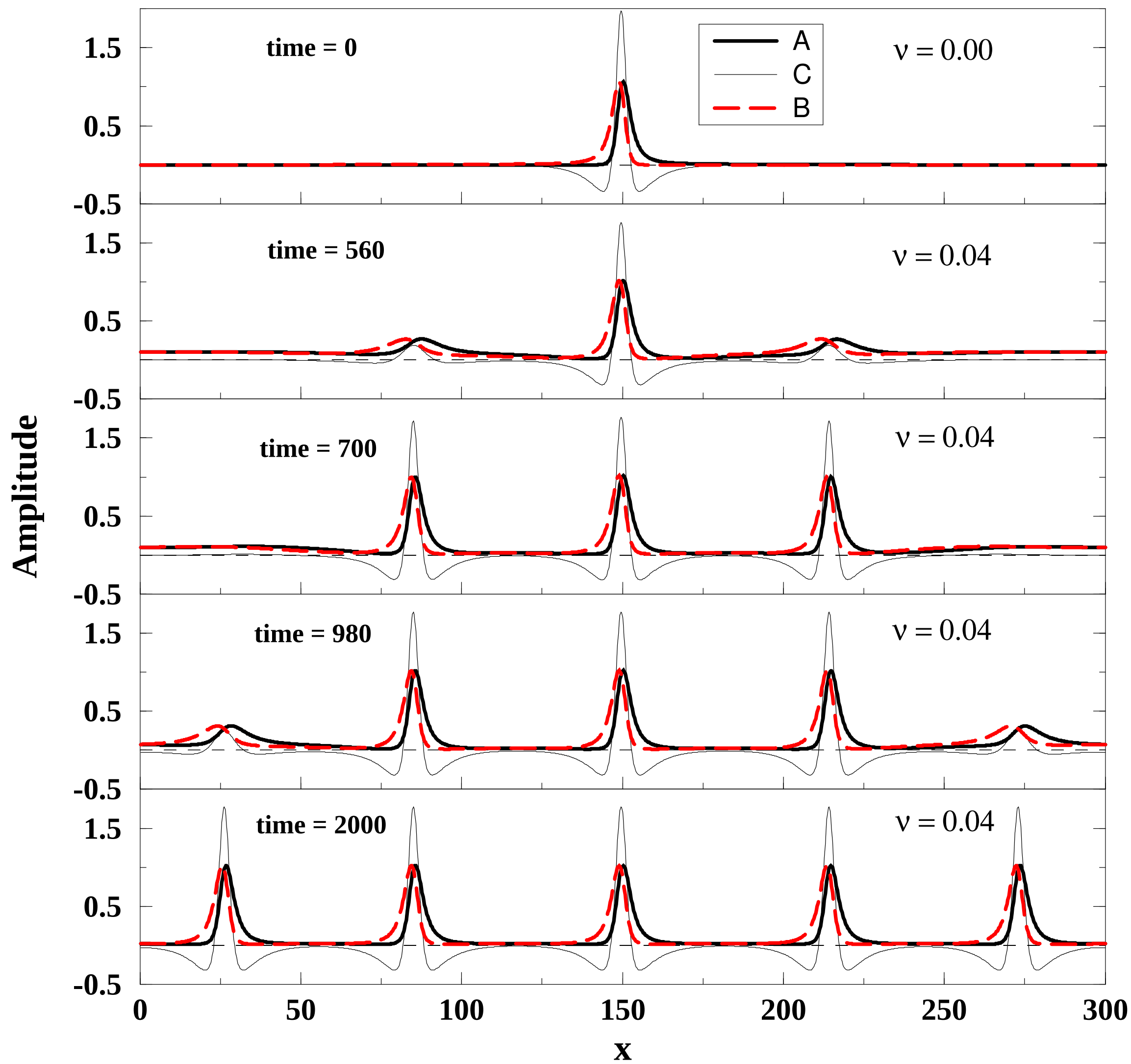

Figure 4.2: Time series of a standing-wave pulse for forcing strength $\nu = 0.04$. Parameters are $s = 0.75, \mu = -0.025, d = 1.0, c = 1.0, g = 0.5, f = 1.0, \delta = 0.7, \alpha = -0.02, h = 1.0$

the amplitudes are modulated in space. Finally, for forcing strength $\nu = 0.3$, the solution decays to a homogeneous small amplitude in A and B and the concentration field is no longer present. Similar results are found for the parameters $s = 1.5, d = 1.0, c = 1.0, g = 0.5, f = 1.0, \delta = 0.2, \alpha = -0.05, h = 1.0$, where the standing-wave pulse exists for even smaller values of the control parameter. For $\mu = -0.025, -0.15$, and -0.30, additional pulses first arise for forcing strengths $\nu = 0.07, 0.2$, and 0.4,

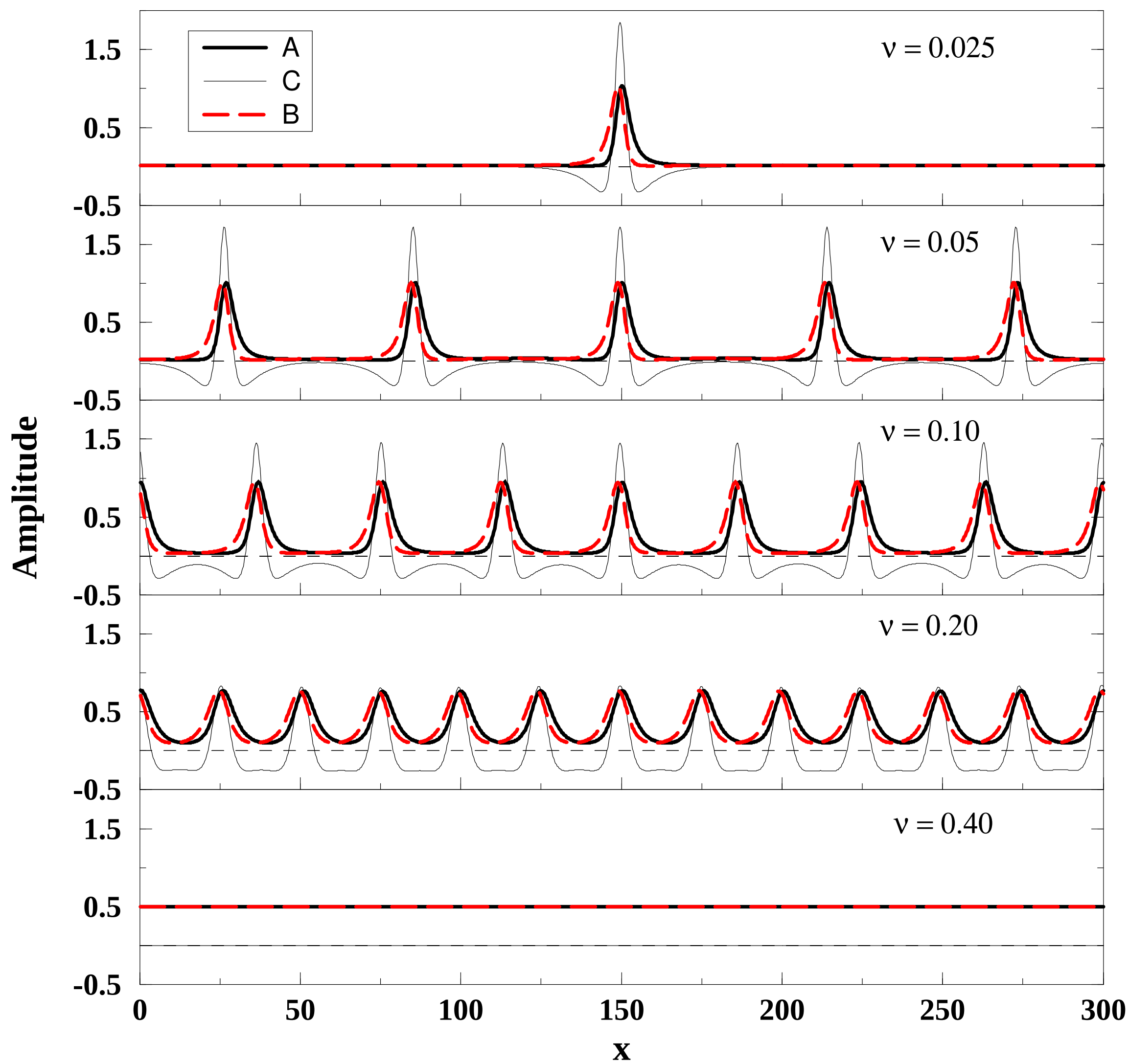

Figure 4.3: Solution as forcing strength increases $\nu = 0.025, 0.05, 0.10, 0.20$, and 0.04. All other parameters as in Figure 4.2.

respectively.

For two-dimensional worms it is then expected that forcing strength comparable to the size of the control parameter will generate new worms in the y-direction. Section 3.5 indicates that for sufficiently small group velocity, worms will remain localized traveling structures in the x-direction for increased forcing. As forcing increases above threshold, the worms are expected to either grow to fill the system or form a standing-wave pulse. Preliminary numerical simulations have indeed shown that forcing leads to a periodic modulation in the y-direction for small values of forcing strength. The parameters used were taken from [58] (Fig. 2): $\mathbf{u}_A = (0.05, 0.75), \mu = -0.025, d_x = d_y = 1.0, c = 1.0, g = 0.5, f = 1.0, \alpha = -0.02, \delta = 0.7, \mathbf{h}_A = (1, 1)$. These simulations have so far shown that the counterpropagating-wave amplitudes grow to full amplitude and the pulse grows to fill the length of the system. Hence, the control parameter μ would need to be sufficiently damping so that the worm would remain localized for intermediate values of forcing strength ν. Here again the worm length will depend on its velocity. From the results of Section 3.5 it is more likely to be observed that the velocity decreases and pulses grow with increased forcing. Further investigation is necessary to determine which other features are expected to be observed in the experimental system.

Bibliography

[1] P. Umbanhowar, F. Melo, and H. Swinney, Nature **382**, 793 (1996).

[2] M. Cross and P. Hohenberg, Rev. Mod. Phys. **65**, 851 (1993).

[3] Y. Pomeau, Physica D **23**, 3 (1986).

[4] D. Bensimon, B. Shraiman, and V. Croquette, Phys. Rev. A **38**, 5461 (1988).

[5] V. Hakim and Y. Pomeau, Eur. J. Mech. B **10**, 137 (1991).

[6] G. W. Baxter and C. D. Andereck, Phys. Rev. Lett. **57**, 3046 (1986).

[7] J. Hegseth, J. M. Vince, M. Dubois, and P. Bergé, Europhys. Lett. **17**, 413 (1992).

[8] T. Mahr and I. Rehberg, Phys. Rev. Lett. **81**, 89 (1998).

[9] H. R. Brand and R. J. Deissler, Phys. Rev. Lett. **63**, 508 (1989).

[10] H. R. Brand and R. J. Deissler, Phys. Rev. A **41**, 5478 (1990).

[11] R. J. Deissler, Y. C. Lee, and H. R. Brand, Phys. Rev. A **42**, 2101 (1990).

[12] H. Riecke, Europhys. Lett. **11**, 213 (1990).

[13] D. Raitt and H. Riecke, Physica D **82**, 79 (1995).

[14] D. Raitt and H. Riecke, Phys. Rev. E **55**, 5448 (1997).

[15] in *Nonlinear Dynamics and Pattern Formation in Semiconductors and Devices*, Springer Proceedings in Physics 79, edited by F.-J. Niedernostheide (Springer, Berlin, 1995).

[16] E. Ammelt, Y. Astrov, and H.-G. Purwins, in *Self-Organization in Activator-Inhibitor-Systems: Semiconductors, Gas-Discharge and Chemical Active Media*, edited by H. Engel, F.-J. Niedernostheide, H.-G. Purwins, and E. Schöll (Wissenschaft und Technik Verlag, Berlin, 1996), pp. 22–27.

[17] L. Schimansky-Geier, C. Zülicke, and E. Schöll, Zeitschrift für Physik B **84**, 433 (1991).

[18] A. Alekseev, S. Bose, P. Rodin, and E. Schöll, Phys. Rev. E **57**, 2640 (198).

[19] A. J. Simon, J. Bechhoefer, and A. Libchaber, Phys. Rev. Lett. **61**, 2574 (1988).

[20] M. Rabaud, S. Michalland, and Y. Couder, Phys. Rev. Lett. **64**, 184 (1990).

[21] H. Z. Cummins, L. Fourtune, and M. Rabaud, Phys. Rev. E **47**, 1727 (1993).

[22] M. Gorman and M. El-Hamdi, Combust. Sci. and Tech. **98**, 71 (1994).

[23] R. J. Wiener and D. F. McAlister, Phys. Rev. Lett. **69**, 2915 (1992).

[24] P. Coullet, R. E. Goldstein, and G. H. Gunaratne, Phys. Rev. Lett. **63**, 1954 (1989).

[25] R. E. Goldstein, G. H. Gunaratne, and L. Gil, Physcial Review A **41**, 5731 (1990).

[26] R. E. Goldstein, G. H. Gunaratne, L. Gil, and P. Coullet, Phys. Rev. A **43**, 6700 (1991).

[27] H. Riecke and H.-G. Paap, Phys. Rev. A **45**, 8605 (1992).

[28] B. Caroli, C. Caroli, and S. Fauve, J. Phys. I **2**, 281 (1992).

[29] S. Fauve, S. Douady, and O. Thual, Phys. Rev. Lett. **65**, 385 (1990).

[30] A. C. Newell, *Solitons in Mathematics and Physics* (SIAM, Philadelphia, 1985).

[31] G. P. Agrawal, *Nonlinear Fiber Optics*, 2 ed. (Academic Press, Inc., San Diego, 1995).

[32] J. Wu, R. Keolian, and I. Rudnick, Phys. Rev. Lett. **52**, 1421 (1984).

[33] J. Wu, J. Wheatley, S. Putterman, and I. Rudnick, Phys. Rev. Lett. **59**, 2744 (1987).

[34] F. Melo, P. Umbanhowar, and H. Swinney, Phys. Rev. Lett. **72**, 172 (1994).

[35] F. Melo, P. Umbanhowar, and H. Swinney, Phys. Rev. Lett. **75**, 3838 (1995).

[36] P. Umbanhowar, F. Melo, and H. Swinney, Physica A (1997).

[37] H. Jaeger, S. Nagel, and R. Behringer, Rev. Mod. Phys. **68**, 1259 (1996).

[38] R. Metcalf, J. Knight, and H. Jaeger, Physica A **236**, 202 (1997).

[39] P. B. Umbanhowar, F. Melo, and H. L. Swinney, Physica A **249**, 1 (1998).

[40] L. Tsimring and I. Aranson, Phys. Rev. Lett. **79**, 213 (1997).

[41] S. Venkataramani and E. Ott, Phys. Rev. Lett. **80**, 3495 (1998).

[42] E. Cerda, F. Melo, and S. Rica, Phys. Rev. Lett. **79**, 4570 (1997).

[43] D. Rothman, Phys. Rev. E **57**, 1239 (1998).

[44] J. Eggers and H. Riecke, Phys. Rev. E **59**, 4476 (1999).

[45] T. Shinbrot, Nature **389**, 574 (1997).

[46] D. Bensimon *et al.*, J. Fluid Mech. **217**, 441 (1990).

[47] B. A. Malomed and A. A. Nepomnyashchy, Phys. Rev. A **42**, 6009 (1990).

[48] H. Riecke, Phys. Rev. Lett. **68**, 301 (1992).

[49] H. Riecke, Physica D **61**, 253 (1992).

[50] H. Herrero and H. Riecke, Physica D **85**, 79 (1995).

[51] H. Riecke and W.-J. Rappel, Phys. Rev. Lett. **75**, 4035 (1988).

[52] M. Dennin, G. Ahlers, and D. S. Cannell, Phys. Rev. Lett. **77**, 2475 (1996).

[53] M. Dennin, G. Ahlers, and D. S. Cannell, Science **272**, 388 (1996).

[54] M. Dennin, D. S. Cannell, and G. Ahlers, Phys. Rev. E **57**, 638 (1998).

[55] U. Bisang and G. Ahlers, Phys. Rev. E **60**, 3910 (1999).

[56] Y. Tu, Phys. Rev. E **56**, R3765 (1997).

[57] M. Treiber and L. Kramer, Phys. Rev. E **58**, 1973 (1998).

[58] H. Riecke and G. D. Granzow, Phys. Rev. Lett. **81**, 333 (1998).

[59] C. Crawford and H. Riecke, Physica D **129**, 83 (1999).

[60] H. Riecke, Europhys. Lett. **2**, 1 (1986).

[61] H. Sakaguchi and H. Brand, Physica D **97**, 274 (1996).

[62] H. Sakaguchi and H. Brand, Europhys. Lett. **38**, 341 (1997).

[63] V. Gertsberg and G. Sivashinsky, Prog. Theor. Phys. **66**, 1219 (1981).

[64] J. Lega, J. V. Moloney, and A. C. Newell, Phys. Rev. Lett. **73**, 2978 (1994).

[65] J. Kutz *et al.*, J. Opt. Soc. A. B **11**, 2112 (1994).

[66] B. Sandstede, C. Jones, and J. Alexander, Physica D **106**, 167 (1997).

[67] H. Müller, private communication .

[68] J. Fineberg, private communication .

[69] O. Lioubashevski *et al.*, Phys. Rev. Lett. **83**, 3190 (1999).

[70] H. Riecke, J. D. Crawford, and E. Knobloch, Phys. Rev. Lett. **61**, 1942 (1988).

[71] D. Walgraef, Europhys. Lett. **7**, 485 (1988).

[72] H. Riecke, J. D. Crawford, and E. Knobloch, in *New Trends in Nonlinear Dynamics and Pattern-Forming Phenomena: The Geometry of Nonequilibrium*, edited by P. Coullet and P. Huerre (Plenum Press, New York, 1990), pp. 61–64.

[73] C. Martel and J. M. Vega, Nonlinearity **9**, 1129 (1996).

[74] H. R. Brand and R. J. Deissler, Physical Reveiw A **45**, 3732 (1992).